IMPERIAL COLLEGE LONDON

HIGH ACCURACY ULTRASONIC DEGRADATION MONITORING

by

Attila Gajdacsi

A thesis submitted to Imperial College London for the degree of

Doctor of Philosophy

Department of Mechanical Engineering
Imperial College London
London SW7 2AZ

June 2015

Declaration of originality

The content of this thesis is my own work under the supervision of Dr. Frederic Cegla and Professor Peter Cawley. Wherever the work of others has been used, appropriate references are provided.

Attila Gajdacsi

15/06/2015

Copyright Declaration

Abstract

This thesis is concerned with maximising the precision of permanently installed ultrasonic time of flight sensors. Numerous sources of uncertainty affecting the measurement precision were considered and a measurement protocol was suggested to minimise variability. The repeatability that can be achieved with the described measurement protocol was verified in simulations and in laboratory corrosion experiments as well as various other experiments. One of the most significant and complex problems affecting the precision, inner wall surface roughness, was also investigated and a signal processing method was proposed to improve the accuracy of estimated wall thickness loss rates by an order of magnitude compared to standard methods.

It was found that the error associated with temperature effects is the most significant among typical experimental sources of uncertainty (*e.g.* coherent noise and coupling stability). By implementing temperature compensation, it was shown in laboratory experiments that wall thickness can be estimated with a standard deviation of less than 20 nm when temperature is stable (within 0.1 °C) using the signal processing protocol described in this thesis. In more realistic corrosion experiments, where temperature changes were of the order of 4 °C), it was shown that a wall thickness loss of 1 µm can be detected reliably by applying the same measurement protocol.

Another major issue affecting both accuracy and precision is changing inner wall surface morphology. Ultrasonic wave reflections from rough inner surfaces result in distorted signals. These distortions significantly affect the accuracy of wall thickness estimates. A new signal processing method, Adaptive Cross-Correlation (AXC), was described to mitigate the effects of such distortions. It was shown that AXC reduces measurement errors of wall thickness loss rates by an order of magnitude compared to standard signal processing methods so that mean wall loss can be accurately determined. When wall thickness loss is random and spatially uniform, 90% of wall thickness rates measured using AXC lie within $7.5 \pm 18\%$ of the actual slope. This means that with mean corrosion rates of 1 mm/year, the wall thickness estimate with AXC would be of the order of 0.75-1.1 mm/year.

In addition, the feasibility of increasing the accuracy of wall thickness loss rate

measurements even further was demonstrated using multiple sensors for measuring a single wall thickness loss rate. It was shown that measurement errors can be decreased to 30% of the variability of a single sensor.

The main findings of this thesis have led to 1) a solid understanding of the numerous factors that affect accuracy and precision of wall thickness loss monitoring, 2) a robust signal acquisition protocol as well as 3) AXC, a post processing technique that improves the monitoring accuracy by an order of magnitude. This will benefit corrosion mitigation around the world, which is estimated to cost a developed nation in excess of 2-5% of its GDP. The presented techniques help to reduce response times to detect industrially actionable corrosion rates of 0.1 mm/year to a few days. They therefore help to minimise the risk of process fluid leakage and increase overall confidence in asset management.

Acknowledgements

I would like to express my deepest gratitude to my supervisor Dr. Frederic Cegla for giving me the opportunity to join the NDE lab at Imperial College. His limitless ingenuity and excellent guidance ensured that if there were any obstacles we faced throughout this PhD project, we found a way to go around them. Furthermore, I would like to thank Prof. Peter Cawley and Prof. Mike Lowe for their stimulation and for creating a fantastic working environment. I would also like to thank all the members of the lab for their help, especially Balint Herdovics for providing much of the measurement data in Chapter 4 and Peter Huthwaite for insightful conversations about imaging techniques thus helping to improve Chapter 6.

I owe a debt of gratitude to Dr. Jon Allin, Dr. Peter Collins and Dr. Jake Davies of Permasense Ltd., where I have been working part-time in the last two years. Their recognition and support motivated me greatly and allowed me to better understand the commercial implications of the work presented in this thesis. I would also like to thank Richard Braint, Nikki Hill and all other employees of Permasense Ltd., for their active interest in my research and for being patient with me while writing this thesis.

Finally, I would like to thank my family for their continued encouragement. I am most grateful for the support of my wife, Tamara, without her support this work would have been considerably harder.

Contents

List of Figures

Nomenclature

δ	Kronecker delta
γ	First Lamé parameter
μ	Second Lamé parameter
∇	Nabla operator
Ω	Number of cycles in toneburst
ω	Angular frequency
Φ	Scalar potential
ρ	Material density
σ	Standard deviation
σ_{ij}	Stress tensor
Θ	Temperature
ε	Strain tensor
A	Amplitude
BW	Backwall surface geometry
c	Propagation velocity of waves
CL	Correlation length
d	Separation of transducers
f	Frequency
F_i	Body force per unit volume
H	Vector potential
k	Wave number
N	Number of measurements
P	Pressure
S	Waveform or signal
T	Thickness of sample

t	Time
u_i	Displacement vector
v_f	Void fraction
w	Transducer length

Chapter 1

Introduction

1.1 Motivation

It is common industrial practice to establish a finite design life for engineering plants, structures and components. This is because there are many degradation mechanisms, such as corrosion, erosion, material fatigue, decarburisation, various forms of crack formation, etc. that affect plant components [1–6]. The effect of these degradation mechanisms can to some extent be mitigated (*e.g.*: by using more resistant alloys or by injecting chemical compounds such as corrosion inhibitors). However, even exotic alloys degrade and often operators deliberately use cheaper materials that degrade more readily but at a somewhat predictable rate. Most components used in plants are therefore expected to degrade as they get older.

Components that degrade over time have to be replaced before they become unfit for service and can potentially cause failures. There is a large economic incentive to delay replacements for as long as possible and extend component life. Non-destructive inspection and monitoring (often called SHM) of component integrity are typically used to measure and predict the rate of degradation. This helps to avoid failures and enables safe plant operation, in some cases even beyond the intended design life of the component.

An example of the scale of the component degradation problem is illustrated by studies on the cost of corrosion, a specific degradation mechanism: Biezma *et al.*

estimated that the cost of corrosion (*i.e.*: mitigation, prevention and replacement) to a developed nation is of the order of 2-5% of the gross domestic product [7, 8]. Although there are accurate electrochemical techniques available to monitor corrosion, such measurements lack the capability to localise where corrosion occurs. In addition, electrochemical techniques do not provide a measurement of remaining component strength. In contrast, ultrasonic non-destructive evaluation yields measurements of the remnant wall thickness, a good indicator of component health.

The disadvantage of standard ultrasonic inspections is that they are reported to be imprecise with a wall thickness measurement variability of up to ± 1 mm [9, 10]. This is because standard hand-held ultrasonic inspections are carried out manually, resulting in large errors due to positional offsets. In addition, it takes strategic effort to plan and execute them, since the plant needs to be shut down for inspections. Hence they can only be carried out at certain times resulting in infrequent inspections. Months or years may elapse between inspections and a given component may be evaluated by different inspectors each time. Both these factors further increase variability. Because of infrequent and imprecise measurements, it is not possible to extract accurate corrosion rates as illustrated by Figure 1.1.a, which figure will be repeated and explained in more detail in Chapter 2.

Permanently installed ultrasonic monitoring addresses many of the concerns associated with manual inspection because automated measurements are taken at

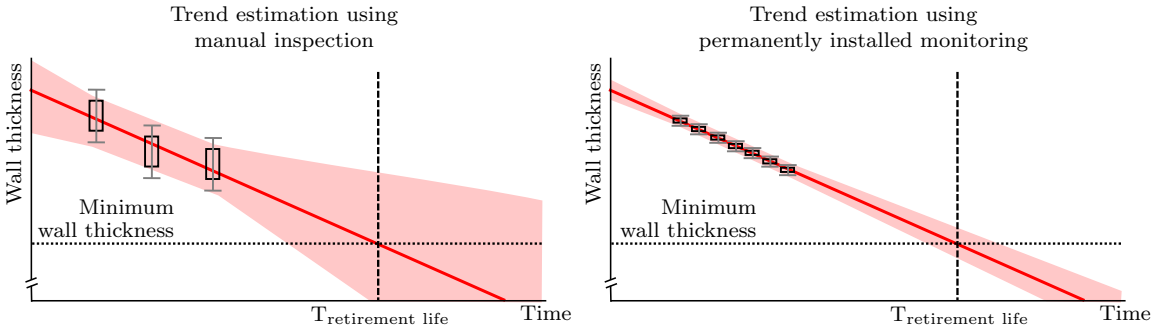

Figure 1.1: Left graph shows measurement uncertainties associated with manual inspection, whereas right graph shows uncertainties associated with permanently installed monitoring. Both graphs show the variability of individual point measurements as box plots with whiskers (box indicates 50% of measurements, while whiskers represent 90% of measurements). The variability of trend estimates is shown by a red patch. The real mean wall thickness in the geometrical sense is shown by a dark red line.

fixed locations, grossly reducing coupling errors and reducing operator involvement. Firstly, data can be collected more frequently using automated permanently installed sensors. In addition, permanently installing sensors allows for much more repeatable measurements compared to manual inspections because errors associated with sensor positioning are eliminated. More frequent and more repeatable thickness measurements result in much more accurate wall thickness loss rate estimates.

The key challenge associated with permanently installed monitoring is to maximise precision over the sensor lifetime (long periods of time). There are a number of unknowns in relation to the precision of ultrasonic monitoring. What are the dominant factors influencing measurement precision? What are the factors limiting wall thickness loss rate estimation accuracy? Once error sources have been identified, techniques to minimise their effect should be evaluated. Investigating these questions with the purpose of maximising the precision of ultrasonic measurements is the primary motivation for this thesis.

The presented work applies to ultrasonic measurements in general. Therefore monitoring material degradation mechanisms other than corrosion induced wall thickness loss is also discussed. High Temperature Hydrogen Attack is an example of such mechanisms, where small methane bubbles form in the material as a result of hydrogen diffusing into steel and reacting with the carbon content of the steel. The thickness of the affected component therefore does not change, and instead the material is weakened due to the small voids. Since the small voids are expected to cause a drop in ultrasonic propagation velocity, such mechanisms can also potentially be monitored ultrasonically and this was also investigated in this work.

1.2 Thesis aims and outline

The primary aim of this thesis is to gain a solid understanding of errors in permanently installed ultrasonic monitoring setups and to experimentally demonstrate how travel time measurement precision can be maximised to achieve unprecedented levels of accuracy in corrosion rate measurements. In addition, it is also shown how signal processing techniques can be used to mitigate the detrimental effects of inner wall

surface roughness on ultrasonic measurements. The thesis is organised as follows:

First the background of wave propagation physics and the principles of ultrasonic wall thickness measurements are introduced in Chapter 2. This chapter starts by explaining the equations describing the physics of ultrasonic wave propagation in bulk media. The details of wall thickness measurements using permanently installed ultrasonic sensors are then explained. As part of this, a standard commercially available permanently installed waveguide transducer is described. This transducer is suitable for all conditions investigated in this theses and is used as an example throughout the thesis to demonstrate how the presented methods can be applied.

Chapter 3 evaluates signal processing methods that can be used to mitigate uncertainties inherent in ultrasonic signal acquisition. First a robust signal processing protocol for precise ultrasonic wall thickness measurements is presented. This is described early on as it provides a good overview of the required signal processing steps. Following this, the investigations that were used to calibrate the parameters of the various steps of the final protocol are described. As part of this, the maximum possible precision that can be achieved using the waveguide sensors is established. Although the quantitative results are specific to the waveguide sensor, it is thought that the process of evaluation itself applies to other sensors as well.

Having established uncertainties associated with signal acquisition and processing, Chapter 4 evaluates uncertainties associated with experimental measurements. This chapter evaluates 3 of the most significant experimental sources of error and quantifies them separately. Coherent noise is discussed first. Quantitative results are also shown and evaluated for the waveguide sensor. The second issue discussed is the coupling stability of sensors. A key advantage of permanently installed sensors is that coupling is more stable compared to conventional sensors, however it still is not expected to remain constant indefinitely, hence the effects of potential changes are evaluated. The third issue that is discussed is the effect of temperature on ultrasonic time-of-flight measurements. Beyond simple temperature compensation, the effects of temperature gradients within the component are also evaluated.

Chapter 5 evaluates ultrasonic measurements in experiments. Here, controlled corrosion processes are used to induce wall thickness loss, which is then monitored

using a permanently installed ultrasonic sensor. The chapter starts by introducing the theory of how corrosion can be induced using a forced current. This approach is proposed as it is expected that the forced current is proportional to induced corrosion and hence can be used to benchmark the ultrasonic wall thickness results. In addition, theory on unforced corrosion is also presented as a more realistic alternative. As part of this, an electrochemical measurement approach is described that can be used to estimate the naturally occurring corrosion rate. Experimental results are then shown using both forced and unforced corrosion cells. Electrolytes that were tested are: NaCl, Na_2SO_3, distilled water, various concentrations of citric acid and HCl.

Chapter 6 evaluates another potential area of application for time-of-flight ultrasonic measurements: material degradation mapping. Here, background on Hydrogen Attack is presented highlighting associated safety concerns, and hence the importance of overcoming challenges for monitoring it. It is pointed out that the effect of Hydrogen Attack on ultrasonic waves can be modelled as a change to ultrasonic propagation velocity. Since the degradation itself is difficult and dangerous to induce, heating is used to create a non-uniform ultrasonic propagation velocity distribution within a test component. This is expected to result in a non-uniform velocity distribution similar to what would be expected to be the effect of Hydrogen Attack. During the transient heating, ultrasonic measurements are recorded using a waveguide sensor array. Imaging algorithms are then presented for the reconstruction of the spatial velocity distribution based on the ultrasonic measurements. Following the encouraging results of the feasibility study using heat, the implementation of a Hydrogen Attack rig is presented. Results of the Hydrogen Attack measurements are then described, including comparisons of ultrasonically measured data with SEM images.

The effect of backwall surface morphology changes, or backwall surface roughness, is relatively complex. Chapters 5 and 6 do mention the topic, however, because of its complexity, it is evaluated separately in Chapter 7. More specifically, gradual geometrical changes of the component surface on the accuracy of ultrasonically measured corrosion rates are investigated in this chapter. The relevance of this is that permanently installed sensors carry out frequent measurements at a fixed location, hence the geometry of the underlying surface is expected to change only gradually between

measurements. For this, a model to simulate gradual surface morphology changes is introduced first. Since such morphology changes are expected to significantly affect ultrasonic thickness estimates [11], a new arrival time estimation method is also introduced. This new method specifically addresses the challenges of measuring wall thicknesses of components with gradually changing surface morphologies. A large number of gradually changing backwall surfaces are then simulated and evaluated using both conventional and newly introduced signal processing methods.

The results of Chapter 7 suggest that under certain surface roughness conditions the accuracy of ultrasonic wall thickness loss rate estimates is limited. Therefore Chapter 8 investigates the feasibility of using multiple transducers to monitor wall thickness loss more accurately. Two configurations are considered. The first setup relies on multiple transducers illuminating the same patch of the backwall surface from different angles. The second configuration relies on multiple transducer pairs coupled at various locations, where the mean wall loss is assumed to be the same. Both multi-transducer configurations are evaluated for the gradually changing backwall surface evolution conditions investigated in Chapter 7 and their performance is compared to a single transducer pair.

All results of the thesis are then summarised in Chapter 9, where conclusions are drawn and future work is suggested.

Chapter 2

Background Theory and Analysis Tools

2.1 Introduction

The purpose of this chapter is to provide the theoretical background for the work in this thesis. First, the underlying theory of ultrasonic measurements is introduced, including the basic governing equations of wave propagation in elastic media. The principles of how ultrasonic waves can be used for wall thickness measurements are then demonstrated using an existing commercially available ultrasonic sensor. A decision was taken to use this existing ultrasonic sensor hardware as an example experimental test setup for measurements in this thesis. It is believed that the developed methodology is also applicable to other ultrasonic setups, while specific details and results may vary. It is then explained why permanently installed ultrasonic monitoring in particular is more precise than traditional manual inspection methods. Finally, a simulation technique that is capable of rapidly simulating realistic ultrasonic signals reflected from components of varying geometries is described. This is particularly important for analysing the effect that subtle changes in geometry will have on the signal.

2.2 Wave equations and wave propagation in bulk media

The theory of elastic wave propagation is well known. It has been studied by many authors, see for example [12–14]. A brief summary of the underlying equations is recalled here, in order to provide the foundation for all of the tools and techniques used in this thesis. First, the equation of linear momentum is considered. This can be expressed in Cartesian tensor notation as:

$$\sigma_{ij,j} + F_i = \rho \ddot{u}_i \tag{2.1}$$

where $\sigma_{ij,j}$ is the stress tensor at a point, ρ is the density of the material, F_i is the body force per unit volume and $\ddot{u}_i$ is the acceleration vector of a point of the material. For isotropic materials, the stress tensor can be expressed as a function of the strain tensor using Hooke's law:

$$\sigma_{ij} = \gamma \varepsilon_{kk} \delta_{ij} + 2\mu \varepsilon_{ij} \tag{2.2}$$

$$\varepsilon_{ij} = \frac{1}{2}\left(u_{i,j} + u_{j,i}\right) \tag{2.3}$$

where γ and μ are the first and second Lamé parameters in the solid, ε is the strain tensor and δ is the Kronecker delta. By substituting Equations 2.2 and 2.3 into Equation 2.1 with the assumption that the material is homogeneous and there are no body forces, Navier's equation is obtained:

$$(\gamma + \mu) u_{j,ij} + \mu u_{i,jj} = \rho \ddot{u}_i \tag{2.4}$$

Calculating the divergence of Navier's equation results in:

$$\nabla^2 \Phi = \frac{1}{c_L^2} \ddot{\Phi} \tag{2.5}$$

where ∇ is the nabla operator, Φ is the scalar potential of the displacement field and c_L is the propagation velocity of any dilatational disturbance (longitudinal waves). This is referred to as the wave equation for longitudinal waves. c_L is therefore

expressed by:

$$c_L = \sqrt{\frac{\gamma + 2\mu}{\rho}} \tag{2.6}$$

In contrast, performing the operation of curl on Equation 2.4 results in:

$$\nabla^2 H = \frac{1}{c_T^2}\ddot{H} \tag{2.7}$$

where H is the vector potential of the displacement field and c_T is the propagation velocity of transverse wave motion (shear waves). This therefore constitutes the wave equation for shear waves. c_T in Equation 2.7 can also be expressed by:

$$c_T = \sqrt{\frac{\mu}{\rho}} \tag{2.8}$$

Since Φ and H are the scalar and vector potentials of the displacement field, together they constitute its Helmholtz decomposition of the displacement field:

$$u = \nabla\Phi + \nabla \times H, \qquad \text{with } \nabla.H = 0 \tag{2.9}$$

Therefore the longitudinal and the shear modes describe wave motion in the bulk of isotropic homogeneous media. They propagate within the medium independently at different velocities, and mode conversion only takes place at boundaries. The concept of exploiting elastic wave propagation for non-destructive testing purposes is well established and has been implemented in a wide array of tools and methods [15–22]. The main motivation of this thesis is high accuracy measurements of progressive degradation such as thickness loss or material property (ultrasonic velocity) change, and therefore the next sections elaborate on how to take advantage of ultrasonic waves for the purposes of high accuracy measurements.

2.3 Ultrasonic measurement principles

It has long been known that ultrasonic waves can be used for the purposes of wall thickness measurements [23]. A waveguide transducer is used here to demonstrate the principle of such measurements in Figure 2.1. The waveguide itself is a long

thin strip with a cross section of 1 mm by 15 mm rectangle. The advantage of this setup is that if the specimen is at a high temperature, an otherwise temperature sensitive piezo element can be used for transduction of ultrasonic waves. The chosen transducer uses shear horizontal (SH) waves, and the waveguide acts as a delay line to transmit the waves into the material. Since the waveguide is used to transmit SH waves, transduction into the sample can be achieved without exciting longitudinal or shear vertical modes in the plane of interest. Because of the close proximity of boundaries within a waveguide however, there are a large number of guided wave modes that exist in it. The propagation within this waveguide proposed by Cegla *et al.* [24, 25] has been extensively studied, and therefore is not investigated in this thesis.

This transducer is typically used in a pitch-catch arrangement, which is used in this thesis, as shown in Figure 2.1. Here, two waveguide transducers are used, one for transmission and the second for reception. The pitch-catch arrangement is especially advantageous as it reduces coherent noise in the measurement. This is because the transmission coefficient of the transmitting waveguide into the sample is rather poor and the returning signal might be masked by higher amplitude end reflections of undesired wave modes travelling in the transmit waveguide. On transmission into a second receiving transducer this is however not the case as the transmitted signal will be strongest. (This is similar to the use of dual element probes that are commonly used in UT).

During a typical acquisition using a pitch-catch setup, the sending transducer (Tx) is first excited with a wavepacket. The excited wavepacket then travels down the sending waveguide transducer and gets transmitted into the component that is being tested, where it propagates to the interface of the receiving transducer via different paths within the component as shown in Figure 2.1. The wavepackets then get transmitted into the receiver waveguide and propagate towards the receiver piezo element to be converted into electrical signals. An example of a measured signal is shown in Figure 2.2.

Since the wavepaths travelled by the ultrasonic wavepacket are significantly different in length, they arrive at the receiver at different times. These arrival times can then be estimated. As the geometry of the setup is known and the propagation velocity

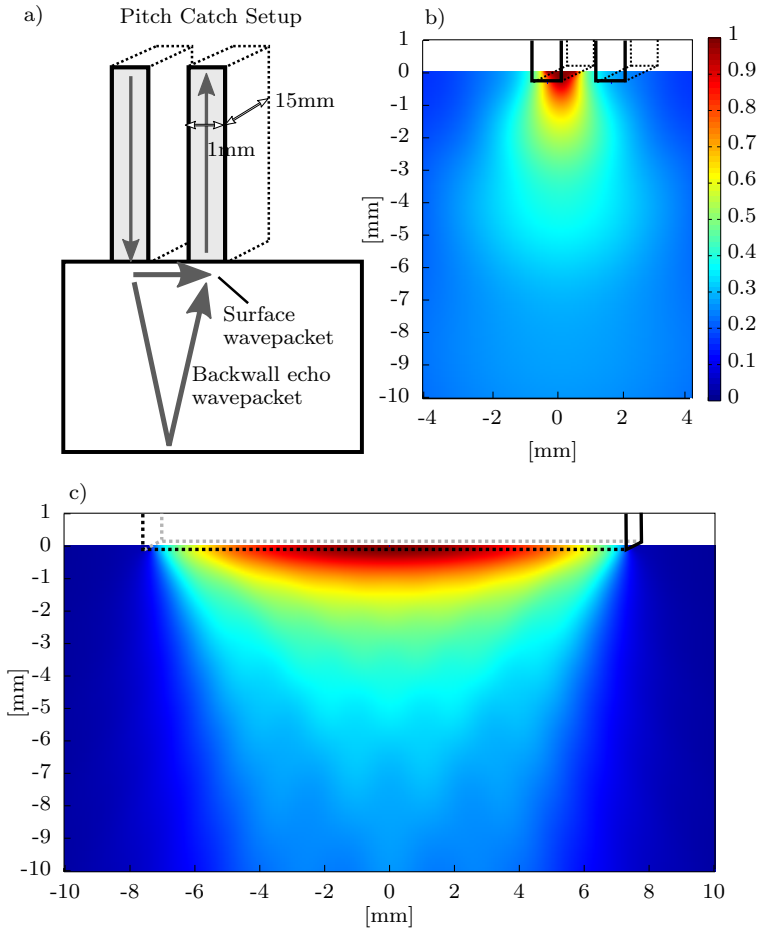

Figure 2.1: a) shows a pitch-catch measurement setup using waveguide transducers. Here grey arrows show the paths of the ultrasonic wavepackets. b) and c) show the beam spread of the waveguide transducer along its central planes computed using a 3D Huygen's model with a wavelength of 1.6 mm. b) shows the beam spread of the sending transducer in its cross section parallel to the 1 mm edge whereas c) shows the beam spread of the sending transducer in its cross section parallel to the 15 mm edge using the same colour scale as b).

of the ultrasonic waves can be determined, the calculation of the thickness is also possible. Here, the propagation equations that describe the arrival times of the first 3 wavepackets (as shown in Figure 2.2) based on ultrasonic propagation velocities and geometric considerations are shown:

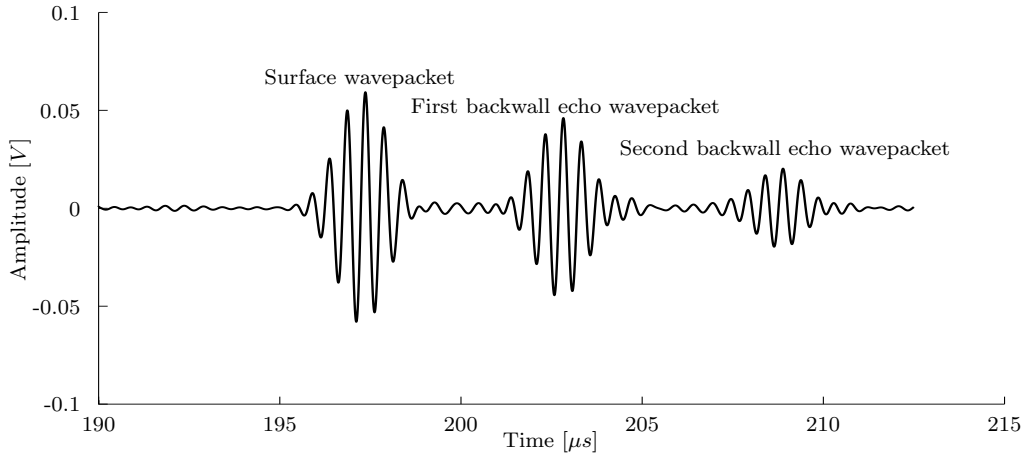

Figure 2.2: Example signal recorded using waveguide transducers in a pitch-catch setup on a 10 mm thick mild steel sample at room temperature where ultrasonic wave propagation velocity is 3250 m/s using a 2 MHz 5-cycle toneburst as excitation.

$$t_1 = \frac{w_t}{c_{wt}} + \frac{d}{c_m} + \frac{w_r}{c_{wr}} \tag{2.10}$$

$$t_2 = \frac{w_t}{c_{wt}} + 2 \cdot \frac{\sqrt{\left(\frac{d}{2}\right)^2 + T^2}}{c_m} + \frac{w_r}{c_{wr}} \tag{2.11}$$

$$t_3 = \frac{w_t}{c_{wt}} + 4 \cdot \frac{\sqrt{\left(\frac{d}{4}\right)^2 + T^2}}{c_m} + \frac{w_r}{c_{wr}} \tag{2.12}$$

where t_n is the estimated arrival time of the n^{th} wavepacket, w_t and w_r are the lengths of the transmitter and receiver waveguide transducers, c_{wt} and c_{wr} are the average propagation velocities of ultrasonic waves in the transmitter and receiver waveguides, d is the separation of the waveguide transducers, c_m is the average propagation velocity within the material of the sample and T is the thickness of the sample. By solving this system of equations for the thickness, the following results:

$$T_{3p} = \frac{1}{4}\sqrt{c\left(t_3 - t_1\right)}\sqrt{c\left(t_3 - t_1\right) + \frac{-4c\left(t_2 - t_1\right)^2 + c\left(t_3 - t_1\right)^2}{4\left(t_2 - t_1\right) - \left(t_3 - t_1\right)}} \tag{2.13}$$

$$T_{2p} = \frac{1}{2}\sqrt{c\left(t_1 - t_2\right)\left(-2d - c \cdot t_2 + c \cdot t_1\right)} \tag{2.14}$$

where T_{3p} is the solution for the system of equations consisting of all 3 equations (surface wavepacket, first backwall echo wavepacket and second backwall echo wavepacket), whereas T_{2p} is the solution for the equations only for the first two equations. It is apparent, that both equations rely on the estimated arrival times

and the propagation velocity of the ultrasonic waves in the material. In order to obtain a good estimate of the mean wall thickness, which is the focus of this thesis, it is critical that these variables are determined accurately in apriori measurements.

Both equations therefore rely on the shear velocity which is a function of material parameters μ and ρ as described by Equation 2.8 and therefore it is expected to be a material property. In addition, these parameters typically also vary as a function of temperature. There are no additional environmental conditions (*e.g.*: ambient pressure) that significantly influence these parameters under typical operating conditions. Although stresses in the pipe wall may influence the ultrasonic propagation velocity via the acoustoelastic effect [26], such stresses are not expected to be present during normal operation and their effect is small compared to the effect of temperature. They are therefore ignored in this work. The most important variable that influences the propagation velocity of shear waves during measurements is the temperature. By measuring temperature, it is expected that shear velocity can be determined either by calculation (using Equation 2.8) or by calibration.

Beyond shear velocity, the variables to be determined in order to estimate wall thickness using equations 2.13 and 2.14 are the arrival times and the separation of waveguides. A difference between these equations is that in Equation 2.14 the separation of waveguides (d) is required as an input parameter whereas for Equation 2.13 it is not needed. Relying on d is expected to limit the accuracy of absolute thickness estimates, since it may not be possible to determine the effective separation accurately for every transducer pair. The advantage of the T_{2p} approach is that since the separation is constant for the permanently installed sensor, the calculated thicknesses are expected to be very repeatable.

Instead of d, Equation 2.13 relies on the arrival time of the second backwall echo t_3 for the solution. This may be disadvantageous in some scenarios, as this wavepacket is expected to be the lowest amplitude of the first 3 wavepackets. The signal-to-noise ratio for this wavepacket is therefore smaller than for the surface and backwall echo wavepackets, and so the variability of the estimated arrival time is expected to be higher. This may limit the repeatability of the estimated thickness. However, since the separation of waveguides does not have to be assumed, this is expected to result in more accurate absolute thickness measurements. In this thesis both equations are

used, since they both offer certain benefits under different conditions. Equation 2.14 is expected to provide more repeatable thickness estimates, whereas Equation 2.13 is expected to provide more accurate thickness estimates in absolute terms.

It should be noted here that the waveguide transducers were chosen because they are commercially available and are mechanically robust. They are suitable for many of the cases that are of interest in this thesis, such as high temperature measurements and corrosion monitoring. However, the techniques that are presented here are aimed to be more generally applicable and are not transducer specific.

2.4 High Accuracy Monitoring Using Permanently Installed Sensors

Ultrasonic thickness measurements as described in the previous section have been used for manual hand-held inspections for more than 50 years [23], and such manual inspection techniques are still standard practice in industry [27, 28]. Because of positional offsets and coupling uncertainties in between measurements as well as operator slips and errors, the repeatability of manual measurements is limited. Errors of the order of 0.25-1 mm are expected [9, 10]. In addition, some of the pipes in petrochemical applications are hard to access. For example pipes have to be stripped of insulation, excavated from underground locations or scaffolding has to be built to reach pipes in overhead locations. Consequently, measurements are typically inaccurate and are carried out infrequently.

Permanently installed monitoring drastically reduces uncertainties associated with coupling and positional offsets. In addition, automated measurements are possible. Altogether this results in more frequent and more repeatable measurements compared to manual handheld inspection. Repeatability of the order of tens of nanometres have been reported in [29] and [P3]. Furthermore, permanently installed monitoring allows for substantial improvements in the accuracy to which mean wall thickness loss rates can be estimated. In a plant integrity assessment context accurate thickness loss rate estimation is very valuable, since it can be used for the early identification of corrosion/erosion activity, it can be correlated with changing process conditions and

can be used as input to control corrosion inhibition strategies. Achieving a sufficient level of accuracy for this has not been possible using standard manual inspection techniques.

The potentially higher accuracy in monitoring wall thickness loss rates using permanently installed sensors can be illustrated by considering the statistical uncertainty of a slope evaluated by discrete point measurements, see Figure 2.3. The variation of the slope can be linked to the uncertainty associated with each individual measurement. Assuming that the standard deviation of individual thickness measurements are the same, the standard deviation of the slope can be determined based on the temporal separation of the measurements. It can be shown that improvements in the repeatability of the individual measurements and the temporal separation between measurements have a dramatic effect on the accuracy with which trends can be estimated [30]:

$$\sigma_{slope} = \frac{\sigma}{\sqrt{\sum (t_i - \bar{t})^2}} \tag{2.15}$$

where σ_{slope} is the standard deviation of the slope, σ is the standard deviation of the individual thickness measurements, i is the index number of individual measurements, t_i are the times of measurements and $\bar{t}$ is the mean of all t_i.

By assuming that N number of measurements are carried out at equal Δt intervals

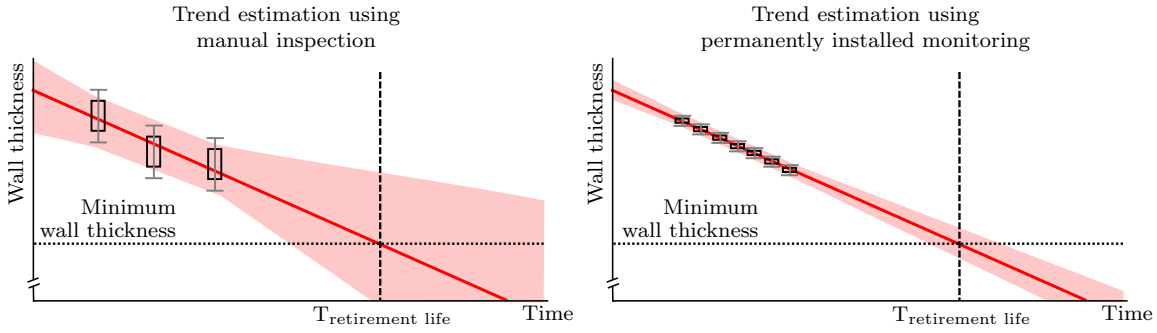

Figure 2.3: The left graph shows measurement uncertainties associated with manual inspection, whereas the right graph shows uncertainties associated with permanently installed monitoring. Both graphs show the variability of individual point measurements as box plots with whiskers (box indicates 50% of measurements, while whiskers represent 90% of measurements). The variability of trend estimates is shown by a red patch. The real mean wall thickness in the geometrical sense is shown by a dark red line.

in a period of $\widehat{t} = N \cdot \Delta t$ time, it is possible to expand Equation 2.15. In addition, by assuming that N is large, the effect of Δt on the standard deviation of the slope can be estimated (the derivation of this is explained in the Appending in Section A.1):

$$\sigma_{slope} = \frac{\sigma\sqrt{12}}{\Delta t\sqrt{N^3 - N}} \overset{N>>1}{\approx} \frac{\sigma\sqrt{12}}{\Delta t N^{3/2}} = \frac{\sigma\sqrt{\Delta t}\sqrt{12}}{\widehat{t}^{3/2}} \tag{2.16}$$

This means that the variability of the slope is proportional to the variability of individual measurements and is also proportional to the square root of the time interval between measurements. In other words, increasing the time interval between measurements by a factor of four doubles the slope variability. Hence, the concept of permanently installing sensors is expected to achieve a potential improvement in trend estimation accuracy of multiple orders of magnitude compared to manual methods, as standard deviation is improved by eliminating coupling errors and positional errors driving down σ and because very frequent measurements are possible *i.e.* improving both contributors to slope uncertainty.

The distinction about thickness precision (equivalent to the term thickness repeatability) and thickness accuracy should be pointed out here. The absolute accuracy of individual thickness measurements is expected to improve only marginally using permanently installed compared to manual hand-held sensors. It is the repeatability of thickness measurements that is improved by multiple orders of magnitude when using permanently installed ultrasonic sensors. In turn, this significant improvement in repeatability and the increase in measurement frequency enables substantial improvements in trend estimation accuracy. Hence, improvements in thickness measurement repeatability and trend estimation accuracy are the main focus of this thesis, but not improvements in thickness measurement accuracy.

2.5 DPSM (Distributed Point Source Method) simulation approach

There are many parameters and processes that have to be adjusted to optimise the measurement setup, such as acquisition hardware, signal processing tools and thickness calculation approaches. Ideally, any optimisation process is carried out in

simulations first, where uncertainties are minimal and are easily controlled compared to experimental data. Simulation tools are therefore introduced early on in this thesis. They will be used throughout the thesis as the basis of parametric studies or investigations.

One of the most popular simulation approaches is the Finite Element Method (FEM) [31,32]. FEM relies on discretising the domain of the material into nodes and elements that make up a mesh. Because of the discrete mesh that covers the entire domain, it is very versatile and non-uniform material properties are straightforward to incorporate in the model. However, it is not numerically efficient in cases where wave propagation over large parts of bulk material has to be simulated. To some extent this can be mitigated by creating hybrid FEM models that mesh the feature of interest and the transducer only and use analytical formulations to propagate wavefields in the bulk material. [33–36]. Although such an approach does improve computational efficiency, it still relies on meshing parts of the domain, and its performance is limited.

As an alternative the DPSM (Distributed Point Source Method) as proposed by Placko and Kundu [37] is considered. The DPSM is a semi-analytical method originally developed to solve field equations for a wide array of engineering problems (*e.g.*: for ultrasonic, magnetic, eletromagnetic fields). DPSM is mesh-free, which allows for a potential performance improvement compared to methods relying on discrete meshes such as FEM. Instead, DPSM relies on point sources to simulate the behaviour of boundaries and interfaces.

This method has been successfully implemented to simulate signals for the waveguide sensor (also used in this thesis) by Jarvis *et al.* [11], which was verified against FEM. In this thesis the same implementation is used, with some parametric adjustments as described here. This implementation relies on the assumption that SH waves can be modelled in 2D using an acoustic wave propagation model. This is because in a 2D model SH waves reflect from boundaries without mode conversion, since the direction of motion is perpendicular to the simulated plane. Hence the equation describing SH wave propagation is identical to that of acoustic wave propagation in 2D [12]. Furthermore, Jarvis *et al.* noted, that the cross-sectional width of the transducer (1 mm) is relatively small compared to the wavelength ($\lambda \sim 1.6$ mm) whereas the

cross-sectional length of the transducer is relatively large (15 mm). This conveniently allows for the simplifying assumption that the transducer can be modelled in two dimensions of the central plane of the transducer. Although the same 2D assumption about the internal wall surface is not as realistic, Jarvis *et al.* [38] concluded that such 2D simulations still capture the majority of the physical interactions on the backwall surface. With the 2D assumption the DPSM model for shear horizontal waves is equivalent to an acoustic model and implies that no mode conversion takes place at interfaces, as the simulated displacement is perpendicular to the plane in which modelling takes place. Phenomena such as beam spread from the transducer, multiple scattering and diffraction effects are fully simulated.

DPSM can be used to simulate monochromatic waves, therefore in order to implement a temporal domain simulation, the frequency components of the excitation signal using the Fast Fourier Transform (FFT) are first calculated. DPSM then simulates the response of the system for each and every frequency component. The response of the simulated system can then be reconstituted in the temporal domain by applying an Inverse Fast Fourier Transform (IFFT).

The simulation problem is therefore simplified to considering a single frequency component at one time. The central assumption of the DPSM model is that a large number of point sources placed at a small offset from an interface can be used to model the wave excitation, reflection and transmission behaviour of that interface. In DPSM, point sources can be active or passive. Active point sources are used to simulate areas of predefined pressure, such as the interface of a transmitter transducer. Passive point sources are used to simulate interactions on boundaries, such as the backwall surface of a sample. The excited wavefield of active and passive point sources are identical, and is a function only of wave number, distance, time and angular frequency as described by the Green's function:

$$P(r,t) = AH_0^{(2)}(kr) \cdot e^{i\omega t} \tag{2.17}$$

where the P is the pressure at time t separated by distance r from the point source, k is the wave number, ω is the angular frequency, $H_0^{(2)}$ is the zero order Hankel function of the second kind and A is a complex constant relating to strength and phase of the wave excitation of the point source. It should be noted here that it is

only A that is unique to a point source.

The logic of how DPSM then simulates the wavefield is the following: n_a active point sources are placed close to the interface of the transmitter transducer as shown in Figure 2.4. Boundary condition equations prescribing the source pressure are set up at the interface below each active point source, resulting in n_a number of boundary condition equations. Because of this, the sum of the wavefields excited by the active point sources at those boundary points are known. This can be formulated as a linear system of equations:

$$\mathbf{P}_{BC} = \mathbf{Q}_{TS}\mathbf{A}_S \tag{2.18}$$

$$\mathbf{Q}_{TS} = \begin{bmatrix} H_0^{(2)}(kr_1^1) & H_0^{(2)}(kr_2^1) & \dots & H_0^{(2)}(kr_N^1) \\ H_0^{(2)}(kr_1^2) & H_0^{(2)}(kr_2^2) & \dots & H_0^{(2)}(kr_N^1) \\ \vdots & \vdots & \ddots & \vdots \\ H_0^{(2)}(kr_1^M) & H_0^{(2)}(kr_2^M) & \dots & H_0^{(2)}(kr_N^M) \end{bmatrix} \tag{2.19}$$

where $\mathbf{P}_{BC}$ is the vector of prescribed pressures at the boundary points, $\mathbf{A}_S$ is the amplitude constant associated with each active point source, $\mathbf{Q}_{TS}$ is the matrix of wave propagation equations (from Equation 2.17) from active point sources to the boundary points, N is the number of active point sources, M is the number of boundary locations and r_a^b is the distance between point source a to boundary point b. Since only the vector $\mathbf{A}_S$ is unknown, it can be calculated by:

$$\mathbf{A}_S = [\mathbf{Q}_{TS}]^{-1}\,\mathbf{P}_{BC} \tag{2.20}$$

Once the values in vector $\mathbf{A}_S$ are calculated, all variables associated with the active point sources are defined.

The same logic can be applied to compute the response of a reflecting surface. Namely a large number of passive point sources are placed at a small offset from the reflecting interface. The boundary condition of zero-pressure is then assumed on the backwall interface itself. Since the wavefield at the backwall boundary is equal to the sum of active and passive point sources, an equation similar to Equation 2.20 can be formulated, which in turn can be used to calculate the variables associated with the passive point sources. The total field response at any point can be calculated as a

sum of contributions from all active and passive point sources.

In the implementation used in this thesis DPSM relies on placing point sources close to the interface of the transducer and the backwall surface. An example of the geometry of such a setup is shown in Figure 2.4. Here, the transmitter transducer is simulated by 100 active point source with a radius of 5 µm offset from the transducer interface by 5 µm. The backwall surface is simulated by 800 passive point sources with a radius of 25 µm offset from the transducer interface by 25 µm. The receiver transducer is simulated by 50 receiver points that do not interact with the field placed on top of the interface.

The DPSM promises a simulation accuracy that has been shown to be as accurate as an equivalent FEM model but with a speed increase of an order of magnitude [11,38],

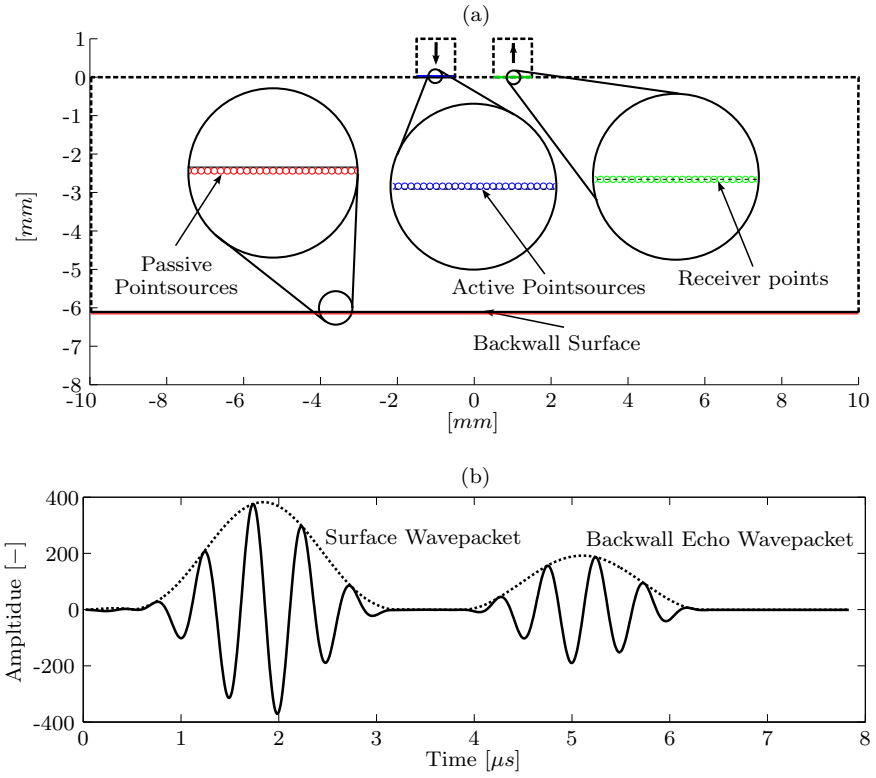

Figure 2.4: a) DPSM model of the permanently installed ultrasonic sensor on a flat backwall surface. Blue circles are the active point sources simulating the transmitter transducer. Red circles are passive point sources simulating the backwall geometry. Continuous black lines are shown where a zero pressure boundary condition has been applied. Dashed lines are purely for visual purposes only and therefore no boundary condition was applied to them. b) shows the simulated signal based on the model. The first wavepacket in the signal is the surface wavepacket. The second wavepacket is the backwall echo.

and hence is used as the primary simulation tool in this thesis.

2.6 Summary

In this chapter the basics of ultrasonic wave propagation have been summarised. After this, the concept of ultrasonic thickness measurements based on time-of-flight estimation was described. Throughout the thesis experimental validation of simulation results will be sought, therefore a particular transducer setup for testing results is required. The SH waveguide transducer was chosen because it is readily available and used for monitoring in the field. The general features of the waveguide transducer were described in this chapter, as it will be used for most experimental measurements. A number of variables were highlighted that are expected to influence the variability of the wall thickness measurement (*e.g.*: the contact patch of the waveguide transducer, coherent noise caused by the waveguide transducer, arrival time estimation, determination of ultrasonic propagation velocity etc.). These variables and their effect on the ultrasonic measurement is central to this thesis, and are therefore investigated systematically in the next chapters. The concept and advantages of permanently installed monitoring were then explained, emphasising their potential for thickness measurement repeatability and accurate mean wall thickness loss rate estimates. Following this, the DPSM was presented as the primary ultrasonic wave simulation approach to be used in this thesis.

Chapter 3

Uncertainty in Arrival Time Determination (Signal Processing)

3.1 Introduction

The aim of this thesis is to maximise the accuracy to which ultrasonic degradation monitoring measurements are carried out. For this purpose, the previous chapter has introduced the concept of permanently installed ultrasonic monitoring and elaborated on how high precision ultrasonic monitoring can be realised. In order to maximise the precision of estimated wall thicknesses, it is also important to implement a signal processing protocol with good noise rejection. This chapter is aimed principally at minimising random noise and its effects on ultrasonic measurements. Systematic error sources, mostly associated with experimental factors such as the effect of temperature, are investigated in Chapter 4 and are not considered here. This chapter is organised as follows:

The first section describes a robust signal processing protocol that was found to result in accurate ultrasonic wall thickness measurements. This is presented early on as it is a very good overview of all the signal processing steps that are required. Following this, the various studies and investigations that were used to arrive at this final protocol are presented. The performance of this setup is demonstrated using the waveguide sensor. In addition, results showing the expected performance of

transducers with different excitation frequencies and characteristic SNRs compared to the waveguide sensor are also described.

3.2 Signal Processing Protocol Overview

Here a specific signal processing implementation is presented, that was developed to maximise wall thickness measurement precision. The final protocol that was found to perform best is as follows:

- A 2 MHz 5-cycle Von Hann-windowed (sometimes referred to as Hanning-windowed) toneburst is produced to be used as excitation signal
- The excitation signal is digitised at 50 MHz sampling frequency, 14bit resolution and ±12 V amplitude using suitable hardware
- The excitation signal is sent to the transducer
- The response is measured on the receiving transducer at 50 MHz sampling frequency and 12bit resolution
- A bandpass filter is applied to the received signal using a 5^{th} order Butterworth filter between frequencies 1.6 MHz and 2.4 MHz
- The signal is averaged 320 times
- The signal is upsampled to a virtual sample frequency of 512 MHz
- Arrival times of consecutive echoes in the signal are estimated using cross-correlation (XC) and linear interpolation between samples to find the peak of the XC function with the best possible precision

Experimentally measured wall thickness estimates using this signal processing protocol are shown in Figure 3.1 to demonstrate the performance of this protocol. The standard deviation of these wall thickness estimates is 14 nm, therefore verifying that very high repeatability can be achieved. This signal processing protocol was the conclusion of a series of investigations of how certain parameters related to the signal acquisition process affect arrival time precision. These will be described in the following order:

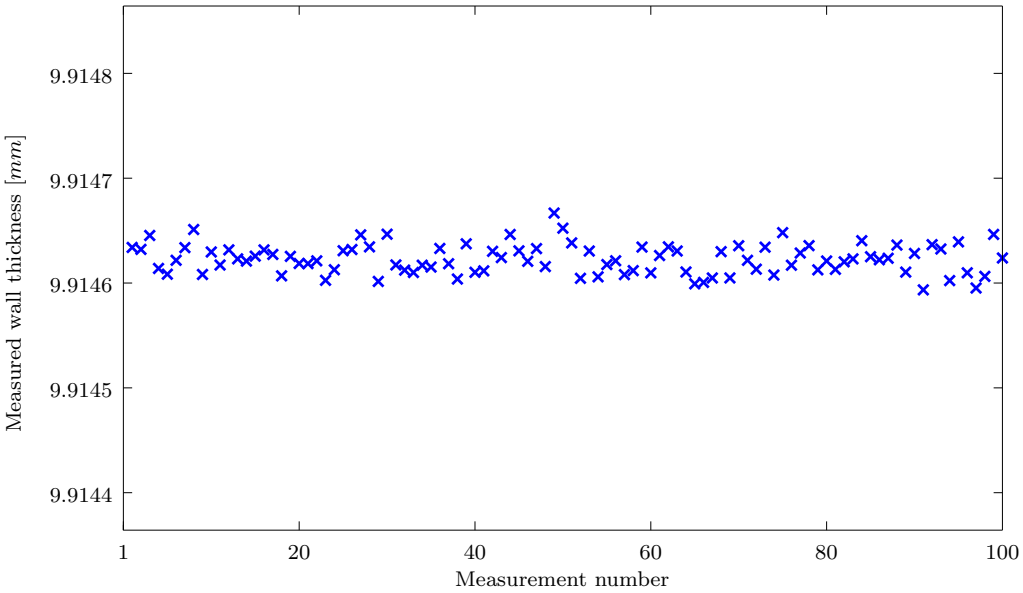

Figure 3.1: Wall thickness measurements based on experimentally acquired signals following the outlined signal processing protocol. The standard deviation of measurements is 14 nm.

- Performance comparison of arrival time estimation methods
- Interpolation methods with various signal acquisition settings
- The effect of raw waveform signal to noise ratio (SNR) on the uncertainty in estimated arrival time
- The choice of frequency of the excitation signal

3.3 Performance evaluation using the waveguide sensor

3.3.1 Comparison of arrival time estimation methods

In order to accurately estimate the wall thickness of a sample, accurate arrival time estimation is key. Here techniques that are typically used for arrival time estimation are discussed. Their implementation is also described, and the repeatability of estimated wall thicknesses using each method is then compared in simulations.

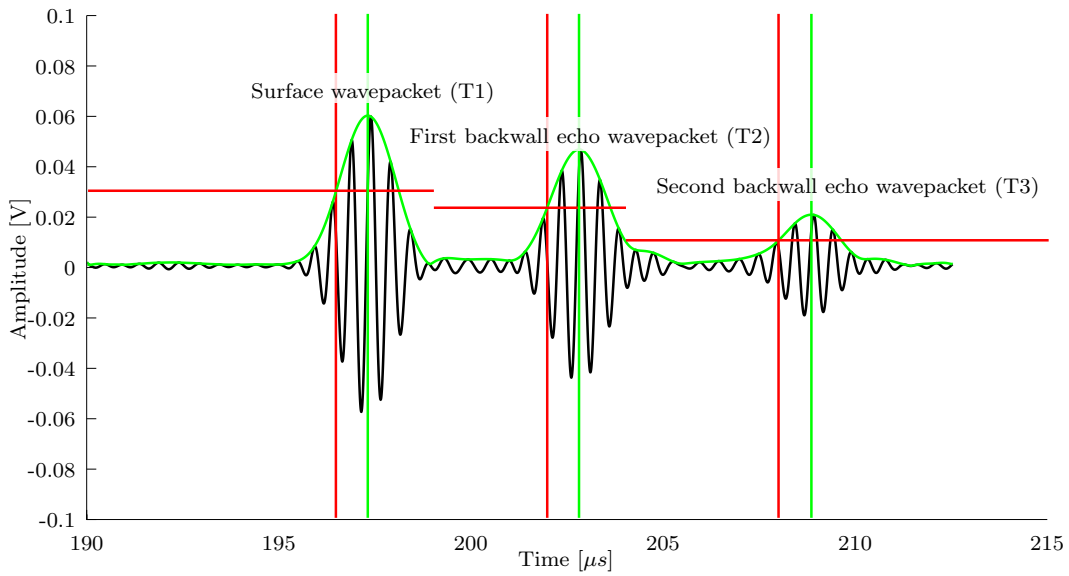

Figure 3.2: The figure shows the Hilbert-envelope (green line) of a sample waveform (black line) and its estimated arrival times using P2P (green vertical lines). Red horizontal lines show the calculated thresholds for each wavepacket. FA arrival times calculated based on the intersection of thresholds (6dB here) and the Hilbert envelope are also displayed (red vertical lines).

A commonly used arrival time estimation concept is based on calculating an envelope function for the waveform [39]. These methods are often referred to as Envelope Peak or Peak-to-Peak (P2P) methods. In this thesis the P2P notation is used throughout to avoid confusion. Some P2P methods use the raw signal, but most rely on computing an envelope function for the measured waveform. This ignores phase information and is believed to be more robust. One way to achieve this is via the Hilbert-transform. The Hilbert transform applies a 90° phase shift to all frequency components of the signal [40], hence it can be used to calculate the envelope of the signal by:

$$E(t) = \sqrt{f\left(t\right)^2 + H\left(f\left(t\right)\right)^2} \tag{3.1}$$

where $f(t)$ is the function for which the envelope is calculated, $H\left(f\left(t\right)\right)$ is the Hilbert transform of $f(t)$ and $E(t)$ is the computed envelope. A sample waveform along with its Hilbert-envelope is shown in Figure 3.2. Other methods exist that compute a similar envelope function, such as filtering using finite impulse response (FIR) filters [41, 42]. The result however is fundamentally the same as a band-pass filter and the Hilbert-transform, namely an envelope function with a limited

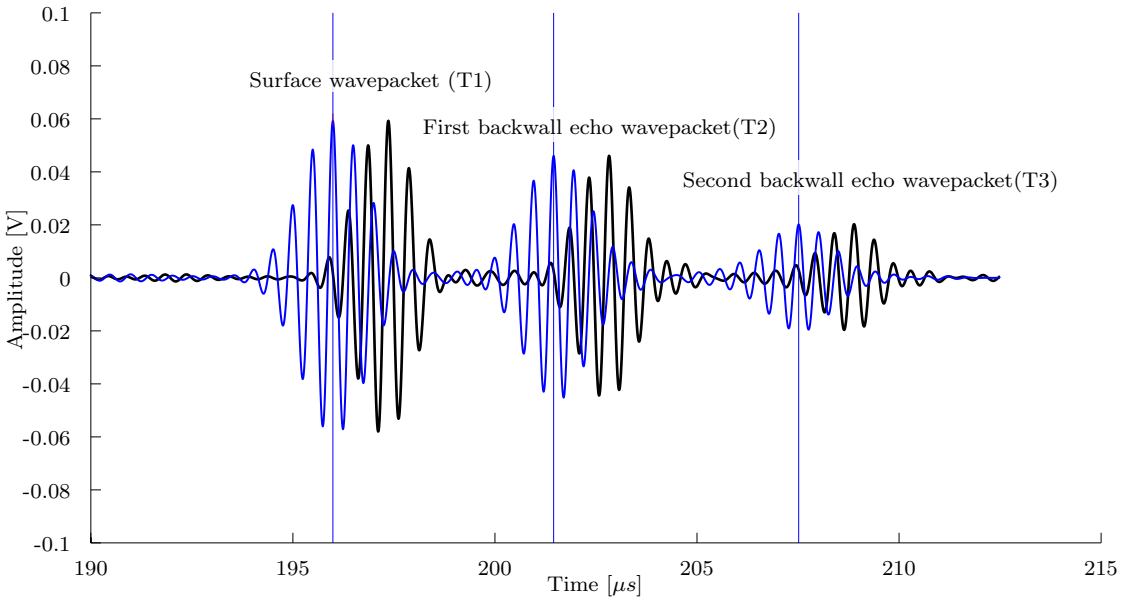

Figure 3.3: The figure shows the cross-correlation function (blue line) of a sample waveform (black line) with a synthetised 180 ° toneburst and the estimated arrival times of that waveform using XC (blue vertical lines).

frequency spectrum, where the phase information is ignored. Based on the computed envelope, the arrival times of the various wavepackets are estimated by determining the maximum peaks of the envelope function. P2P methods are simple to implement. The calculation of the envelope is straightforward and since typically only a small number of peaks are present in it, their identification is easy and can be robustly automated.

First-Arrival (FA) is another method to estimate arrival times of wavepackets [11]. It also relies on calculating an envelope function and finding the peaks of that function. FA then establishes a threshold as a function of the amplitude of each peak - *e.g.* the threshold for the each wavepacket is determined as -6 dB of its amplitude. Since for each wavepacket this threshold is determined independently, the threshold for each wavepacket will be different. The crossing of this threshold and the envelope function is then taken as the arrival time for a given wavepacket. This is shown in Figure 3.2 directly compared to a P2P arrival times. Since FA is based on an envelope as well, it is only marginally more complex to implement than P2P methods.

Cross-correlation (XC) is another popular arrival time estimation method [11, 39]. Cross-correlation is defined as the sliding dot product of a function with the complex conjugate of another. In the context of arrival time estimation, cross-correlation

behaves as a form of similarity metric between two signals as a function of time-lag. This can be used for arrival time estimation by cross-correlating the synthesised toneburst that is transmitted at the beginning of a measurement with the received signal. An example of a correlation function is shown in Figure 3.3. The peaks of the resulting cross-correlation function therefore represent the times where the two functions correlate well. The arrival times of the wavepackets in the waveform are then estimated by determining the time of the biggest peaks in the cross-correlation function.

A difficulty that may arise during this process is that in some cases the received wavepackets may be distorted compared to the sent toneburst. Phase shifts in the received signal are a typical form of distortion, caused by characteristics of the transducer itself, coupling to the sample and reflections from various interfaces in the sample. It is assumed here that such shifts do not occur after a given transducer has been coupled and so repeatability is assumed to be unaffected.

Beyond these three fundamental methods, there have been reports suggesting that combining some of them may result in more accurate arrival time estimation algorithms. Yu [39] proposes to estimate arrival times by calculating the envelope function of the received waveform and cross-correlating it with the envelope function of the sent toneburst. In the report by Yu [39], it was recognised that this approach was chosen since the standard P2P method appeared to be unstable because of what was described as dispersion effects. In this thesis it is assumed that signals are dispersion-free, in which case such an approach is not expected to offer any advantages.

In addition, other more complex methods also exist that can be used for arrival time estimation. The wavelet transform is one of the many possible methods that can be used for feature detection and arrival estimation [43]. Its potential has been recognised for defect detection, since it can be used to describe the temporal distribution of harmonic components [43]. However, such a method offers limited advantages in this thesis, since here the frequency spectrum of the reflection of ultrasonic waves is well defined and not expected to change. Since only the temporal shift of wavepackets is to be determined in this thesis, cross-correlation is expected to estimate arrival times with similar accuracy, hence the wavelet transform is not investigated in this

thesis. The split-spectrum processing (SSP) method is another possible candidate for arrival time estimation [43]. SSP is also based on multi-frequency analysis, and therefore SSP is also omitted from this investigation for similar reasons.

Three arrival time estimation methods - P2P, FA and XC - were evaluated to find which method is capable of determining arrival time with the highest precision. The chosen methodology for this is as follows: a signal is simulated using the previously presented DPSM method by transmitting a 2 MHz 5 cycle Hann-windowed toneburst that has been reported to work well with the waveguide transducer [25] into a sample with a uniform wall thickness of 10 mm. This signal is simulated at 512 MHz sampling rate. No quantisation error is introduced (other than what is implicit in a double precision variable), therefore ideal sampling resolution is assumed. It is expected that the random noise level for a single raw experimentally measured waveform using a waveguide is approximately -52 dB, therefore -52 dB white Gaussian noise is added onto the simulated signals. Here, signal to noise ratio is interpreted as the ratio of the standard deviation of random noise and the maximum amplitude of the signal. The noiseless simulated waveform and the signal with added noise are shown in Figure 3.4.

The simulated signal is then filtered and averaged 320 times following the outlined

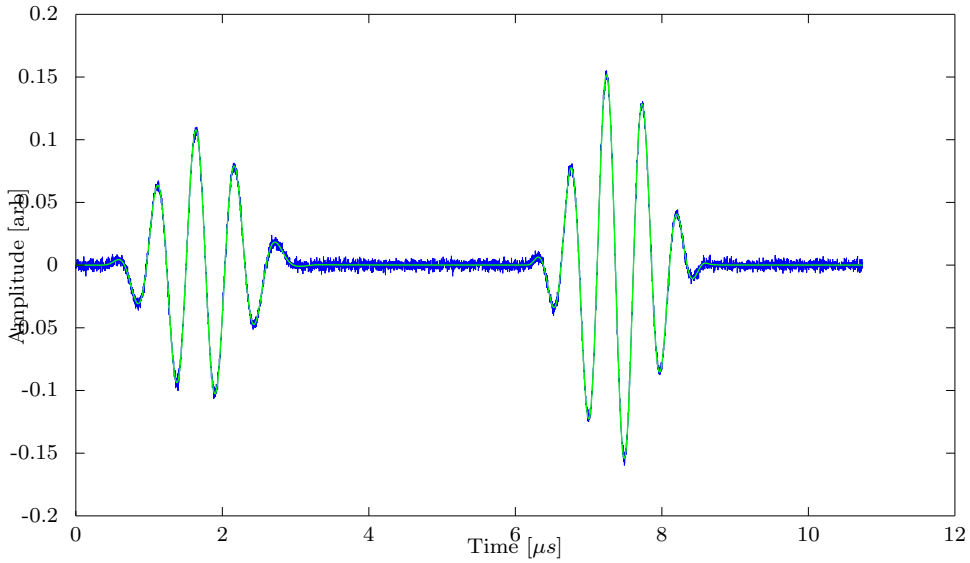

Figure 3.4: Simulated waveform using DPSM (green line). Signal with added -52 dB white Gaussian noise (blue line).

signal processing protocol. Since it is the repeatability of arrival times that is of interest, altogether 100 averaged waveforms are simulated using this protocol. These 100 waveforms are then evaluated using all three arrival time estimation methods. It should be noted that although waveforms are simulated with parameters that are characteristic of the waveguide transducer (*i.e.* characteristic SNR and transducer geometry), it is thought that the comparison of arrival time estimation methods is not specific to this transducer and the comparison is expected to apply to other transducers using a different geometry with signal to noise ratios of similar order of magnitude.

The distribution of calculated thicknesses for all three methods are shown in Figure 3.5 and their standard deviations are shown in Table 3.1. It is clear that the variability of XC is approximately an order of magnitude lower than any other method, which is as expected because of its better noise suppression compared to other considered methods. Because of this, XC is used as the default arrival time estimation method throughout this thesis.

In addition, it should be noted here that the absolute accuracy of all methods appears to be comparable. The mean thickness calculated in simulations for XC is 10.065 mm, for P2P it is 10.123 mm and for FA it is 10.175 mm. It is expected that the small differences come from small biases of each method, which may possibly be compensated. This is not considered here, since this performance evaluation is

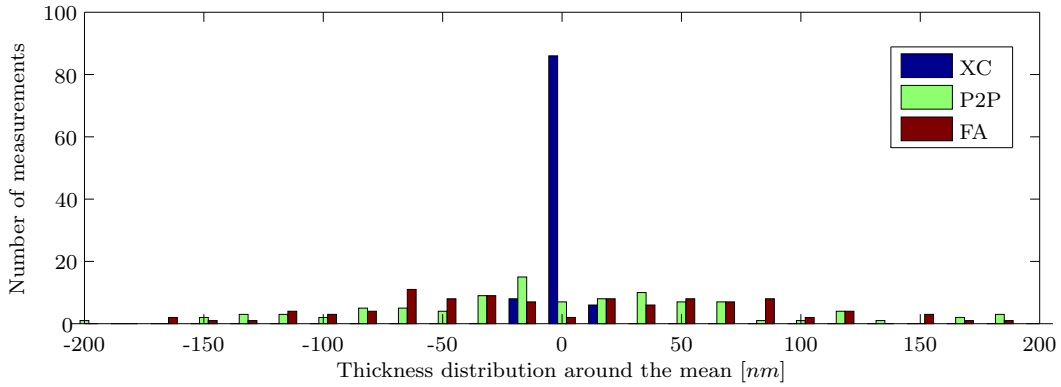

Figure 3.5: Distribution of calculated thicknesses using all three signal processing methods for simulated signals. XC thicknesses are shown in blue, P2P results are shown in green and FA results are shown in red. All distributions are shown for each method around their corresponding mean calculated thickness.

STD of arrival time [ps]			STD of thickness [nm]		
P2P	FA	XC	P2P	FA	XC
53.9	51.6	3.63	88.1	84.4	5.95

Table 3.1: Standard deviations of time differences between backwall echo and surface wavepacket in the left three columns. In the right three columns, the standard deviations of thicknesses are shown. All values calculated for a simulated plate with a wall thickness of 10 mm and an ultrasonic velocity of 3250 m/s

aimed solely at improving repeatability, and since XC offers the best repeatability, no further effort is put into evaluating other methods.

3.3.2 Evaluation of Signal Acquisition and Interpolation

It has been demonstrated in the previous section that very high wall thickness estimate precision is achievable using XC. These simulations however assumed that signals can be acquired at very high sampling rates without any quantisation error. In practice however signal acquisition hardware capable of high sampling rates and quantisation levels may be costly. In addition, signal acquisition hardware has to be deployed for each permanently installed sensor, and therefore the cost and complexity of the signal acquisition hardware is expected to be critical. Hence, it is of interest to investigate how low the parameters of the signal acquisition hardware can be kept while still maintaining high precision for thickness estimates. This was evaluated next.

The parameters of the signal acquisition instrument that are considered here are sampling frequency and maximum number of quantisation levels as both of these parameters may limit precision. First, limitations associated with sampling frequency are discussed. The entire frequency spectrum of a toneburst with a centre frequency of 2 MHz that is used with the waveguide sensor is below 4 MHz, which means that according to the Nyquist-Shannon sampling theorem 8 MHz sampling rate is sufficient to avoid aliasing. It should be recognised however, that this finite signal sampling potentially limits the precision of extracted arrival times as the correlation functions that are used with XC are calculated with the same sampling frequency basis as the waveform they are based on. Hence, peaks that are extracted from these waveforms will also be limited by the sampling frequency. In order to overcome

this limitation in accuracy, interpolation to increase the potential accuracy of the extracted arrival times beyond the sampling limit is employed.

A typical interpolation approach is to fit a proxy curve to the function to be interpolated. The proxy curve can then be differentiated and its peaks can be determined more accurately than that of the original function. This approach was adopted by Honarvar *et al.* [44]. In the report by Honarvar. [44] polynomial interpolation scheme was used, where the order of the fit and number of points to be used were parameters that have to be determined based on the system itself.

As an alternative to this approach, an interpolation scheme based on the discrete Fourier transform (DFT) is described here, which aims to increase the virtual sampling frequency of signals. As previously stated, the highest frequency component of the toneburst that is used in this thesis is approximately 4 MHz, therefore a sampling frequency of just 8 MHz satisfies the Nyquist-Shannon sampling criterion. Once a signal has been sampled at sampling rate of 8 MHZ or above, it is possible to apply a DFT to that signal, and zero-pad it in the frequency domain. This zero-padding explicitly asserts that the unmeasured frequency components are zero. Following this, an inverse DFT is applied, resulting in an increase of virtual sampling rate [45, 46]. The amount of increase in virtual sampling rate is a function of the zero-padding in the frequency domain: doubling the number of points in the frequency domain results in doubled virtual sampling frequency in the time domain. This method of zero-padding in the frequency domain for the benefit of increase in virtual sampling frequency is referred to as upsampling in this thesis.

It should be recognised that upsampling waveforms to very high frequencies is not practical. Instead, upsampling is used in combination with interpolation. The signal processing protocol evaluated here therefore first upsamples a waveform and then applies a linear fit to its slope to interpolate the arrival of wavepackets.

The performance of this interpolation method is evaluated using various sampling parameters by simulating signals with DPSM and superposing white Gaussian noise to achieve an SNR of 52 dB. An example of such a waveform was shown in Figure 3.4. Once the noise has been superposed onto the signals, they are quantised either with 8bit, 10bit or 12bit precision, as these are thought to be conservative quantisation

320 averages		Upsampled				No upsampling			
			Quantisation				Quantisation		
			8bit	10bit	12bit		8bit	10bit	12bit
Sampling	8 MHz	8 MHz	21.9	17.4	18.3	8 MHz	179	135	131
	16 MHz	16 MHz	18.1	11.6	11.4	16 MHz	18.9	12.1	12.3
	32 MHz	32 MHz	13.4	8	8.4	32 MHz	14.3	7.9	8.3
	64 MHz	64 MHz	10.9	6.4	5.8	64 MHz	10.3	6.4	6.1

Table 3.2: Standard deviation of estimated thicknesses [nm] on a 10 mm thick simulated sample based on waveforms with 52 dB white Gaussian noise averaged 320 times. The left column shows results with upsampling to 512 MHz, whereas the right column shows results without upsampling.

levels. Waveforms are simulated at 4 different sampling frequencies: 8, 16, 32 and 64 MHz. Altogether 200 waveforms are generated for each parameter set, each of them an average of 320 raw quantised waveforms following the defined signal processing protocol. This process is carried out both with upsampling to 512 MHz, and also without any upsampling. The resulting standard deviations are shown in Table 3.2.

It can be seem from Table 3.2 that increasing quantisation resolution or sampling rate are both favourable in all cases. The data in the table also reveals that upsampling can decrease variability by approximately 80% when sampling frequency is low (8 MHz), but it does not make a significant difference for results at high sampling frequencies (64 MHz). It is assumed that this is because linear interpolation of slope is accurate for sampling frequencies of 64 MHz and higher. It is expected therefore that upsampling to approximately 64 MHz is effective in decreasing measurement variability, but higher virtual sampling frequencies are of no real benefit.

In order to verify these results experimentally, a Handyscope HS3 (TiePie engineering, Sneek, Netherlands) was selected for signal generation and acquisition purposes. The technical specifications of this instrument are as follows: output impedance: 50 Ohm, input impedance: 1 MOhm, output signal amplitude: ±12 V peak-to-peak, maximum sampling rate for signal generation and acquisition: 100 MHz, quantisation for signal generation: 14bits, quantisation for signal acquisition: 8bits at 100 MHz or 12bits at 50 MHz.

Beyond the considerations of the appropriate signal acquisition parameters that have already been discussed in this section, it is also critical to make sure that various

impedances in the signal generation circuit allow for efficient signal propagation into and out of the transducers. The output impedance of the Handyscope is quoted to be $Z = 50$ Ohm. The selected waveguide sensor relies on piezoelectric transducers, which are generally considered high impedance in electric circuits at low frequencies. At 2 MHz however, the impedance of piezoelectric transducers is expected to be of the order of $Z \sim 100$ Ohm [47]. Although the impedance of the specific piezoelectric element used for the waveguide sensor has not been characterised, its impedance is also expected to be of similar order of magnitude. Therefore the sending transducer can be directly connected to the signal generator of the Handyscope resulting in good power transfer. Since the impedance of the resulting transduction circuit is of the order of $Z \sim 150$ Ohm, the Handyscope is expected to be able to provide the necessary power without amplification required *i.e.* a current of 80 mA= $\frac{12\text{ V}}{150\text{ Ohm}}$ at its rated 12 V output voltage. As for the receiver piezoelectric transducer, this can be modelled as a voltage source as a basic approximation [48]. Measuring signals from the receiver transducer is therefore directly possible using the high input impedance ($Z = 1$ MOhm) input channel of the Handyscope.

Using this setup, 100 waveforms were collected, each the average of 320 raw waveforms. These waveforms were then processed using the signal processing protocol described in this chapter. The resulting thicknesses are shown in Figure 3.1. In the figure it is also shown that the standard deviation of the wall thickness estimates is 14 nm, hence confirming that it is possible to acquire wall thicknesses at this precision using the waveguide sensor.

In summary, it is concluded that even at very modest sampling frequencies (8 MHz) and quantisation resolutions (8bits) it is possible to achieve a repeatability of the order of tens of nanometres (using the 5-cycle 2 MHz centre frequency toneburst). This was then verified experimentally using a waveguide sensor. Achieving even higher repeatability is theoretically possible, it is expected that experimental issues, such as temperature fluctuations, limit repeatability. Increase in repeatability is therefore not pursued any further with this setup. Instead, the next sections evaluate whether similar precision can be achieved using sensors other than the waveguide sensor.

3.4 Performance evaluation using generic transducers

The previous sections demonstrated that wall thickness estimates with a variability of the order of tens of nanometres can be measured using the waveguide sensor with the signal processing protocol described in this chapter. The protocol that was used for this is expected to perform well with other transducers as well, but it is of interest to quantify differences in performance. Different transducers may have different characteristic SNRs or may be sensitive to different frequency ranges compared to the waveguide transducer. In this chapter these two variables are investigated. First, it is quantified how averaging can be used to improve SNR. Secondly, it is evaluated how the choice of excitation signal frequency affects the precision of estimated wall thicknesses.

3.4.1 The effect of waveform SNR

The response of the ultrasonic measurement system will always be affected by random noise regardless of the chosen transducer. It is acknowledged that this measured noise is inherent in the analogue circuit [49]. In order to investigate how transducers of various SNR perform in ultrasonic measurements, it is critical to first clarify how the SNR can be improved in processing and how it affects measurements. As part of the signal processing protocol discussed here, filtering and averaging is applied to measured waveforms to mitigate the effect of random noise. The details and limitations of this are described here.

The frequency spectrum of the toneburst that is used to excite the transducer, such as the waveguide sensor, in an ultrasonic measurement is relatively narrow, therefore frequency selective filtering is possible. This is achieved by attenuating the frequency components of the received signal that are not components of the sent toneburst, ideally without affecting the frequency components that are intentionally excited. A 5^{th} order Butterworth band-pass filter is selected for this purpose, also known as a maximally-flat magnitude filter [50]. As established, a toneburst with a centre frequency of 2 MHz was selected for the waveguide sensor, therefore the cut-off

frequencies of the filter are set to be 1.6 MHz and 2.4 MHz. The interested reader can find the frequency response of the Butterworth filter in [50].

In addition, averaging waveforms is a straightforward approach to attenuate the components of random noise that are indistinguishable from the components of the excited signal based on frequency selective filtering. The basic concept of averaging is simple: measure a large number of waveforms in quick succession, and numerically average the measured signals. In implementation however, it is difficult to take advantage of averaging a large number of waveforms, as averaging a large number of waveforms can take excessively long. This is an issue because the concept of averaging relies on the assumption of stationary signals, which is increasingly likely to break down if averaging takes place over longer periods of time. The maximum time limit over which waveforms are practical to average is not investigated here however, as this is expected to be highly specific to a given experimental setup *e.g.* measuring 320 waveforms to average using the Handyscope takes 21 seconds. Hence it is assumed that of the order of 300 averages is near the practical limit using the waveguide sensor in experiments.

A simple way to evaluate performance of averaging is to estimate the improvement in signal to noise ratio that can be achieved with it. The signal to noise ratio of raw waveforms acquired using the waveguide sensor is assumed to be $52dB$ (with SNR interpreted as the ratio of the standard deviation of noise and the maximum amplitude of the signal). A large number of waveforms are therefore generated by adding $52dB$ white Gaussian noise onto noise-free simulated signals.

Figure 3.6 shows the improvement in SNR using averaging. The SNR of waveforms is plotted against the number of averages. Using the data on this figure, it is possible to estimate how raw waveforms with signal to noise ratios other than 52 dB perform when processed using these techniques. Figure 3.6 shows that the relationship between the logarithm of averages and SNR is linear with a slope of 10 dB/decade. This is consistent with the theory that the standard deviation of a random variable when averaging independent measurements is expected to decrease by the square-root of the number of averages [51]. As a rule of thumb, it is interesting to note therefore that if the SNR of the raw signal measured by a different transducer is for example 42 dB (*i.e.* 10 dB less than the waveguide sensor), the number of averages would

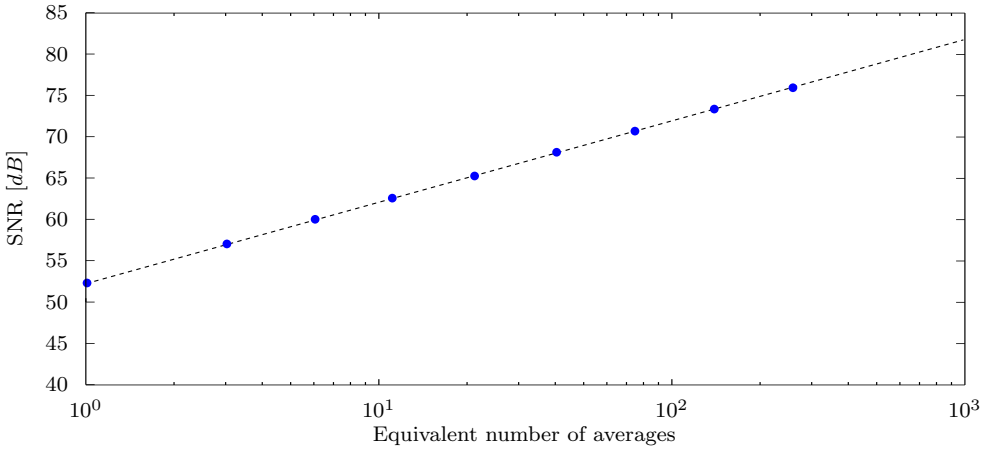

Figure 3.6: Signal to noise ratio of waveforms acquired with averaging (blue circles). A linear fit to measured SNRs is also shown (dashed black line).

need to be increased by a factor of 10 to reestablish an SNR of 52 dB.

3.4.2 Thickness STD improvement as a function of SNR

In addition to quantifying how SNR is affected by various transducers and as a function of averaging, it is also of interest to evaluate how the SNR improvement translates into improvement of wall thickness estimate precision. This is investigated in this section.

Similarly to previous sections, here waveforms were generated with 52 dB white Gaussian noise added. These 5-cycle Hann windowed 2 MHz signals were simulated with a sampling rate of 64 MHz and quantisation of 12bit. The signals were then averaged in groups of $2, 4, 8, 16..256$ resulting in SNRs of $52, 55, 58, 61..72$ dB. Both band-pass filtering and upsampling to 512 MHz were applied. The waveforms were then processed using XC. The standard deviation of resulting thicknesses is shown in Figure 3.7 as a function of SNR.

It has been explained in the previous section that if the SNR of a raw waveform is decreased, it is possible to increase the number of averages to compensate. Based on Figures 3.6 and 3.7 therefore it is possible to estimate the precision of wall thickness estimates using transducers of arbitrary SNR. As an example, consider the waveguide

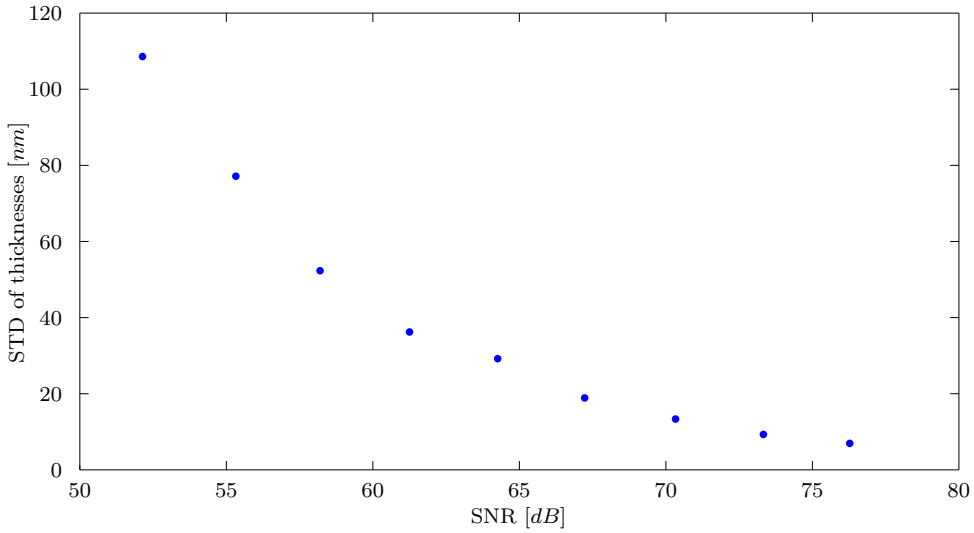

Figure 3.7: Standard deviation of thicknesses using XC as a function of SNR for waveforms acquired using averaging (blue circles) where the excitation signal was a 5-cycle Hann windowed 2 MHz toneburst. SNR was measured as the maximum amplitude of the signal divided by the standard deviation of the noise.

transducer in a pitch-catch arrangement, which is capable of acquiring signals of 52 dB SNR. Averaging 320 raw signals an SNR of 76 dB is achieved resulting in a wall thickness precision of 6 nm.

3.4.3 Alternative Excitation Signal Frequencies

Most transducers are expected to differ from the waveguides not only in their characteristic SNRs but also in frequency characteristics. It has been explained that the waveguide is limited to excitation frequencies near 2 MHz. Other transducers may work well with other frequencies, and hence it is of interest to evaluate what frequency ranges may result in the most repeatable thicknesses. This section therefore investigates how the variability of wall thickness estimates changes as a function of excitation frequency.

An example simulated waveform that can be acquired using a 2 MHz 5 cycle toneburst as excitation on a 10 mm thick sample is shown in Figure 3.8 using a pitch-catch setup such as the waveguide sensor. In addition, two more waveforms are also shown, one acquired using a 0.85 MHz 5 cycle toneburst and another with a 20 MHz 5 cycle toneburst. As can be seen from the figure, frequencies lower than 0.85 MHz

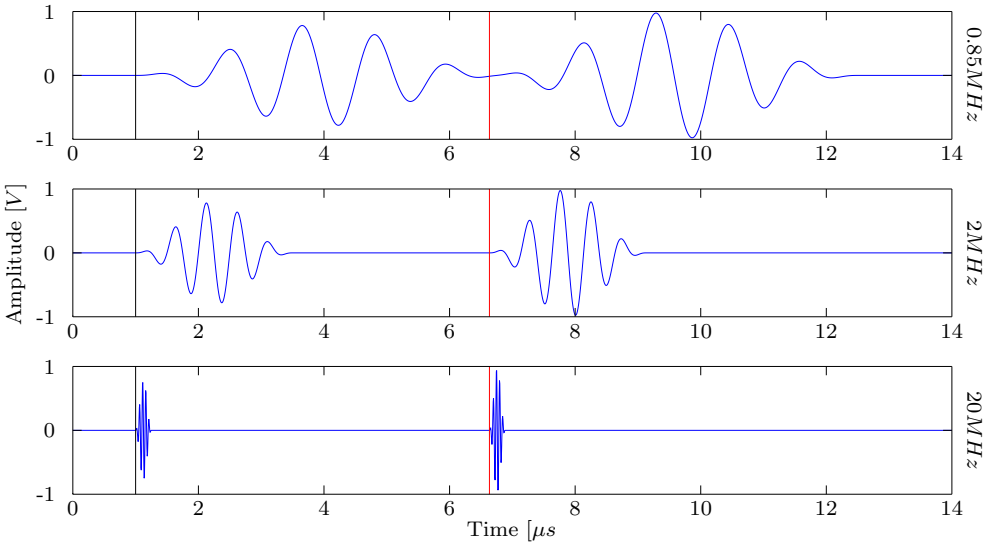

Figure 3.8: Figure shows 3 ultrasonic signals on a 10 mm simulated sample using various frequency tonebursts. Top graph was simulated with a 0.85 MHz toneburst, the middle graph with a 2 MHz toneburst and the bottom graph with a 20 MHz toneburst.

would result in the wavepackets overlapping when the wall thickness of the measured component is less than 10 mm and hence are not considered practical for any setup regardless of transducer.

Frequencies higher than 0.85 MHz however are feasible to use and it is of interest to see how varying frequency affects the precision of wall thickness precision. To evaluate this, here a large number of signals were simulated with DPSM using tonebursts of various frequencies as excitation that were transmitted into a sample with a uniform wall thickness of 10 mm. The frequency range between 0.85 MHz and 20 MHz was evaluated here. Signals were simulated with sampling rates of 512 MHz and without any quantisation error introduced. In addition, white Gaussian noise was added onto the signals to simulate real behaviour. Three signal to noise ratio values were investigated: 42,52 and 62 dB. The results of estimated wall thickness variability are shown in Figure 3.9.

As Figure 3.9 shows, the variability of estimated wall thicknesses decreases with frequency when signal to noise ratio is constant. It should be noted however that in practice higher attenuation is typically associated with higher frequencies [52]. Hence, the SNR is expected to decrease with high frequency bursts and as a result

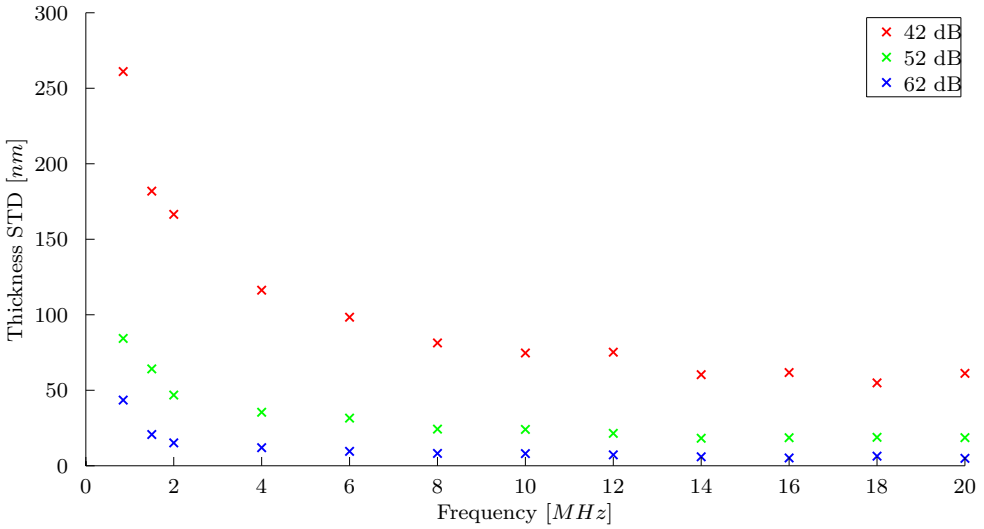

Figure 3.9: Standard deviation of wall thicknesses using tonebursts of various frequencies for excitation with signal to noise ratios of 42 dB (shown in red), 52 dB (shown in green) and 62 dB (shown in blue).

repeatability may not improve. Although the waveguide transducer is limited to using a 2 MHz toneburst, it is therefore expected that this does not impose a significant limitation on precision.

3.5 Conclusions

This section has presented a signal processing protocol that can measure ultrasonic wall thickness at very high precision. One of the key findings of this chapter was that arrival time estimation is most precise using cross-correlation (XC) which was therefore used in the protocol. In addition, the effect of averaging on both SNR and thickness precision was quantified. It has also been shown that it is critical to use an excitation signal with a centre frequency of 2 MHz or more to avoid the overlap of wavepackets and maximise precision.

The performance of the final signal processing protocol was demonstrated in experiments using the waveguide sensor. It has been shown that a wall thickness standard deviation of 14 nm can be achieved in laboratory conditions. Even when the sampling rate was limited at 8 MHz and quantisation was limited to 8bits a standard deviation of 21 nm was shown to be achievable.

Chapter 4

Uncertainty in Experimental Measurements

4.1 Introduction

The previous chapter has discussed and evaluated potential error sources in signal acquisition and processing. Discussion of experimental issues has been limited to those directly involved in signal acquisition (*e.g.*: signal quantisation). Within the context of this thesis, this chapter is aimed at investigating the most common experimental error sources in order to further increase precision of ultrasonic measurements. Discussed topics include measurement errors associated with coherent noise, coupling variability as well as compensation of the effects of temperature.

Coherent noise is the first of the common issues considered here. In ultrasonic signals coherent noise is frequently caused by imperfect transducers or backscatter from structural features such as large grains. Coherent noise cannot be reduced via averaging, as it is stationary. In the experiments performed in this thesis the most significant source of coherent noise is the imperfect waveguide transducer. The noise in this case consists of unintentionally excited modes that propagate at different velocities in the waveguide. Such coherent noise can be observed as a form of tail after each wavepacket in the signal. As the tail of a preceding wavepacket may not die down before the next wavepacket arrives, a form of systematic error in arrival

time extraction may be introduced.

Another error source that was investigated is the variability of coupling to the sample. In order to provide measurements with as little variability as possible, it is critical for signals from permanently installed ultrasonic sensors to remain as constant as possible. It is however relatively difficult to maintain constant coupling over long periods of time and under different environmental conditions. Sensors may be expected to operate for multiple years, during which the couplant may dry out or bonding material may change properties [53]. For the particular case of the waveguide sensor, dry coupling is used, which is thought to be relatively robust compared to other coupling techniques. It is expected that differential thermal expansion of the attachment assembly may still introduce fluctuations in coupling pressure as the temperature of the monitored component changes. Hence, some changes in coupling are expected in practice and were investigated.

Beyond error sources specific to the sensor technology that is used, external factors such as temperature changes of the sample may also introduce error in the measurement. Previous sections have highlighted that temperature compensation is key to achieve highly repeatable thickness measurements. This section first looks at calibration curves for temperature compensation for different materials. In order for the compensation to be effective in application, it is clear that it is critical to measure the temperature of the sample accurately. Since monitoring high temperature pipes is an important application for permanently installed sensors, temperature gradients are expected to be present in the pipe wall. This implies that the outside pipe surface, where temperature compensation measurements can be carried out, may not accurately reflect the effective temperature of the full depth of the pipe wall. This temperature gradient effect may limit the accuracy of temperature compensation and hence was investigated.

In addition, inner wall surface morphology may also influence the accuracy of thickness measurements. Uneven inner wall surface geometry, or rough backwall surfaces, cause distortion in the ultrasonic signal that is reflected from them. Since ultrasonic measurements rely on this reflection to determine arrival times and the thickness of the sample, such distortion can significantly increase the variability of thickness measurements. This interaction is relatively complex however, and was

therefore investigated separately in Chapter 7.

4.2 Coherent noise

Coherent noise is a common phenomenon that affects ultrasonic signals. For permanently installed ultrasonic sensors, backscatter from grains is a typical source of coherent noise, since spatial variations cannot be taken advantage of [54]. Other potential sources of coherent noise include imperfect coupling or inherent transducer limitations such as ringing [55] or multiple modes propagating at different velocities in a waveguide transducer [25]. This section focuses on the effects of coherent noise on estimated time of flights regardless of the source of the noise.

An example waveform affected by coherent noise is shown in Figure 4.1.a. This waveform was measured using the previously described waveguide transducer on a 10 mm thick mild steel sample. In this case, it is apparent that unintentionally excited modes of the waveguide sensor contribute to the measured waveform between the main wave packet arrivals. It is also apparent in Figure 4.1.a. that very little noise is measured before the surface wave, it is therefore concluded that these unintentionally excited modes propagate slower than the signal itself, therefore coherent noise in this example appears as a tail after each wavepacket.

In order to investigate this behaviour, a simple simulation model was used. First, a pulse-echo measurement is carried out using a single waveguide without a sample attached. A waveguide transducer with a SNR of 16 dB has been selected for this. This SNR value was measured as the maximum amplitude of the pulse echo reflection divided by the maximum amplitude of coherent noise measured 2.5 cycles after the main arrival in the same waveform (shown in blue in Figure 4.1.a.). This is thought to result in relatively conservative error estimates, since it has been reported that 30 dB or better SNR is usually achieved using the waveguide transducer [24]. The result of a pulse-echo measurement is a wavepacket that has travelled in both directions in the waveguide. The recorded signal therefore contains a wavepacket that is followed by a coherent noise tail. This waveform is then superposed onto itself with scaled amplitude and an arbitrary time-shift applied. This simulates the

behaviour of a surface and backwall echo reflection that would be expected as a result of thickness measurement. Since the time shift can be controlled, the effective underlying synthetic thickness of the sample can be precisely set and compared to thickness values estimated by signal processing.

This model was set up to scale the backwall echo wavepacket to 150% of the surface wavepacket amplitude. Time shifts were applied to represent a synthetic thickness range of $4 - 12$ mm by assuming a propagation velocity of 3250 m/s. An example waveform is shown in Figure 4.1.b. Waveforms were generated starting with the largest timeshift equivalent to a synthetic thickness of 12 mm. Following this, 200 more waveforms were generated simulating a synthetic thickness loss of approximately 37 µm per step. Once waveforms were simulated, XC was applied to calculate arrival times, following which thicknesses were estimated.

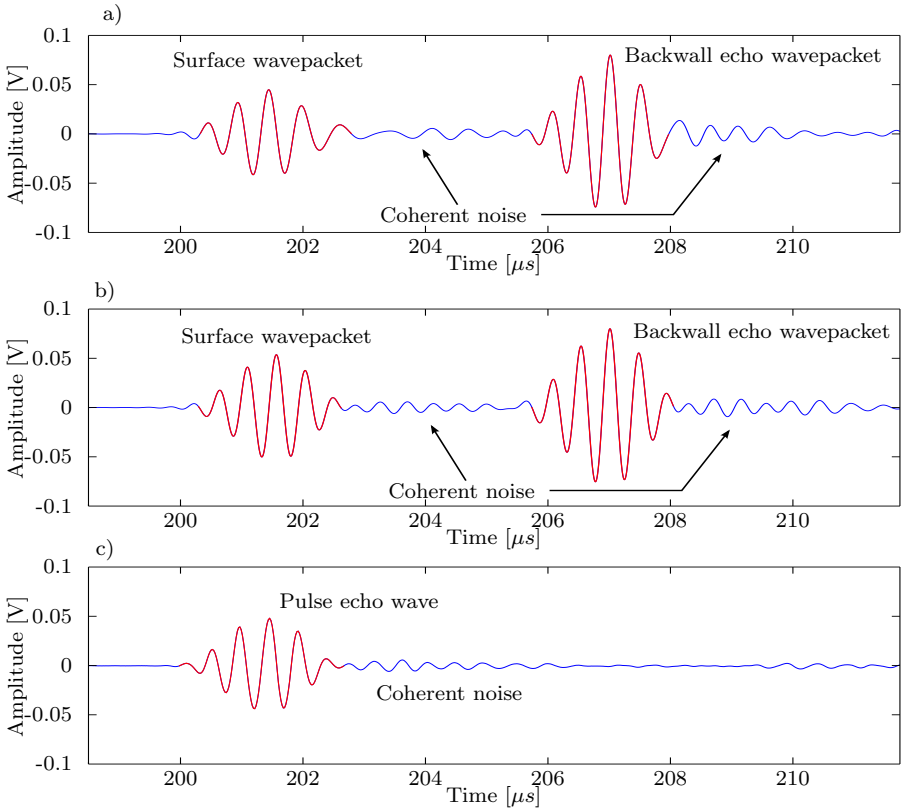

Figure 4.1: a) shows a waveform recorded with the waveguide sensor setup in pitch-catch mode. b) shows a waveform synthesised by superimposing two copies of a pulse-echo waveform shown in c). Therefore the surface and backwall echo wavepackets of b) are identical but horizontally offset and vertically (amplitude) scaled. On all three figures coherent noise is shown in blue.

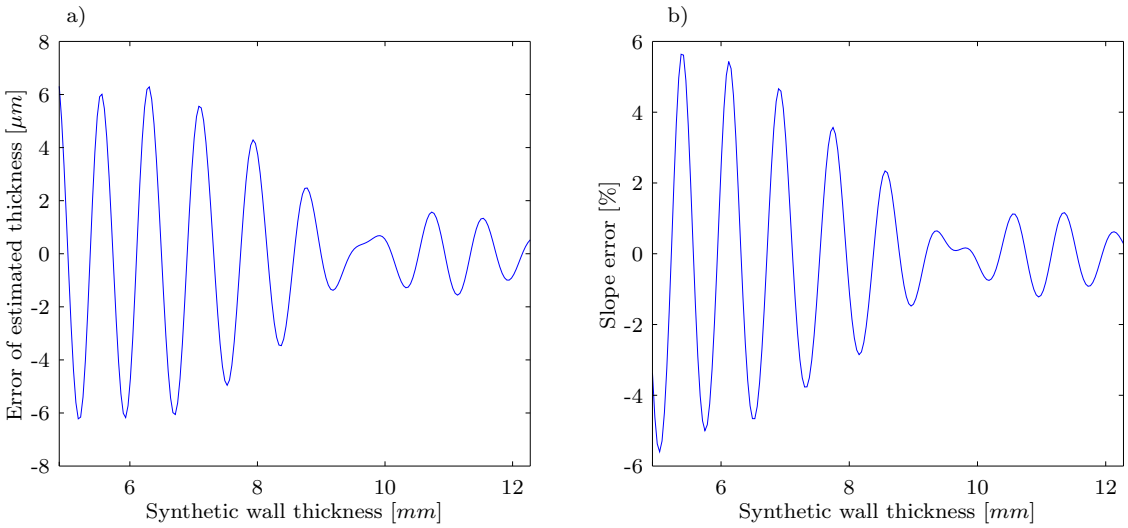

Figure 4.2: a) shows the absolute thickness error of estimates as a function of synthetic thickness. b) shows the normalised wall thickness loss rate error as a function of synthetic thickness.

Comparing the synthetic thicknesses to the estimated thicknesses, the maximum disagreement across the whole simulated thickness range was 6 µm as shown in Figure 4.2.a. This error is very small, and it is expected that other sources of variability are more limiting to absolute thickness accuracy. Therefore in this thesis absolute thickness error caused by coherent noise is assumed to be negligible.

Corrosion rate is often also desired and so the estimation of slope error is also important. Hence, the wall thickness loss rate error was calculated by normalising the error with the analytically calculated loss rate according to the following equation:

$$\overline{r} = \frac{r_a - r_m}{r_a} \tag{4.1}$$

where $\overline{r}$ is the normalised wall thickness loss rate error, r_a is the pre-set synthetic wall thickness loss rate of 37 µm per step and r_m is the estimated wall thickness loss rate between consecutive steps. The normalised wall thickness loss rate error is displayed in Figure 4.2.b. It can be seen from the figure that up to 6% error is expected. This error however is expected to apply only in the worst case for small amounts of wall thickness loss (< 0.3 mm) as can be seen on the figure.

The SNR of the waveguide selected for this investigation is assumed to be relatively poor, and so it is expected therefore that this error estimate is the worst case scenario. It should also be noted here that even though this result is specific to the

measurement system relying on the waveguide transducers, it is thought that such a simple protocol can be applied to any system affected by coherent noise in order to evaluate its effects.

4.3 Changes in coupling geometry

4.3.1 Problem statement

Long term stability of measurements is critical for permanently installed sensors. A typical issue over long periods of time is the stability of the transducer coupling. Dry-coupling is expected to be more stable compared to the more common bonded coupling. Over the course of multiple years however, dry coupling may still be subject to small changes. Such changes are expected to be a long term result of temperature variations, both as seasons change and as the operating temperatures of pipes vary. This is because differential thermal expansion of various materials (*i.e.* studs welded to the pipe, coupling clamp and the waveguides) in the sensor coupling assembly may alter coupling pressure.

Changes in the ultrasonic signal are therefore expected over time. First, simulations were carried out to see how subtle changes to coupling may affect the ultrasonic signal. Then the results of simulations were compared to experimental measurements on a compression testing machine.

4.3.2 Simulations

Coupling stability issues associated with differential thermal expansion are expected to affect most dry-coupled sensors. Although the concept is generic, presented quantitative results are specific to the waveguide sensor that was chosen as an example geometry. In order to clarify how the waveguide sensor is coupled onto samples, the cross-sectional geometry of the sensor is shown in Figure 4.3.b. For additional context, Figure 4.3.a. shows an isometric view of the relatively complex coupling assembly. Two studs are welded on the specimen, onto which the coupling

assembly of the sensor is placed. By tightening nuts on the welded studs, the coupling pressure of the sensors can be adjusted.

As shown in Figure 4.3.b., when the sensor is coupled, contact between transducers and sample is made via an approximately 0.5 mm by 12 mm contact patch. It is expected that increasing coupling pressure caused by differential thermal expansion will cause the tip of the transducers to deform. As a result, the effective contact patch width of 0.5 mm is expected to grow wider. It is not expected to exceed 1 mm, the width of the transducer itself. The 12 mm dimension is expected to change by approximately the same amount, resulting in 12.5 mm long contact patch. However, this is expected to have far less significant effect on the beam spread when compared to the change in the width of the transducer from 0.5 mm up to 1 mm and hence its effect is ignored.

In order to evaluate how contact patch changes influence the ultrasonic signals, DPSM simulations were carried out on a 10 mm thick sample block. It was assumed that the separation of the waveguides remains constant and that parameter d_f (shown

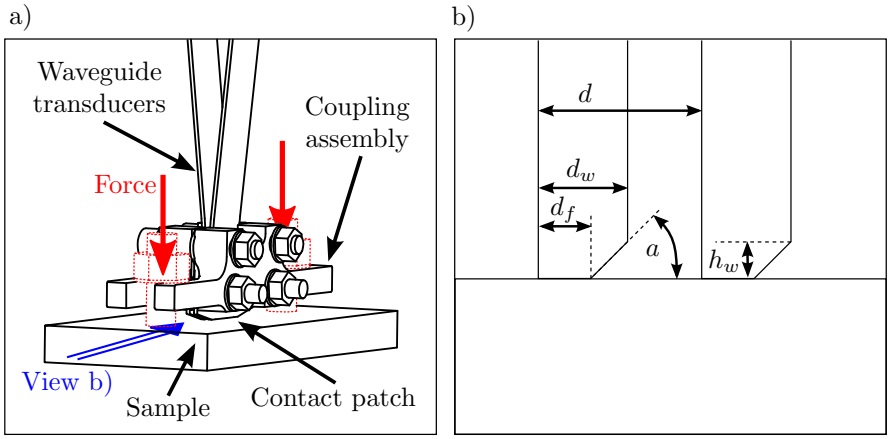

Figure 4.3: Figure a) shows the coupling assembly of the waveguide sensor highlighting that studs (shown in red) are used to force the sensor onto the sample. Figure b) shows the cross-section of the two waveguide transducers from the angle shown in a). The separation between the transducers is $d = 2$ mm, the width of a single transducer is $d_w = 1$ mm, the width of the horizontal contact interface of the waveguide is d_f, the angle of the chamfer is $a = 11^o$ and the height of the chamfer is $h_w \approx 0.1$ mm. Initially, d_f is 0.5 mm for an undeformed waveguide transducer. However, as the transducer tip is coupled in a stress state near yield, small variations in coupling forces can result in plastic deformation. As a result, the contact patch may potentially grow as large as $d_f = 1$ mm.

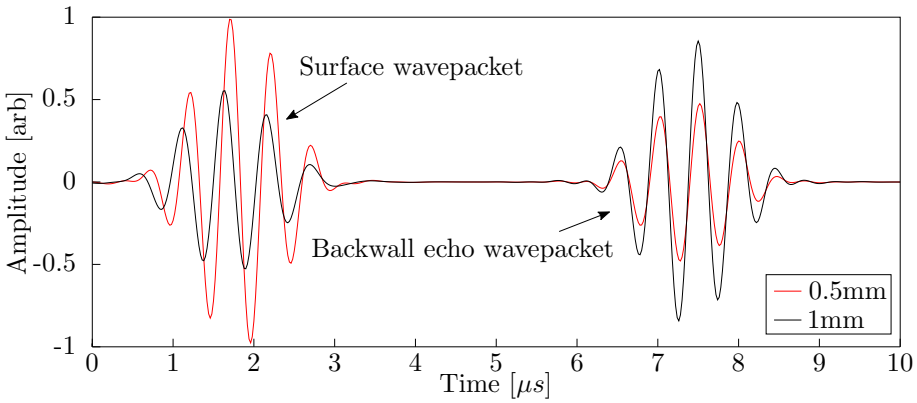

Figure 4.4: The red line is a simulated waveform for a sensor where both waveguides are coupled along a 0.5mm wide contact patch. The black line is a simulated waveform for a contact patch width of 1mm. In both cases a 2 MHz 5-cycle toneburst as was used as excitation

in Figure 4.3.b.) varies from 0.5 mm to 1.0 mm. Example simulated waveforms are shown in Figure 4.4. It can be seen from the figure that as the contact patch widens the amplitude of the backwall echo wavepacket increases. The amplitude of the surface wavepacket decreases however. This is because as the contact patch of the transducer grows to 1 mm, its size becomes comparable to the 1.6 mm wavelength of the 2 MHz burst excited in the specimen. Hence with a wider contact patch, the wave that is excited will be more collimated and so less energy will propagate horizontally. Once the waveforms were simulated, they were filtered and arrival times were extracted using XC. The arrival times of the surface and backwall echo wavepackets were then used to estimate the thickness of the simulated sample. The resulting estimated thicknesses are shown in Figure 4.5 as a function of simulated contact patch width. It is apparent from the figure that up to 0.1 mm thickness error may be introduced by changing the width of the contact patch.

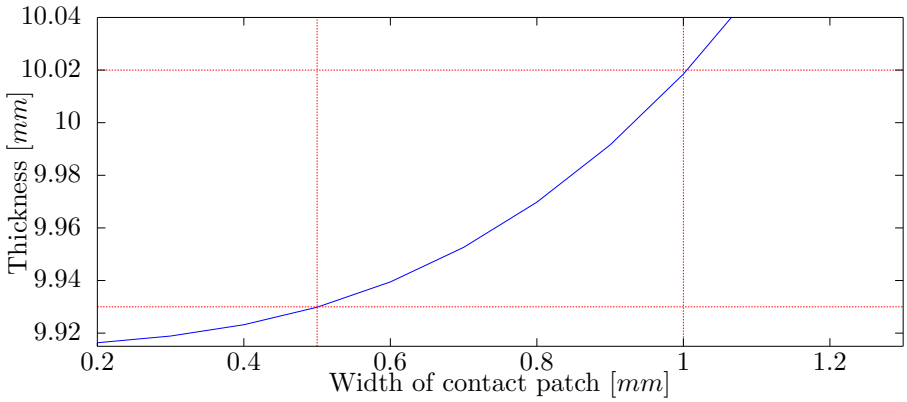

Figure 4.5: Plot shows estimated thicknesses for various contact patch widths based on arrival time extraction with XC from simulated ultrasonic signals with a 2 MHz 5-cycle toneburst as excitation using Equation 4.2 to calculate the thickness and an ultrasonic velocity of 3250 m/s (as used in the DPSM simulation).

4.3.3 Experimental verification

The results obtained via simulations of various contact patch sizes indicate that the accuracy of estimated thicknesses may vary by as much as 0.1 mm depending on contact patch size. This result was achieved by evaluating the full range of geometrically feasible contact patch sizes. The aim of this section is to experimentally verify that the assumed range of contact patch sizes is realistic. In order to do this, a forced deformation measurement was set up using an Instron compression testing machine shown in Figure 4.6. The experimental data presented here was jointly measured and evaluated by Balint Herdovics and I.

The Instron machine was used to apply compressive load onto the sensor assembly and to measure the displacement of the attachment assembly while applying that load. Figure 4.7.a. shows the extension-load plots of 5 loading cycles applied with 3kN, 4kN, 5kN, 6kN and 7kN maximum compressive load. Each of these load cycles were repeated 5 times. These specific load values were chosen as they are representative of what is expected during sensor installation. It is apparent from the figures, that as maximum load increases, the remnant compressive extension at zero load increases as well, which indicates plastic deformation of the waveguide sensor. At 7kN compressive load, the vertical plastic deformation of the system is approximately 0.3 mm. The majority of this plastic deformation is assumed to be at the contact tip of the waveguide sensor.

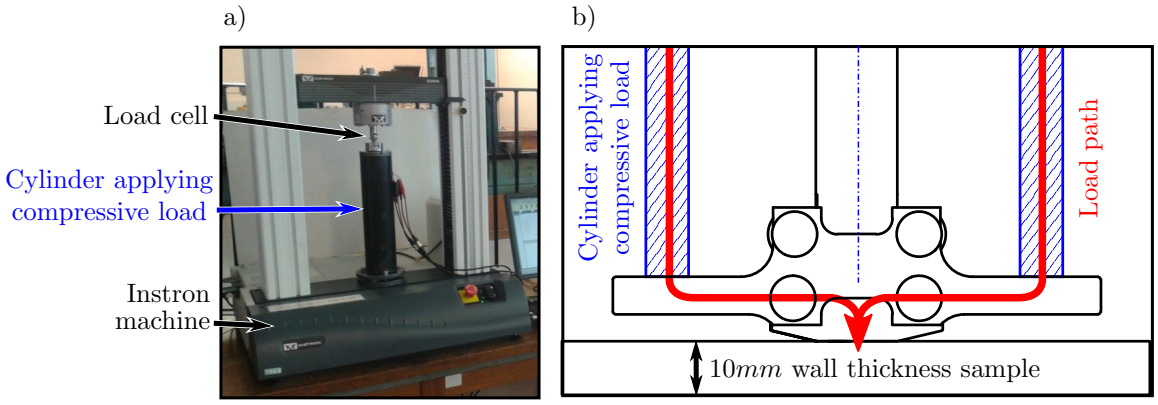

Figure 4.6: a) shows the Instron machine setup. Here, the waveguide sensor is inside a cylinder that is used to apply compressive load. b) shows how this load is applied and how the waveguide sensor is positioned inside the cylinder. Here red arrows are used to emphasise how compressive load is applied. In this setup both compressive load and compressive extension are measured at the load cell shown in a).

During the measurement, ultrasonic signals were also recorded continuously. The amplitude of the measured signals are shown in Figure 4.7.b. It is observed that at a given compressive load, signal amplitude is highest if the sensor had been previously exposed to even higher loads. The plastic deformation and the continuously increasing signal amplitude suggest that the contact patch size does increase as compressive coupling load is applied. In addition, it is also noted that increasing load above 6kN does still introduce further plastic deformation, but it does not further increase signal amplitude. It is therefore inferred that the maximum contact patch width of 1

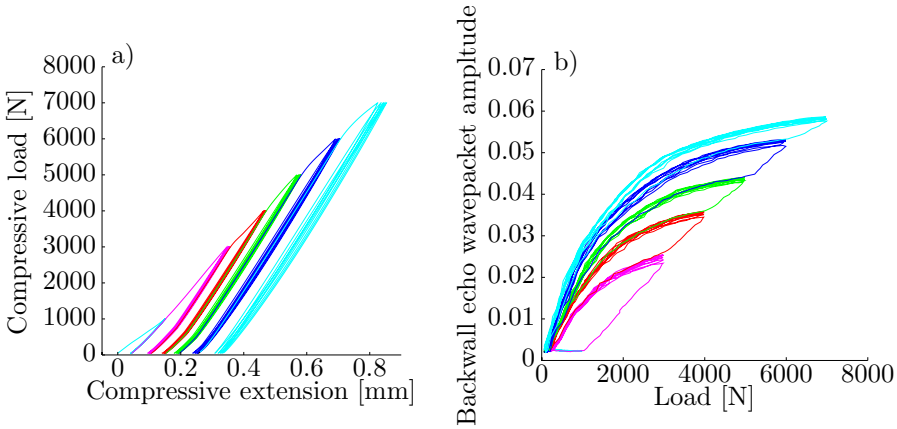

Figure 4.7: a) shows the compressive load-extension graph for the waveguide sensor. b) shows the amplitude of the backwall echo amplitude of the received signals. Compression cycles to different maximum loads are shown by different colours. Magenta shows cycles with a max. load of 3 kN, red with 4 kN, green with 5 kN, blue with 6 kN and cyan with 7 kN max. load. 5 cycles are shown for each of the 5 maximum load values and so 25 compression cycles are shown in total.

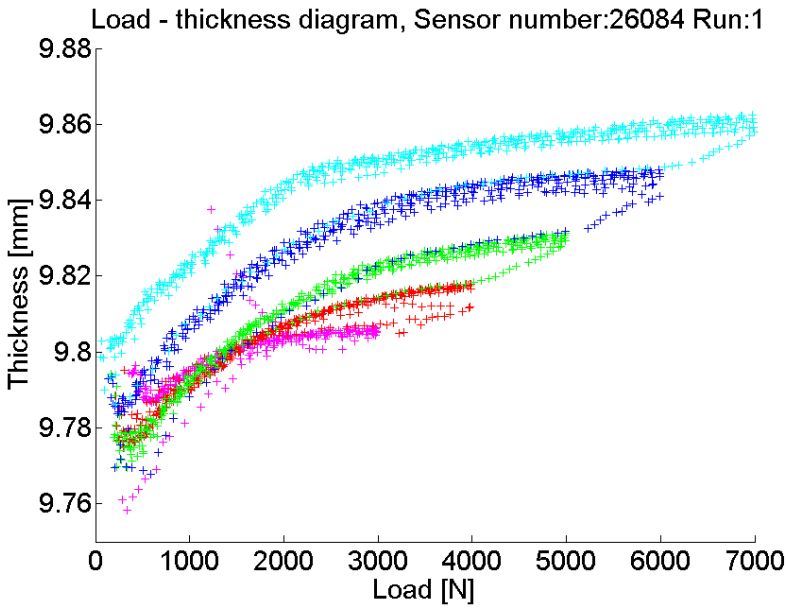

Figure 4.8: Wall thickness estimates using XC (with a 2 MHz 5-cycle toneburst) for the waveguide sensor during the compression testing. Colours shown here correspond to those in Figure 4.7.a. and b.

mm is reached at approximately 6kN compressive load.

In order to quantitatively compare these findings with the simulated data, the thicknesses were estimated based on the experimentally measured waveforms. The estimated thicknesses are plotted against compressive load in Figure 4.8. It can be seen from the figure that the overall range of thicknesses is approximately 0.1 mm (between 9.76 mm and 9.86 mm), which is in agreement with the simulated results. It is therefore concluded that the initial hypothesis that the contact patch may vary as a function of compressive load is correct. Furthermore it can be seen that by coupling the sensor to a compressive load of 7kN at first attachment and then loosening it to 5kN may result in the most stable thickness estimates. This means that ± 2 kN load variations may result in minimal thickness variations (of the order of $\sim$ 10 micrometers).

4.4 Effects of temperature

4.4.1 Calibration measurements

It is well known that ultrasonic propagation velocity varies as a function of temperature [25, 56]. Temperature variations of just 20 °C are expected to cause ultrasonic propagation velocity changes of the order of 0.5%. Similar temperature variations in some cases may occur over short periods of time, caused by process condition changes or even daily temperature variations. If uncompensated, such temperature changes are expected to skew both short and long term corrosion rate estimates. In order to minimise the effect of temperature on ultrasonic measurements, temperature compensation is investigated in this section.

Since ultrasonic propagation velocity changes are being considered, it should be noted that ultrasonic propagation velocity is also a function of material constants, as explained in Chapter 2. It is therefore expected that the ultrasonic propagation velocity-temperature curve will differ for various materials. Accurate calibration curves however are not well reported in the literature. In this thesis a selection of steel alloys were evaluated in order to assess the extent to which variability can be expected. Altogether 6 steel alloys were selected for this purpose. Their composition is summarised in Table 4.1.

A sample of each of these 6 alloys was selected and a waveguide sensor was coupled onto each of them. A K-type thermocouple was then spot welded onto each of the samples 10 mm from the contact patch of the ultrasonic sensor. The quoted accuracy

Grade	**C [%] (max)**	**Mn [%]**	**P [%] (max)**	**S [%] (max)**	**Si [%] (max)**	**Ni [%]**	**Cr [%]**	**Mo [%]**	**Thickness [mm]**
S275	0.25	1.6	0.05	0.05	0.05	-	-	-	9.98 ± 0.005
304	0.08	2	0.04	0.03	1	8-11	18-20	-	9.84 ± 0.005
316	0.08	2	0.04	0.03	0.75	14	16-18	3	9.65 ± 0.005
Cr 12	0.04-0.17	0.40-0.65	0.04	0.04	0.15-0.40	-	0.80-1.15	0.45-0.60	9.67 ± 0.005
Cr 5	0.15	0.30-0.60	0.04	0.03	0.5	-	4.00-6.00	0.45-0.65	10.17 ± 0.005
Cr 9	0.15	0.30-3.60	0.03	0.3	1	-	8.00-10.0	0.90-1.10	9.59 ± 0.005

Table 4.1: Composition of steel alloys selected for temperature compensation calibration. Thicknesses of the samples were measured using a micrometer (0.01mm precision).

of the thermocouples was 1 °C, whereas the standard deviation of their temperature readings was measured to be ~ 0.05 °C. This is equivalent to a thickness estimate standard deviation of 100 nm for a 10 mm thick component. The samples were then placed into a furnace (Model: Elite BSF12/27, Max. Temp.: 1200 °C, Max. Power: 5 kW) where they were slowly heated from room temperature to 450 °C with a heating rate of 1 °C per minute. This slow heating rate was chosen to allow the samples more time to reach a uniform temperature distribution throughout the sample, resulting in more accurate temperature measurements. In order to avoid the transient coupling effect of the transducers explained in Section 4.3, this heating cycle was repeated 3 times for all samples with the intention that only the 3$^{\text{rd}}$ cycle is to be used for calibration measurements.

During the heating cycles, ultrasonic measurements were also carried out. The arrival times for the measured waveforms were estimated using XC. Thermal expansion is ignored here, and so the thickness of the samples is assumed to be constant (see below), therefore the previously introduced thickness equation can be inverted to estimate propagation velocity at all temperatures using the arrival times from the measured waveforms.

$$T_{2p} = \frac{1}{2}\sqrt{c\,(t_1 - t_2)\,(-2d - c \cdot t_2 + c \cdot t_1)} \tag{4.2}$$

$$c = \frac{d - \sqrt{d^2 + 4T_{2p}^2}}{t_1 - t_2} \tag{4.3}$$

where T_{2p} is the thickness calculated using the arrival times of the surface and backwall echo wavepackets, c is the propagation velocity of the ultrasonic wave, t_1 is the arrival time of the surface wavepacket, t_2 is the arrival time of the backwall echo wavepacket and d is the separation between the transducers. Equation 4.2 is the previously introduced equation for estimating thickness. Equation 4.3 is the result of inverting Equation 4.2 for calculating ultrasonic propagation velocity based on the arrival times and the thickness.

Note, that this inversion assumes that the thickness is constant, and so ignores thermal expansion of the sample that causes the thickness to change with temperature. This also implies, that once the velocities are calculated and are used for temperature compensation, the calculated thicknesses will not change as a function of temperature.

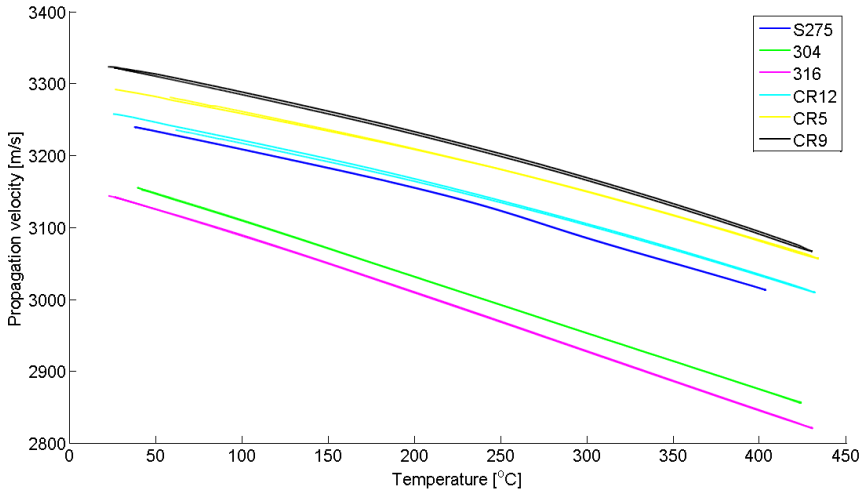

Figure 4.9: Temperature calibration curve for S275 (blue line), 304 (green line), 316 (magenta line), CR 12 (cyan line), CR 5 (yellow line) and CR 9 (black line) alloys. The curves are shown for all samples for the 3rd heating cycle. The curves are shown both for heating up and cooling down.

This formulation is preferred, since the thickness change caused by thermal expansion is only temporary, and does not cause any permanent wall thickness change, whereas it is only permanent wall thickness loss that is of interest in this thesis.

Based on this equation the ultrasonic propagation velocity can be estimated and plotted against measured temperature. Figure 4.9 shows results of the 3rd heating cycle for all samples, including heating up and cooling down. As shown on the figure, the hysteresis between heating up and cooling down is small - less than $\sim 0.2\%$ for all samples. It is therefore assumed that coupling changes do not significantly influence these measurements and the coupling is stable. This also indicates that the heating was slow enough to avoid any significant temperature hysteresis. It is also apparent from the results that over the temperature range of approximately 400 °C a velocity drop of close to 10% is observed for all investigated materials. This qualitatively agrees with previously reported values [25, 56]. Therefore these measurements are expected to be accurate.

As outlined above, one of the aims of this section is to establish the range of variability between calibration curves of various alloys. As can be seen from Figure 4.9, differences in some cases are significant. The largest offset between curves (CR9 and 316) was found to be of the order of 10%. It is concluded here that using the

appropriate calibration curve is therefore critical.

Since the full calibration data is available for this thesis, these calibration curves are used directly in order to maximise accuracy. It is not practical however to report the large number of measurements as a reference. Instead, the calibration curves are approximated by means of polynomial fits, so that they can be concisely summarised by only a few variables. Typically ultrasonic propagation velocity-temperature calibration curves are approximated by linear fits [25]. Since the measurements reported here are more repeatable than what is typically available in the literature, quadratic fits have also been applied to the measured curves. The overview of linear fits is shown in Table A.1 whereas the overview of quadratic fits is shown in Table A.2 in the Appendix. These tables describe both the parameters of the fits and the maximum error that is caused when using the fit.

In summary, linear fits may result in estimated ultrasonic propagation velocity errors as large as 12 m/s ($\sim 0.4\%$) whereas the maximum error introduced by the quadratic fit is 3.75 m/s ($\sim 0.1\%$) over the whole temperature range (20 °C to 400 °C). It is therefore concluded that quadratic fits provide more accurate fits and are recommended instead of the the standard linear fit.

4.4.2 Temperature gradients

As described in the previous section, temperature compensation is critical for accurate wall thickness and wall thickness loss rate estimates. In order to successfully implement temperature compensation, temperature calibration measurements were first carried out. These measurements were carried out in a furnace, where heating was chosen to be slow and uniform. This allowed for accurate temperature readings, which could then be linked to changes in ultrasonic propagation velocity. In field applications however, where temperature readings are used for the inverse problem, the temperature measurements typically have to be performed in less controlled conditions.

A typical limitation in field conditions is non-uniform heating. An example of this can be pipes of petrochemical plants that are ultrasonically monitored. Pipe temperatures

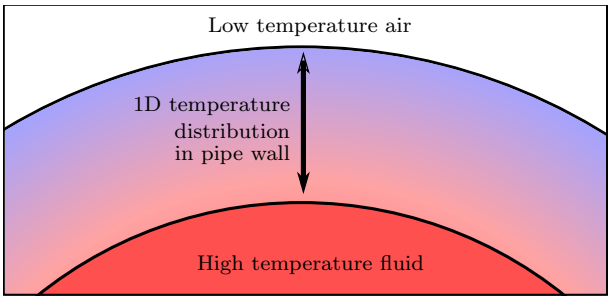

Figure 4.10: Figure shows high temperature fluid and low temperature air surrounding the pipe wall, which result in a non-uniform temperature distribution within the pipe wall.

have to be monitored in order to apply accurate temperature compensation. Such pipes often carry high temperature fluids. Because of this, a temperature gradient can exist within the pipe wall, where the inside surface of the pipe is higher temperature compared to the outside of the pipe, commonly surrounded by air. Since it is only the outside of the pipe that is accessible for temperature measurements, the temperature gradient within the pipe wall is difficult to estimate. This phenomenon is expected to affect pipes, pressure vessels or other containers where the temperatures within said containers are different from the ambient temperature. It is not clear however, how large an error is introduced if this gradient effect is ignored and the temperature compensation is implemented by assuming that the outside surface temperature is accurate.

In order to investigate this, a 1D transient heat propagation simulation was used to study the phenomenon, a sketch of which is shown in Figure 4.10. This simulation models the system by assuming that heat is transferred between the fluid and the inner pipe wall surface via convection and heat is transferred within the pipe wall via conduction. The interaction between the outer pipe surface and air is modelled as heat convection. It is assumed in the simulation that initially the system is in equilibrium and all points of the system (fluid, pipe and air) are at a uniform 20 °C temperature. Following this, the fluid is heated up linearly to a higher temperature which is then kept constant until the end of the simulation. The temperature of air is kept constant throughout the simulation. An example of such a transient temperature evolution is shown in Figure 4.11.a. The variables therefore that describe this transient temperature evolution are the heating rate Q and maximum temperature difference ($\Delta\Theta$). Heating rates from $Q = 6 - 2000$

°C/min were investigated. For $\Delta\Theta$, values from 10 °C to 380 °C are evaluated.

In addition to the predefined temperature changes, the remaining variables are defined here. The only geometric parameter of the system is pipe thickness T, for this values of 5 mm,10 mm and 20 mm are simulated. In order to describe the heat conduction within the pipe, the heat transfer coefficient of the pipe material is assumed to be $k = 50\frac{\mathrm{W}}{\mathrm{m{\cdot}K}}$ [57–59] and its heat diffusivity is assumed to be $\alpha = 1.4 \cdot 10^{-5}$ m/s [59]. These are thought to represent the heat transfer parameters of carbon steel [57–59]. Parameters describing convection are subject to more variability. Conditions, such as flow rates and fluid turbulence within the pipe may influence the rate of heat convection from fluid to pipe. Similarly, insulation on the outside of the pipe or wind conditions may influence the rate of convection on the outside surface of the pipe. Hence, for heat convection coefficients the following ranges of values were investigated: $h_a = 1 - 20\frac{\mathrm{W}}{\mathrm{m^2K}}, h_w = 50 - 1000\frac{\mathrm{W}}{\mathrm{m^2K}}$ where h_a is the heat convection coefficient between the pipe and air, and h_w is the heat convection coefficient between the fluid and the pipe. The simulation was set up using the defined parameters was carried out as described by Simonson *et al.* [60].

The results of an example simulation are shown in Figure 4.11.a. and b. The

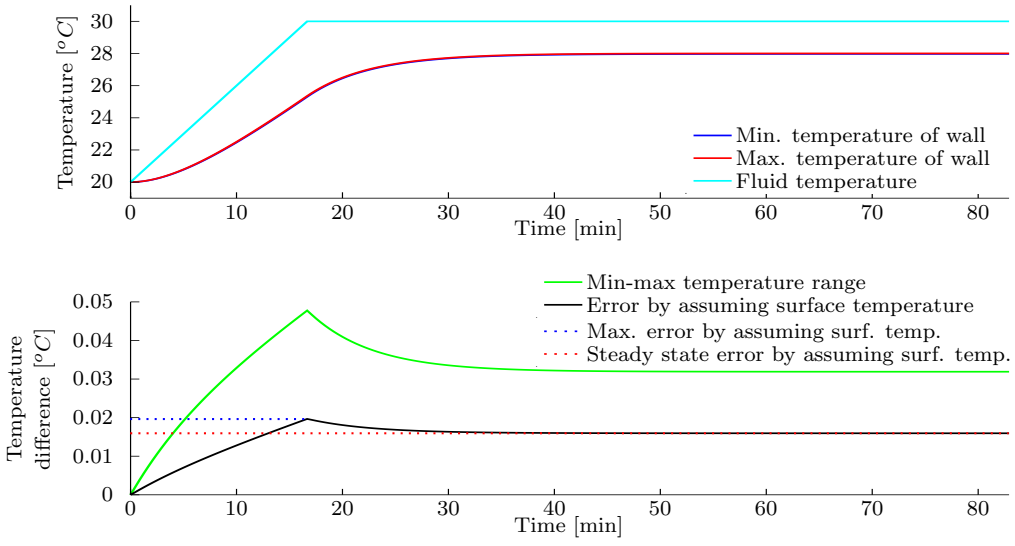

Figure 4.11: Top graph shows the temperature evolution of a simulated $T = 10$ mm thick sample. Variables for this simulation were: $h_a = 20, h_w = 80, \Delta\Theta = 10$ °C and heating rate = 6 °C/min. Bottom graph shows maximum error by assuming surface temperature (METEST) as well as the steady state error by assuming surface temperature (SETEST).

most interesting metric on these plots is the effective temperature error by assuming surface temperature (ETEST) shown as a black line. ETEST quantifies the difference between the outside surface temperature of the simulated pipe and the effective temperature averaged along the ultrasonic wavepath. Because of this, ETEST is the source of error in temperature compensation at any given time in the simulation. The most notable features of the ETEST plot are the maximum transient error (METEST) and the steady state error (SETEST). Instead of showing the full transient plots for all parameter combinations, only METEST and SETEST are used to describe the error introduced by the 1D heat gradient.

Steady state effective temperature error by assuming surface temperature (SETEST)

Firstly, the steady state error (SETEST) is considered here. Since steady state error (SETEST) is not a function of the heating rate, the only parameters of the heat propagation model it is expected to depend on are T, $\Delta\Theta$, h_a and h_w. Therefore simulations have been carried out with all predefined parameter values for these 4 variables. Before the data is presented however, some simplifications are made here to present this 4 dimensional dataset concisely.

It is noted here that the steady state error (SETEST) is directly proportional to $\Delta\Theta$ for all simulated parameter sets. In other words, if $\Delta\Theta$ is doubled, the steady state error (SETEST) will double regardless of any other parameter value. The error introduced in steady state error (SETEST) by this linear fit is negligible compared to the simplification of the simulation itself and is of the order of 0.05%. It is therefore sufficient to plot steady state error (SETEST) results for one particular $\Delta\Theta$ value, since the interested reader can easily calculate other relevant steady state error (SETEST) values.

In addition to $\Delta\Theta$, the steady state error (SETEST) is close to proportional to the thickness for all simulated parameter sets as well. Similarly to $\Delta\Theta$, if the thickness is doubled, the steady state error (SETEST) will double as well regardless of any other parameter value. Here, the linear fit is less good and may introduce up to 39% error in estimated steady state error (SETEST) values.

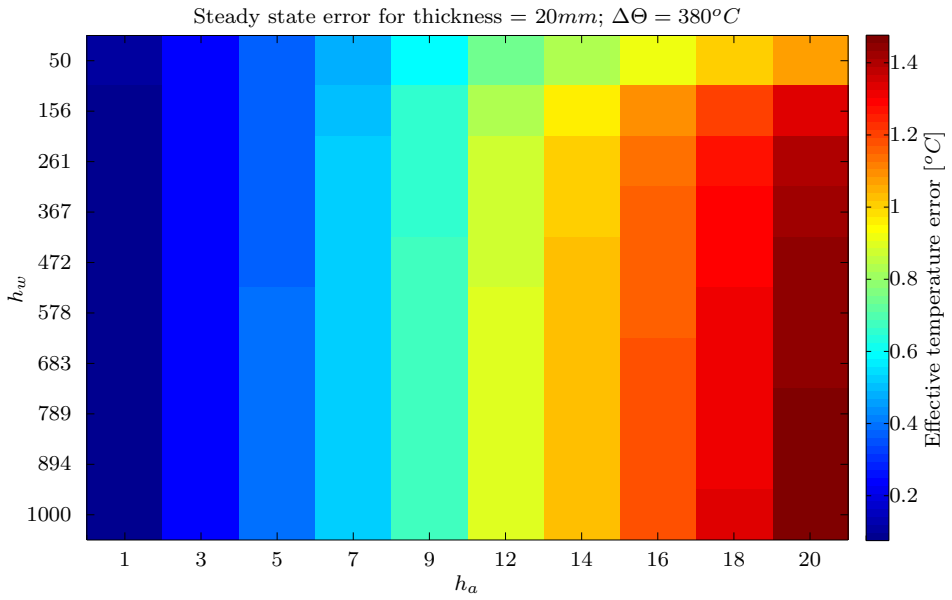

Figure 4.12: Estimated steady state error (SETEST) values in degrees C for a 20 mm thick pipe. The maximum temperature difference in the simulation was $\Delta\Theta = 380$ °C. Results can be scaled for other thicknesses and $\Delta\Theta$ values as described in text.

For h_a and h_w variables no such simplifications are made. Hence, the results of estimated steady state error (SETEST) values are plotted in Figure 4.12 as a function of both h_a and h_w. The plot shows that with $\Delta\Theta = 380$ °C and $T = 20$ mm, the maximum plausible steady state error is approximately 1.4 °C. Errors for other T and $\Delta\Theta$ values can be approximated linearly by $SETEST(h_a, h_w) \cdot \frac{T}{20\text{ mm}} \cdot \frac{\Delta\Theta}{380^o\text{C}}$ where $SETEST(h_a, h_w)$ is the relevant error value directly from Figure 4.12. Based on the ultrasonic propagation velocity-temperature calibration curve established in the previous section this results in about 0.025% propagation velocity error. This is also equivalent to a thickness error of 5 µm for a 20 mm thick pipe for $\Delta\Theta = 380$ °C.

Maximum transient effective temperature error by assuming surface temperature (METEST)

In addition to the steady state error (SETEST), the maximum transient error (METEST) is also evaluated here. METEST is expected to be a function of the already established 4 variables $T, \Delta\Theta, h_a$ and h_w as well as the heating rate Q. Since there are 5 parameters that influence the maximum transient error (METEST), it is even more difficult to concisely present an overview of the simulated dataset. It is

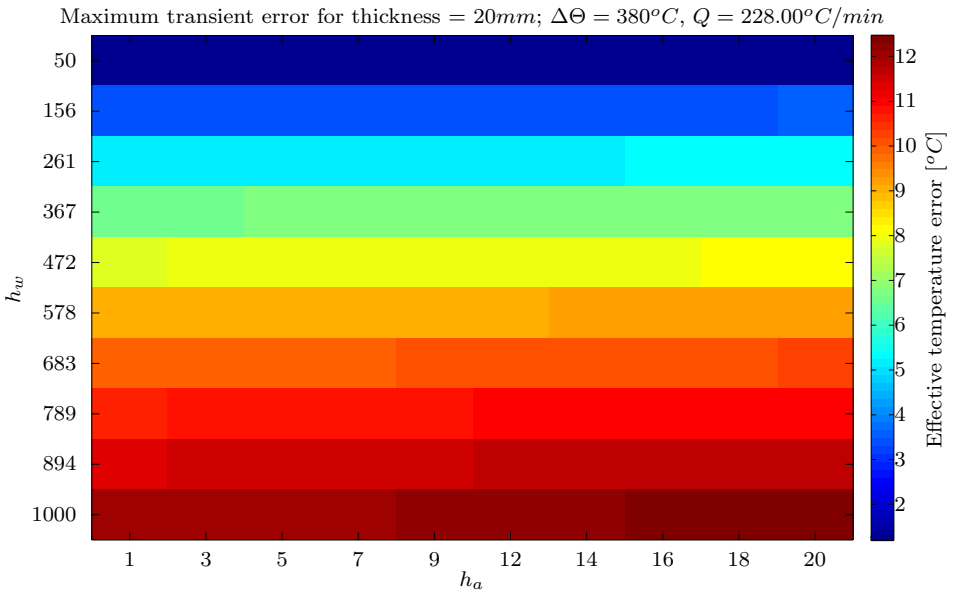

Figure 4.13: Estimated maximum transient error (METEST) values for a 20 mm thick pipe. The maximum temperature difference in the simulation was $\Delta\Theta = 380$ °C. The heating rate was 228 °C/min

expected that the effect of T and $\Delta\Theta$ on the maximum transient error (METEST) are both close to linear, and so the maximum transient error (METEST) is plotted only against the remaining 3 parameters. Results are therefore shown on three separate figures: Figure 4.13 in this section, whereas Figures A.1 and A.2, are found in the Appendices.

In order to approximate the behaviour of T and $\Delta\Theta$, their effect is estimated by linear fits the following way:

$$METEST(h_a, h_w, Q, T, \Delta\Theta) = METEST(h_a, h_w, Q, 20mm, 380^{\circ}\mathrm{C}) \cdot \cdot \frac{\Delta\Theta}{380^{\circ}\mathrm{C}} \cdot (a_{t1} \cdot T + a_{t0}) \qquad (4.4)$$

where $METEST(h_a, h_w, Q, T, \Delta\Theta)$ is the maximum transient error value being estimated, $METEST(h_a, h_w, Q, 20mm, 380^{\circ}\mathrm{C})$ are values from Figures 4.13, A.1 and A.2, whereas a_{t1} and a_{t0} are parameters of a linear fit. With values $a_{t1} = 5.55 \cdot 10^{-2}$ and $a_{t0} = -1.091 \cdot 10^{-1}$, the maximum transient error value can be estimated to an accuracy of 92%. This means that maximum transient error (METEST) values estimated via Equation 4.4 may be up to twice as large or half of the real values.

It can be seen from Figure 4.13 that transient errors of the order of 10 °C may feasibly occur if assuming that temperature measured on the outside surface of a pipe is accurate to compensate ultrasonic thickness with. Based on the ultrasonic propagation velocity-temperature calibration curve established in the previous section this results in about 0.2% propagation velocity error. This is also equivalent to a thickness error of 40 µm for a 20 mm thick pipe.

4.5 Summary

This chapter has discussed and evaluated common experimental error sources in ultrasonic wall thickness measurements. Measurement uncertainties associated with coherent noise, coupling variability and temperature effects have been investigated. The introductions and descriptions of these error sources were kept general, in order to be applicable for a range of ultrasonic applications regardless of hardware choice. Quantitative results were presented for a specific sample application, the waveguide sensor that is used throughout this thesis.

It was found that coherent noise pattern specific to the waveguide transducer does not significantly limit the absolute accuracy of ultrasonic thickness estimates. The absolute wall thickness error caused by coherent noise was shown to be less than 6 µm using a waveguide transducer with a signal to noise ratio of 16 dB. This is considered to be the worst case scenario, as 30 dB is thought to be usually achievable using waveguides. It was also found that wall thickness loss rate estimates may be skewed by up to 6% as a consequence of coherent noise using the same 16 dB SNR transducer. This was accepted as one of the limitations of wall thickness loss rate estimation using waveguide sensors.

Coupling uncertainties were shown to introduce a wall thickness estimate variability of up to 0.1 mm. This variability however would self regulate after temperature cycling during normal operation of the inspected component. Alternatively, coupling to a load of 7 kN and then reducing load to 5 kN the sensor while it is being attached would also stabilise coupling and would eliminate associated variability.

The effects of temperature on ultrasonic wave propagation velocity have also been eval-

uated. It was determined based on previous reports that temperature compensation is necessary, as even small temperature variations ($\sim$ 10 °C) can introduce significant errors in wall thickness and wall thickness loss rate estimates. For reference, $\sim$ 10 °C temperature error would introduce a thickness error of approximately 20 µm on a 10 mm thick sample. Because of this, first the variability of temperature measurements was estimated. It was found that with a K-type thermocouple temperature of the sample can be measured with a standard deviation of $\sim$ 0.05 °C, which is equivalent to a thickness estimate variability of 100 nm for a 10 mm pipe. This error is relatively large compared to the error due to random noise and signal processing techniques alone. It is therefore concluded that the limiting factor of wall thickness estimate repeatability is the error introduced by temperature compensation.

Furthermore, it was found that temperature measurements may in some cases be limited in accuracy because of non-uniform temperature distribution within the pipe wall. Pipes which carry high temperature fluids were investigated as they were thought to be a typical example of this phenomenon. This is because such pipes are exposed to different temperatures on their internal and external surfaces, and so a 1D temperature distribution exists within the pipe wall. Temperature readings are only accessible from the outside surfaces of pipes however, these are not an accurate approximation for the the effective temperature along the ultrasonic wavepath. It was found that as a result of such temperature gradients, temperature compensation errors may be as large as 10 °C during transients for a 20 mm thick pipe with $\Delta\Theta$ = 380 °C and $Q = 228^oC/min$ (equivalent to 40 µm error for a 20 mm thick component) and up to 1 °C in steady state with $\Delta\Theta$ = 380 °C (equivalent to 4 µm error for a 20 mm thick component).

Chapter 5

Ultrasonic Measurements During the Corrosion Process

5.1 Introduction

Previous chapters of this thesis have discussed techniques to maximise the precision of ultrasonic wall thickness monitoring. Although many of the possible sources of error were investigated separately, the performance of the whole permanently installed ultrasonic monitoring system has not been verified experimentally, which is therefore the motivation of this chapter. Since corrosion monitoring is one of the possible applications of ultrasonic monitoring, this section compares predicted corrosion rates in controlled laboratory corrosion experiments to ultrasonic wall thickness loss estimates.

This chapter therefore first introduces key concepts that are essential for inducing corrosion in a controlled way. As part of this, two rig designs are proposed for inducing corrosion. First, forced corrosion is evaluated, which allows for quick confirmation of ultrasonic monitoring accuracy. Secondly, an unforced corrosion rig was constructed, which was expected to result in more realistic corrosion environments and rates, however these are then more difficult to control.

Some of the material described in this chapter has been published before as conference proceedings in [P3] and [P6].

5.2 Theory of corrosion

Corrosion by definition refers to metal loss, which most commonly occurs by oxidation [61, 62]. Many papers and books have been dedicated to evaluate and describe corrosion, a small selection of which is referred to here [61–65]. Within the petrochemical industry alone there are wide range of forms that commonly occur, such as naphthenic acid corrosion [2], sulfidic corrosion [1], hydrochloric acid corrosion [1], etc. The complexity of contributing factors (*e.g.* pH, temperature, electrolyte constituents, flow rate of electrolyte) associated with corrosion is large, and it is often difficult to give accurate quantitative estimates of corrosion based on electrochemical considerations alone.

Instead of characterising various forms of corrosion, this section aims to induce corrosion as simply as possible. By minimising variables, corrosion becomes more predictable and controllable. This then allows for straightforward verification of the ultrasonic thickness measurements, by comparing them to electrochemically predicted corrosion rates.

5.2.1 Basic corrosion process

Mild steels are some of the most affordable steels [66], and therefore are frequently used for a variety of applications [66,67]. They have long been known to be susceptible to various forms of corrosion [68], but their use still remains economically viable and they are used as pipe material. This is because their degradation can be anticipated and predicted and continuously improving corrosion monitoring capabilities help extend the lifetime of such pipes. Hence, mild steel samples are used in this thesis for corrosion experiments, as it is a relevant material and corrosion can be easily induced.

The largest fraction of mild steel is iron Fe and the oxidation of Fe is the most important reaction that characterises metal loss. This oxidation reaction is described by the following equation:

$$\mathrm{Fe} \longrightarrow \mathrm{Fe}^{2+} + 2\,\mathrm{e}^{-} \tag{5.1}$$

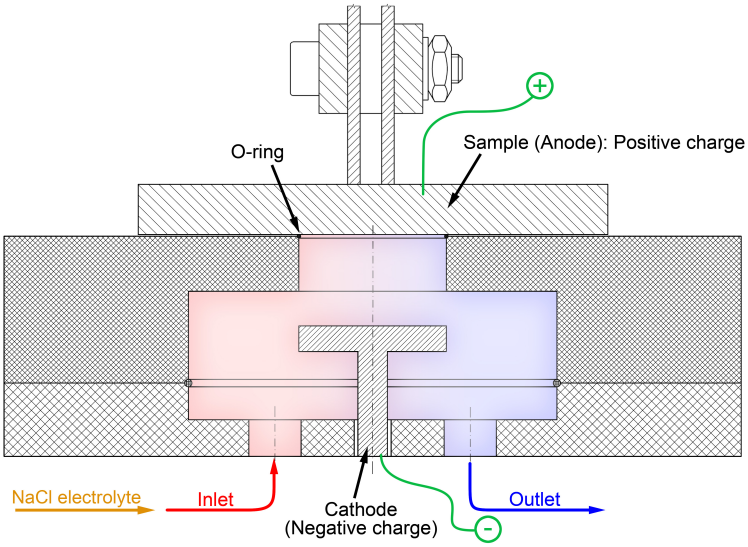

Figure 5.1: Cross-section of forced corrosion rig. Induced corrosion is proportional to the current applied between cathode and anode.

In electrochemical terms, this reaction takes place at the anode, which in this chapter is a mild steel sample that is being corroded. The most straightforward approach to force this reaction is to apply a current across an electrolyte from a counter electrode (cathode) to the sample of interest, which thereby is expected to induce corrosion. In order to experimentally verify this, a corrosion rig was built. This is shown in Figure 5.1.

The operation of the rig is depicted on a diagram shown in Figure 5.2. First a permanently installed waveguide sensor is coupled onto a mild steel sample. Using the

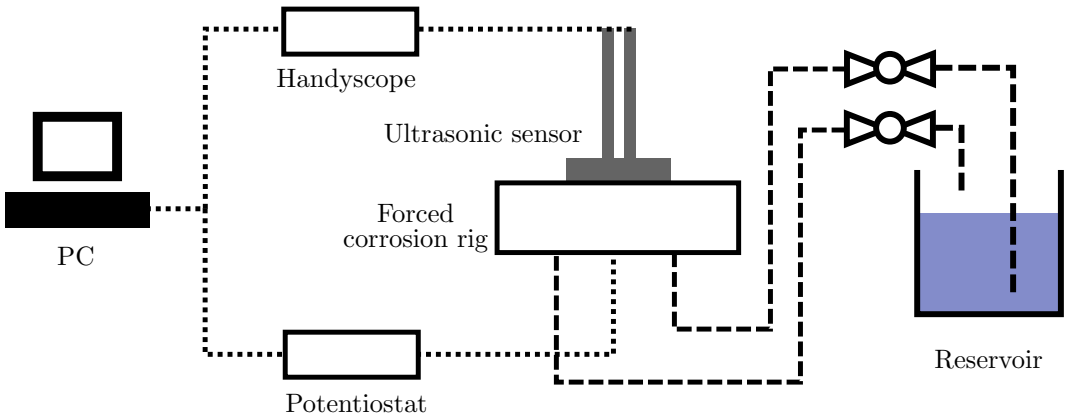

Figure 5.2: Diagram of forced corrosion rig. Dashed lines show electrolyte tubing and dotted lines show electrical connections.

signal acquisition and processing protocol described in previous chapters, ultrasonic wall thickness measurements are initiated and carried out throughout the experiment with a Handyscope HS3 (TiePie engineering, Sneek, Netherlands). A controlled area of the sample below the footprint of the ultrasonic sensor (diameter=21.3 mm, area=452 mm^2 sealed with an O-ring) is exposed to an electrolyte that is pumped through the cell. By applying a current between a cathode and the sample using an Elektro-Automatic PS 8000 DT power supply (Viersen, Germany), corrosion is forced on the exposed area of the sample. The advantage of forcing corrosion in this fashion is that induced corrosion is proportional to the current applied on the sample assuming that the corrosion is uniform across the surface. Since thickness loss is proportional to the current, it can be calculated by Faraday's law:

$$Corrosion\ Rate\left[\frac{\mathrm{m}}{\mathrm{s}}\right] = \frac{M_{Fe}I}{2FA\rho_{Fe}} \tag{5.2}$$

where M_{Fe} is the molar mass of iron, I is the forced current, F is Faraday's constant, A is the exposed area of the sample and ρ_{Fe} is the density of iron. Specifically for the setup used, this equates to $Corrosion\ Rate[\frac{\mathrm{mm}}{\mathrm{year}}] = 2570.8\ I \approx 2500\ I$.

5.2.2 Unforced corrosion

Forcing corrosion by applying current allows for accurately controllable wall thickness loss, it is therefore expected to be useful for verifying the accuracy of ultrasonic wall thickness loss measurements. In forced corrosion experiments, the induced corrosion rate will necessarily be higher than what would naturally occur because of the applied current. Hence, a second set of experiments is proposed, which relies on a corrosive electrolyte to induce corrosion. Here, a corrosive substance (*e.g.*: citric acid) is dissolved in distilled water in order to induce corrosion. The concentration of the solution is the only control mechanism this setup has, since the corrosion current depends on the degree to which the electrolyte promotes oxidation of the surface.

In these experiments the rate of corrosion is not directly controlled, an alternative method of corrosion rate prediction is hence required. Linear polarisation resistance (LPR) measurements are commonly used for estimating corrosion current [69]. This technique is based on the assumption that the polarisation resistance of the system

around its equilibrium potential is inversely proportional to the corrosion current at equilibrium [69]:

$$I_{corr} = \frac{B}{R_p} \tag{5.3}$$

$$B = \frac{\beta_a \cdot \beta_b}{2.303(\beta_a + \beta_b)} \tag{5.4}$$

where I_{corr} is the corrosion current at equilibrium, β_a and β_c are the anodic and cathodic Tafel constants, B is an intermediate constant and R_p is the polarisation resistance. β_a and β_c are expected to be constant and according to [70] B can be assumed to be $B \sim 26$. Hence, only R_p has to be monitored during corrosion measurements.

In order to measure polarisation resistance R_p, a small voltage has to be applied to the sample (referred to as the working electrode) compared to its equilibrium potential. This applied voltage is referred to as the overpotential. Since the applied overpotential is small, only small forced currents are expected, which do not significantly contribute to the corrosion process. It is therefore possible to approximate the corrosion current at equilibrium without significantly disturbing the system. By substituting I_{corr} into Equation 5.2, the corrosion rate can also be estimated.

In a LPR measurement therefore both current and potential on the sample (the working electrode) need to be accurately controlled and measured. In an electrochemical cell, this is most typically achieved by using separate electrodes for measuring current and potential [71]. Altogether 3 electrodes are used in such a cell: a counter, a reference and a working electrode.

The reference electrode is used as a potential reference. Since no large current flows on the reference electrode, its potential can be assumed to be constant [71]. The experiments described in this chapter rely on a silver chloride reference electrode (Ag /AgCl), which is denoted on all plots referring to absolute potentials. In contrast, the counter electrode is used to apply the majority of the required current. Its potential is irrelevant, and is not estimated.

To implement this and to measure the corrosion current in an unforced corrosion cell therefore the addition of a reference electrode is required. A new rig was

built in order to add this capability. This is shown in Figure 5.3. The operation of this unforced corrosion rig can be described as follows: first, the sample with a permanently installed waveguide sensor coupled is attached to the rig with its surface polished to 1200 grit. Similarly to the forced corrosion rig, ultrasonic wall thickness measurements are initiated and carried out throughout the experiment using the signal acquisition and processing protocol described in previous sections. The reference electrode and a stainless steel counter electrode are then inserted into the rig. The electrolyte inlet and outlet tubes are then connected to a pump and the chosen electrolyte is cycled through the system. After this, a LPR measurement is initiated using a potentiostat (Gill AC, ACM Instruments, Grange-over-Sands, United Kingdom). The potentiostat is used to first measure the equilibrium potential of the sample. Following this, an overpotential linearly changing in the range of ±20 mV around the equilibrium potential is applied to the working electrode (the sample) over a period of 2 minutes, during which the current that is supplied to the working electrode is measured. The slope of the measured current-overpotential curve is then assumed to be the polarisation resistance R_p of the cell. Such LPR measurements are then repeated every 4 hours in order to track any potential corrosion rate changes. The ultrasonic measurements can be compared to the corrosion rates estimated using the LPR measurements.

It should be noted here that probes that are capable of LPR measurements in

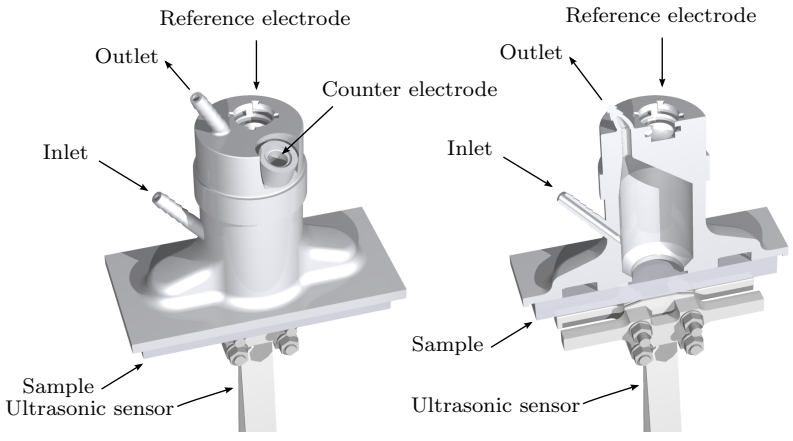

Figure 5.3: Figure a. shows an isometric view of the full unforced corrosion rig, whereas Figure b. shows a cross-sectional view of the same rig. A sample and a waveguide sensor coupled onto the sample is shown on both plots. Note that the ultrasonic sensor is shown in full view (not cross-sectional view) on both figures.

application are commercially available as intrusive probes that can be inserted into pipes. For example, see [70] or the products of Rohrback Cosasco (Santa-fe Springs, USA). There are two main limitations to LPR measurements in applications however. Firstly, the probes are intrusive and if they fail it is a major issue to reinstate them. Secondly, the LPR measurement is best suited to characterise the electrolyte itself rather than the actual effect that it has on the wall thickness. This is because the entire pipe wall acts as an electrode and it is hard to quantify the exact area that the measurement applies to making it mostly a qualitative tool.

5.2.3 pH dependence

The previous sections established two approaches to estimate corrosion current, one for forced and and another for unforced corrosion. Both methods however relied on Equation 5.2 to estimate wall thickness loss based on corrosion current. An implicit assumption in Equation 5.2 was that any material that has oxidised has also been lost in terms of wall thickness. While this assumption is true when corrosion is first initiated on a polished surface, under certain conditions the corrosion product may interfere with any further corrosion. A common everyday example of this is the phenomenon of passivation. Passivation occurs when the corrosion product protects the corroding material from exposure to the corrosive environment hence preventing further corrosion. The behaviour of passivation may be affected by many variables (*e.g.*: material parameters, interaction of electrolyte and material, temperature, etc.). The pH of the electrolyte has been reported to influence the solubility of the corrosion product, and even passivation of mild steel was observed at high pH values [72]. In order to better understand the effect of pH on the corrosion behaviour of mild steel, a Pourbaix diagram of Fe is considered. Pourbaix diagrams show stable phases as a function of pH and absolute potential in aqueous electrochemical systems. The Pourbaix diagram of Fe is shown in Figure 5.4 (reproduced based on [69]).

This diagram is interesting because it shows that at approximately pH 9 and below iron can undergo corrosion in two different oxidation states: as Fe^{2+} and Fe^{3+} [69]. Since both of these species are soluble in water, corrosion at these pH levels is expected result in uniform wall thickness loss. Between pH 9 and 13 however the corrosion product of iron is Fe_3O_4 and Fe_2O_3, which is expected to passivate the

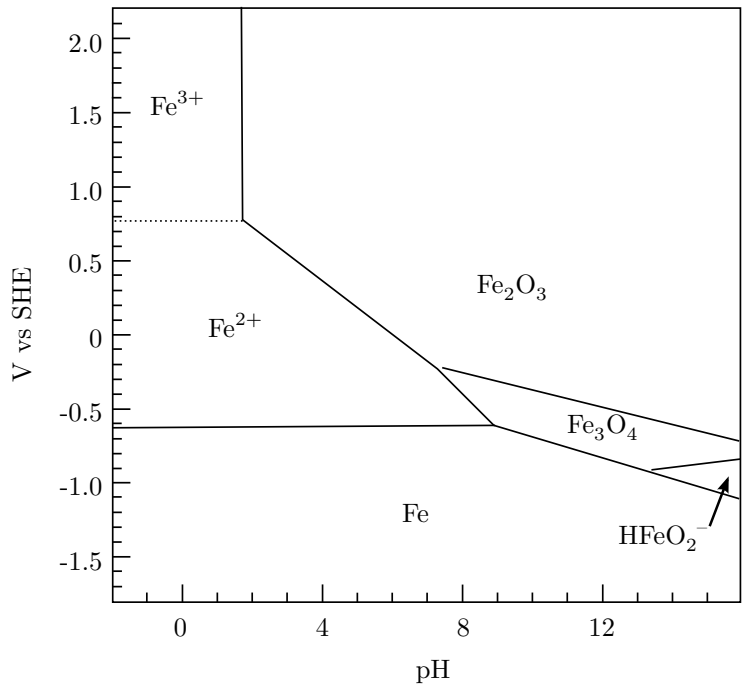

Figure 5.4: Pourbaix diagram of iron in an aqueous electrolyte at 25 °C reproduced based on [69]. Factors such as the concentration of dissolved Fe^{2+} and Fe^{3+} ions as well as temperature also have a small effect on this plot, however these effects are assumed to be negligble in this study.

interface of iron, *i.e.* an oxide layer that stays on the surface of the steel and impedes OH^- ions from reaching the surface so that further oxidation of Fe is slowed down/prevented [69]. In field applications, passivation would typically be considered beneficial, as it hinders further corrosion. When external current is applied with the goal of forcing corrosion however, such as experiments described in this chapter, passivation introduces some uncertainty with regards to how the corrosion will occur. It is expected that as soon the interface of the sample is passivated, the forced current will break down small areas of the passive layer, where further corrosion will occur. This is therefore expected to result in a form of non-uniform thickness loss. In order to evaluate this, as part of the forced corrosion experiments, high pH corrosion was also investigated using Na_2SO_3 as an electrolyte.

5.3 Experimental results with forced corrosion

5.3.1 Forced corrosion using a NaCl electrolyte

The most important aim of this chapter is to establish how accurate the ultrasonic wall thickness loss rate measured using permanently installed sensors is when monitoring throughout the corrosion process. The simplest and quickest way to verify this is by means of forced corrosion. First, a NaCl electrolyte is evaluated. This was chosen since an aqueous solution of NaCl is conductive, making it very suitable for forced corrosion experiments. In addition, it is commonly available, affordable and safe to use.

The forced corrosion rig was set up using a 0.376 w/w % NaCl electrolyte. A mild steel sample with a waveguide sensor coupled was attached to the corrosion rig. A K-type thermocouple was then welded on the sample for the purposes of temperature compensation. Although temperature compensation was used, the rig was placed in a room with relatively stable temperatures, and during the measurements temperature fluctuations of the sample were measured to be less than 0.1 °C during each measurement. Measurements were initiated and operated remotely, so that forced ventilation caused by the operator could be avoided (*e.g.*: any movement or breathing). Once the sample was set up, a forced current was then applied to sample remotely. Multiple rounds of this experiment were carried out with corrosion currents of 2.5mA, 3mA, 5mA and 10mA.

Results of these experiments are shown in Figure 5.5. The figures show relative thicknesses, as it is wall thickness loss that is of interest and not absolute wall thicknesses. The ultrasonic wall thickness estimates were calculated using two arrival times or two peaks (surface and first backwall echo wavepacket). Three peak based thicknesses are not displayed, since they are nearly identical to those of two peak based thicknesses, and hence were omitted from the figure. The figures do not show the temperature of the sample, however it was measured and used for temperature compensation. The temperature of the sample was measured to be within 21.1 ± 0.1 °C throughout all of the measurements and changed less than 0.1 °C during each of the measurements.

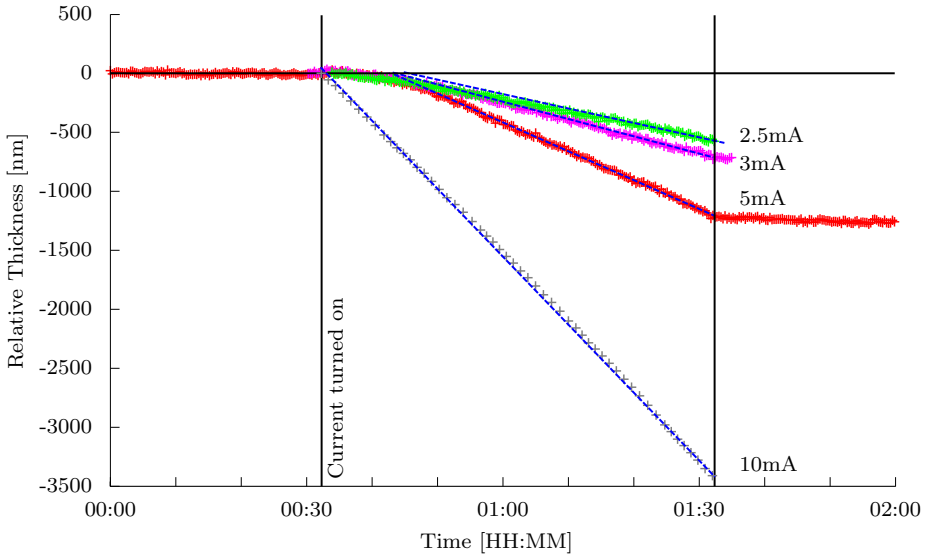

Figure 5.5: Crosses show ultrasonically measured wall thicknesses during 1 hour forced corrosion measurements. Grey crosses show results for 10mA forced current, red crosses are for 5mA forced current, magenta crosses are for 3mA and green crosses are for 2.5mA forced current. The electrochemically predicted corrosion rates for these measurements are shown with blue dashed lines.

As shown by the figure, during first 30 minutes of the measurements, no current was applied. During this period, the standard deviation of ultrasonically measured wall thicknesses was estimated to be approximately 20 nm. As the figure shows, various rates of current were then applied. Applying 10mA corrosion current results in good agreement between predicted and ultrasonically measured wall thickness loss rates. When lower current is applied, such as 3mA or 5mA, a short activation period is introduced. After the activation period, the agreement is good between predicted and ultrasonically measured wall loss rates. It should be pointed out that the predicted corrosion rate for 5mA current is half as high as for 10mA. It may appear contradictory to this, that the overall lost wall thickness caused by 5mA is less than half compared to that caused by 10mA current. This however is caused only by the activation period, which in effect decreases the wall thickness amount lost during the 1 hour period. Another interesting feature of the activation period is that the lower the applied current is, the longer the activation period becomes. It is thought that this is because it takes time to achieve the equilibrium of ion exchange on the sample surface as well as diffusion in the electrolyte. Furthermore, below approximately 2.5mA applied current the wall thickness loss does not settle at a clear rate and instead keeps fluctuating. In summary therefore the corrosion rate is

predictable at high corrosion currents (5mA or above), but becomes less predictable within the observed time frame at low currents (2.5mA or below).

5.3.2 Forced corrosion using a Na_2SO_3 electrolyte

A second experiment was also carried out to evaluate the behaviour of forced corrosion at high pH conditions. For this, a saturated solution of sodium sulfite (Na_2SO_3) was used ($\sim$ 270 g/L [73]). The pH of the saturated solution is reported to be higher than 9, hence it falls within the pH range where passivation of the metal surface is expected.

A measurement was set up initially using an aqueous NaCl solution similarly to the experiment in the previous section. A forced current of 10mA was applied, and the system was left to corrode for a period of approximately an hour, during which the NaCl electrolyte was recirculated to and from an open reservoir. Injection of the saturated Na_2SO_3 solution was then initiated directly into the corrosion rig. After a period of 45 minutes, the injection of the Na_2SO_3 solution was terminated, and the mixture of Na_2SO_3 and NaCl electrolytes was recirculated.

The ultrasonic wall thickness loss measurements during this experiment are shown in Figure 5.6. As the figure shows, the wall thickness loss rate is proportional to applied current while the sample is exposed to NaCl electrolyte. When Na_2SO_3 is injected, a temporary thickness increase is observed. This is thought to be the result of a temporary temperature instability caused by the injected Na_2SO_3 solution, since its temperature was 5 °C higher than that of the NaCl electrolyte. Although both solutions were prepared with constituents of identical temperature, the offset was introduced by the exothermic reaction of dissolving Na_2SO_3 in water. Once the transient temperature effect subsided however, the ultrasonically measured wall thickness loss rate decreased significantly compared to the NaCl solution.

It should be noted here that Figure 5.6 shows both two peak and three peak based thickness estimates. This is because discrepancies between the two estimates are important to clarify. As Figure 5.6 shows, before Na_2SO_3 was introduced to the system, the agreement between two peak and three peak thickness estimates was

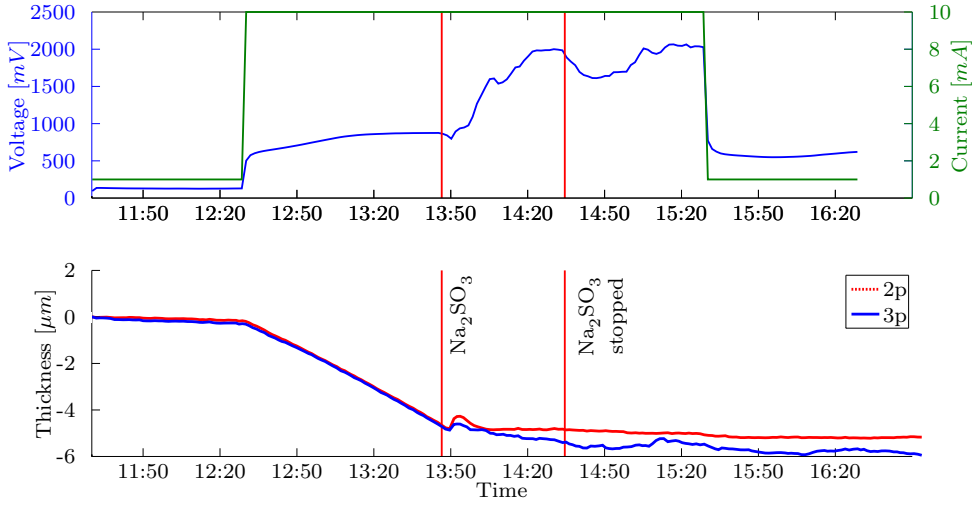

Figure 5.6: Top subplot shows applied current and voltage betweed cathode and anode during a forced corrosion measurement using NaCl and Na_2SO_3 electrolytes. The bottom subplot shows the ultrasonic wall thickness results for the experiment. Red line shows ultrasonic thickness estimates calculated using two peaks (surface and first backwall echo wavepackets) whereas the blue line shown ultrasonic thickness estimates based on three peaks (surface, first backwall echo and second backwall echo wavepackets).

good. When Na_2SO_3 was introduced to the system, the two estimates were no longer in agreement. Visually comparing the backwall of a sample after the Na_2SO_3 experiment to a sample after a NaCl corrosion experiment reveals that the Na_2SO_3 introduced non-uniformity on the backwall surface as shown in Figure 5.7. This non-uniform corrosion is presumed to be the effect of preferential corrosion as the passive layer is broken down. The resulting backwall is expected to interfere with the reflection of ultrasonic signals from it, hence introducing variability in the calculated wall thicknesses.

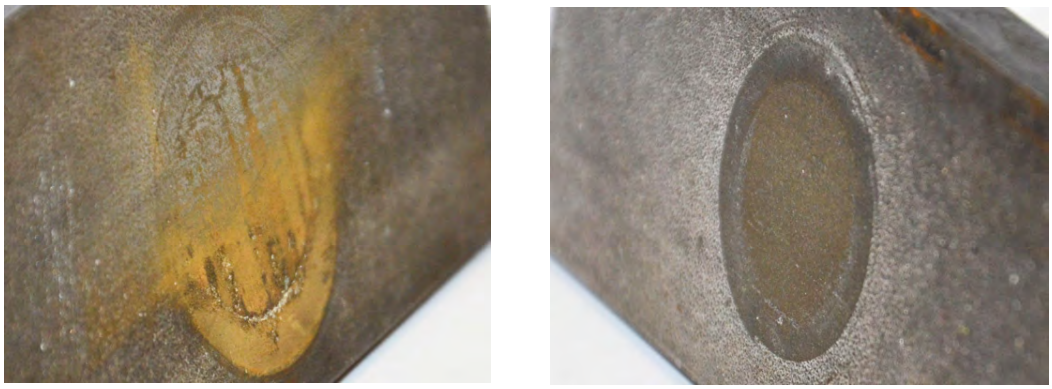

With Na_2SO_3 With NaCL

Figure 5.7: Left photo shows the exposed backwall surface area of a sample that was exposed to forced corrosion using a Na_2SO_3 electrolyte. Right figure shows the exposed backwall surface area of a sample that was exposed to forced corrosion using a NaCl electrolyte

5.4 Experimental results with unforced corrosion

5.4.1 Unforced corrosion using citric acid

The previous section has evaluated the accuracy of estimated wall thickness loss using ultrasonic monitoring techniques described in this thesis. It has shown that wall thickness loss rates of the order of 1 µm per hour caused by forced corrosion can be monitored accurately using ultrasonic techniques. While the previous section verified the potential accuracy of the ultrasonic monitoring methods discussed in this thesis, this was achieved by expediting corrosion processes by applying a current to the sample. Corrosion rates therefore are expected to be relatively high compared to that of unforced corrosion. In this section smaller corrosion rates caused by unforced corrosion are evaluated.

In this section, citric acid is evaluated as an electrolyte. Citric acid was chosen since it is accessible, safe and is expected to result in relatively low corrosion rates. Various concentrations of aqueous citric acid solutions were tested, namely 1%, 0.5%, 0.04% and 0% (distilled water) concentrations by weight. The pH of these solutions estimated to range between pH 3 for the highest concentration of citric acid to pH 7 for distilled water. This was not measured or calculated more accurately, since the induced corrosion is not expected to be linked directly to pH. Instead, it is

noted that the estimated pH range falls within the domain of corrosion without passivation according to the Pourbaix diagram on Figure 5.4. In each experiment 800 mL solution of the given concentration was prepared using distilled water in a 1000 mL vessel. The vessel containing the solution was connected to the unforced corrosion rig according to the diagram shown in Figure 5.8.

Each electrolyte was circulated for 14 hours. A mild steel sample was used for all experiments, ground with 1200 grit emery paper before each experiment. The ultrasonic waveguide sensor was coupled to the sample and was not removed between measurements, in order to maximise repeatability and eliminate uncertainty associated with changing coupling.

During each experiment LPR measurements were also carried out in order to estimate corrosion rates. Before results are shown however, it should be noted that the corrosion rates calculated using LPR measurements are typically affected by various sources of error, and cannot be relied upon unconditionally as an accurate corrosion rate measurement without verification [74]. Relevant error sources include IR drops caused by current flowing through the resistive electrolyte that is exacerbated by poor electrode placement and deviations from linearity in polarisation data [74]. It is expected that a significant error source in the experiments described here is poor location control of the reference electrode, which can result in significant IR drops

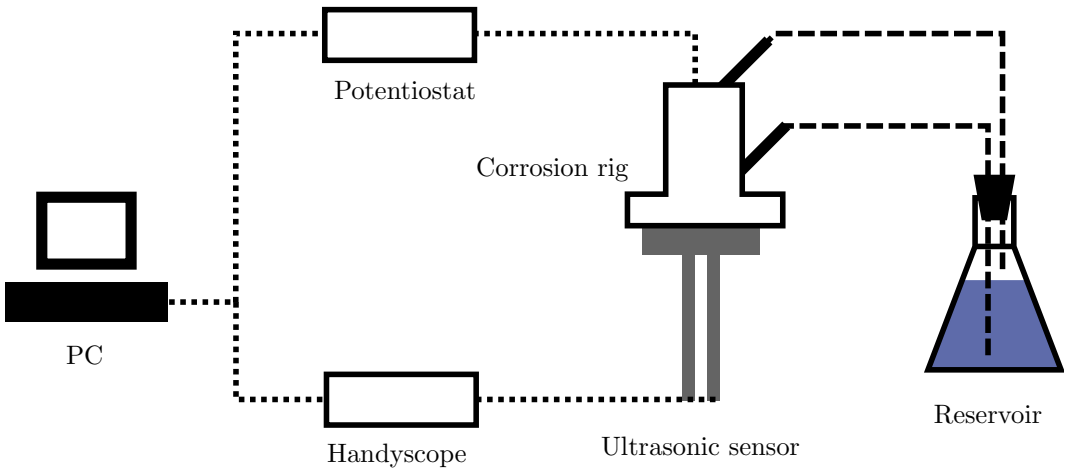

Figure 5.8: Diagram of unforced corrosion rig. Dashed lines show electrolyte tubing, whereas dotted lines show electrical connections. Ultrasonic sensor is upside-down, as this allows the sample to be positioned below the electrolyte, and hence avoid any bubbles collected at the interface.

and therefore skewed LPR measurements. For this reason it would seem sensible that placing the reference electrode close to the sample would result in minimal error. However, this distorts current flow locally, a phenomenon known as shielding [75]. A small capillary referred to as a Luggin probe is sometimes used to minimise this effect, which may be placed close to the surface of the sample as its size is small and it minimally distorts current flow [75]. However in practice Luggin probes are also still subject to some error, as a practical implementation cannot be infinitely small. In addition, standard probes were too large to fit in the unforced corrosion rig and hence a Luggin probe was not used in the experiments described here.

Instead, it is acknowledged that LPR based corrosion rate predictions may be affected by such errors and an approach to compensate them is outlined here. In order to maintain repeatability of the error introduced by poor reference electrode placement, the position of the reference electrode was fixed at 5mm from the sample surface in all experiments. While evaluating corrosion rates based on LPR measurements, it became apparent that all corrosion rates measured using this LPR setup are a factor of 2 less than ultrasonically predicted wall loss rates. It was assumed that this was caused by the poor reference electrode placement. As a compensation approach, all presented LPR corrosion rates in this thesis are multiplied by a factor of 2 and are referred to as scaled LPR corrosion rates.

Wall thickness loss estimates based on scaled LPR measurements and ultrasonically measured relative wall thicknesses are shown in Figure 5.9. It can be seen from the figure that higher concentration of citric acid in principle results in higher rates of wall thickness loss. It is also apparent, that there is a saturation effect observed at a citric acid concentration of 0.5% and higher. Increasing citric acid concentration beyond 0.5% does not further increase the corrosion rate.

Overall, the agreement between ultrasonically measured wall thickness loss and the scaled LPR results is good. Before quantitative conclusions are drawn however, potential sources of error in the ultrasonic measurements are discussed here. As Figure 5.9 shows, the ultrasonic wall thickness loss rate estimates are not as linear as seen in forced corrosion measurements. It can also be seen that deviations from the scaled LPR thicknesses are up to 1 µm for the measurements shown in green on the figure. Although this drift is most clear at 0.04% concentration (shown in

green), smaller drifts can also be observed in the rest of the measurements as well. This is thought to be the effect of temperature, as the temperature conditions of unforced corrosion experiments were less controlled compared to forced corrosion experiments described in the previous section. While the widest temperature range during forced corrosion experiments was 0.1 °C, the temperature during the 0.04% citric acid measurement was 27 ± 2 °C - therefore an overall temperature range of 4 °C. According to calculations in Chapter 4, a temperature measurement error of just ~ 0.5 °C may result in an error of 1 µm and therefore temperature inaccuracies are the likely source of this error.

In summary, the biggest deviations of ultrasonic measurements from scaled LPR corrosion rate predictions were of the order of 1 µm. Since an interesting application of such measurements is prediction of yearly corrosion rates, it is valuable to calculate the smallest detectable wall thickness loss rate based on the determined sensitivity. The smallest detectable wall thickness loss rate within 24 hours is expected to be 1 µm/day ~ 0.35 mm/year. Similarly, the smallest detectable wall thickness loss in 7 days is expected to be 1 µm/week ~ 0.05 mm/year.

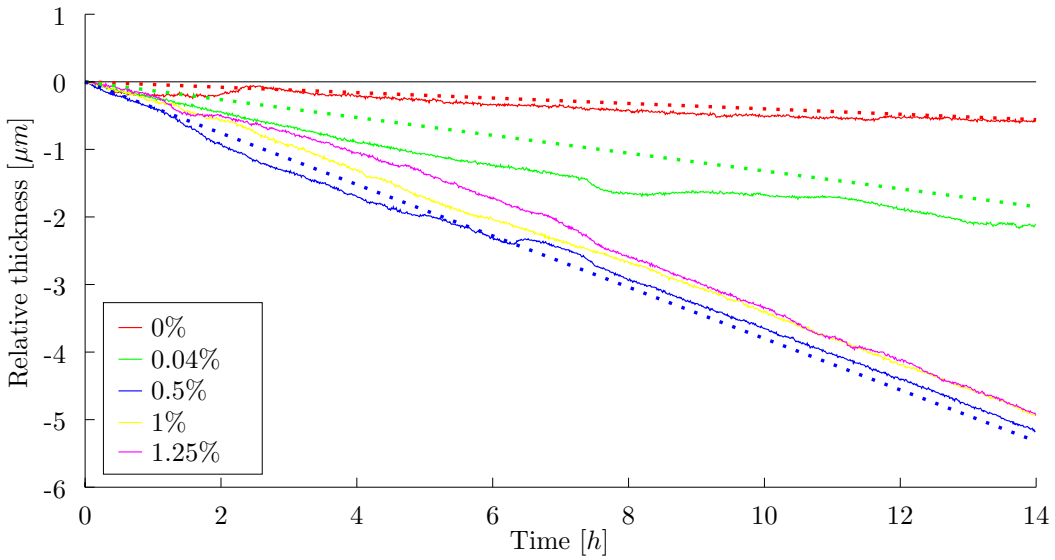

Figure 5.9: Figure shows wall thickness loss estimates during unforced corrosion experiments with various concentrations of citric acid. Ultrasonically estimated wall thicknesses (based on two peaks) are shown with solid lines, while scaled LPR wall thicknesses are shown with dotted lines (note that the blue, yellow and magenta dotted lines overlap). Colours refer to various concentrations of citric acid. Distilled water results are shown in red, citric acid concentration of 0.04% is shown in green, 0.5% is shown in blue, 1% is shown in yellow and 1.25% is shown in magenta.

5.4.2 Unforced corrosion using hydrochloric acid (HCl)

In addition to citric acid, the effect of hydrochloric acid (HCl) was also evaluated. HCl was chosen as it is more frequently encountered in the petrochemical industry. In this section an electrolyte concentration of 1M (3.5 w/w %) was investigated. This concentration is 12 times diluted compared to concentrated 12M (37 w/w%) HCl [76] and was chosen because reports of such concentration are prevalent [77–81].

As described above, a wide array of papers have been dedicated to evaluating the corrosion effects of HCl on mild steel, a selection of which is referred to here [77–81]. All of the referred papers evaluate the corrosion inhibition effect of either heat treatment methods or corrosion inhibitor chemicals in 1M HCl solutions. While they focus on various corrosion inhibition effects, as control measurements they all evaluate the corrosion rate caused by the 1M HCl solution on untreated mild steel samples without any corrosion inhibition. Estimated uninhibited corrosion rates in referred papers vary between ~ 2 mm/year to ~ 80 mm/year.

It is apparent that the corrosion rate depends on factors that are not considered in this thesis. These are thought to be temperature effects on corrosion processes, oxygen availability at the sample, contaminants such as other ions dissolved in the electrolyte, etc. It falls outside the scope of this thesis to evaluate how each of these influences may affect corrosion phenomena. Instead, it is concluded that estimated corrosion rates based on literature alone cannot be relied upon exclusively and accurate online measurements of corrosion rates are key.

The unforced corrosion cell was therefore set up using a 1M HCl solution. The experimental procedure used for HCl was otherwise identical to that of citric acid, the HCl solution was circulated in the rig inducing corrosion without applying an external current. LPR corrosion rates and ultrasonic thickness estimates were also measured during the measurement. The results of the experiment are shown in Figure 5.10.

As the figure shows, both two peak and three peak measurements are displayed. Although deviations of approximately 0.5 µm are measured from the linear fit, it is also apparent that these deviations occur during periods of temperature transients.

It should be noted here that temperature propagation simulations were carried out in previous sections, that quantified the error in ultrasonic thicknesses as a result of temperature gradients within the sample. These simulations however assumed that the temperature of air on the outside surface of the sample were constant and evaluated gradients caused by internal temperature changes only.

Air temperature changes on the outer side of the pipe may however also introduce error, since the thermocouple measuring the temperature of the sample is directly exposed to that environment. Such errors are expected to be highly specific to thermocouple type, thermal mass of thermocouple, insulation of thermocouple from air, air flow directly affecting the thermocouple, etc. It is thought that insulating the thermocouple and preventing direct airflow would minimise such error, this was not implemented however. Instead, the error introduced by the thermocouple sensor that was used in this thesis is considered, which was consistently less than 1 µm. This may not be representative of what could be achieved in field, but it is thought that protecting the temperature sensor from rapid temperature changes should minimise error in such conditions as well and hence comparable results should be achievable. As a final thought, it should also be noted that by continuously

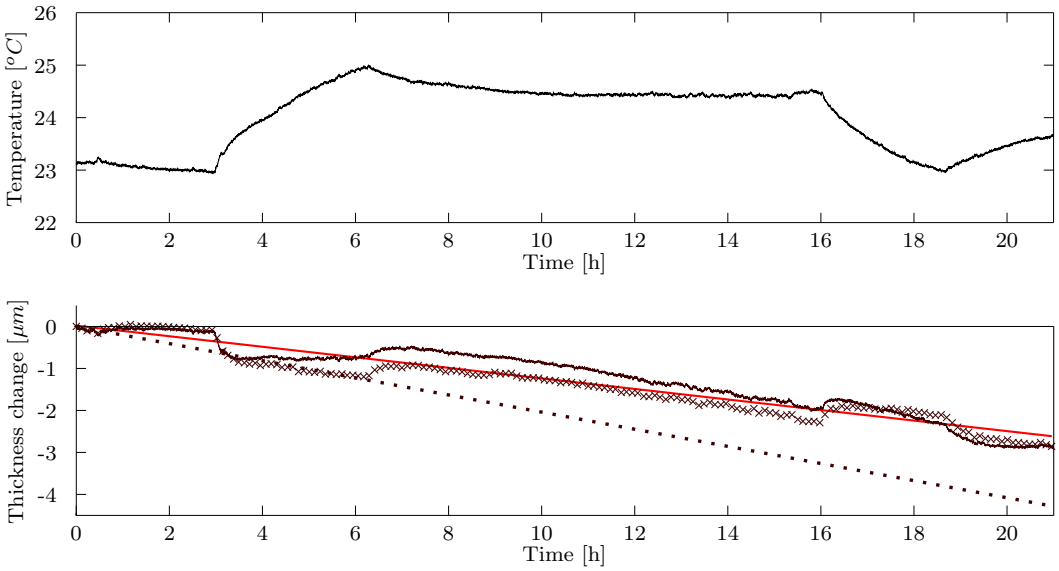

Figure 5.10: Top subplot shows the measured temperatures during the unforced 1M HCl corrosion experiment. Bottom subplot shows the scaled LPR corrosion rates (dotted line), three peak ultrasonic wall thickness estimates (crosses), two peak ultrasonic wall thickness estimates (solid line) and a linear fit applied to two peak thicknesses (red line).

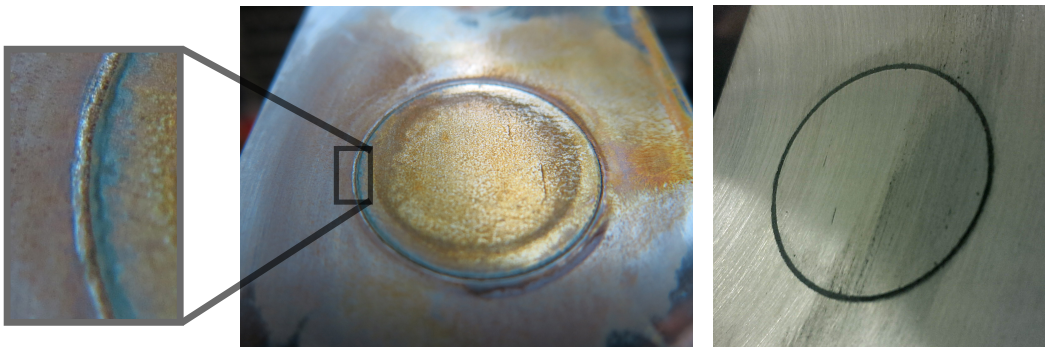

a. Before polishing

b. During polishing

Figure 5.11: Figure a. shows the patch of backwall surface of the mild steel sample that was exposed to a 1M HCl electrolyte during a 20 hour unforced corrosion experiment. A separate zoomed in image highlights a groove. Figure b. shows the same surface during grinding and repolishing highlighting the groove.

monitoring temperature it is possible to identify time periods when temperature gradients are low, during which ultrasonic measurements are expected to be accurate.

Having acknowledged the apparent small drifts on the figure, it is clear that overall the ultrasonically measured wall thickness loss rates are close to linear. Over a period of 20 hours a wall thickness loss rate of approximately 2.5 µm/20 hours = 3 µm/day = 1mm/year was measured using both ultrasonic wall thickness estimating methods, whereas 4.5 mm/20 hours = 5.2 µm/day $\sim$ 2 mm/year was measured using the scaled LPR measurements. The corrosion rate predicted by scaled LPR measurements therefore falls within the order of magnitude of possible corrosion rates as reported in the literature [77–81].

The ultrasonically estimated corrosion rate is therefore lower than that of scaled LPR measurements. This is explained once the bottom surface of the sample is inspected, this is shown in Figure 5.11. As the figure shows, a groove was noted on the 1M HCl corroded sample. This indicates that the sample preferentially corroded below the O-ring. According to [82], chloride ions concentrate in crevices and even low levels can lead to corrosion, which is known as crevice corrosion.

This preferential corrosion below the O-ring explains the difference between LPR and ultrasonic estimated corrosion rates. Ultrasonic measurements interrogate the surface area directly below the sensor, and hence are not influenced by corrosion near the O-ring. LPR measurements however estimate corrosion loss based on electrochemical

measurements of the entire surface, and hence provide an average estimate over that surface. Since the corrosion rate under the small area of the O-ring is high, it increases the average of LPR corrosion rate estimates compared to the ultrasonic ones. Hence this result is in line with expectations when observing a preferential corrosion phenomenon.

5.5 Summary

In this chapter it was demonstrated that permanently installed ultrasonic monitoring can be used to accurately monitor wall thickness loss caused by corrosion. It was shown that under stable temperature conditions the standard deviation of ultrasonically estimated wall thicknesses was 20 nm. It was also shown in forced corrosion experiments that a uniform wall thickness loss rate of less than 500 nm is detectable within one hour under stable temperature conditions. It was not possible to predictably force corrosion of less than 500 nm per hour, and hence lower rates could not be verified using forced corrosion.

In unforced corrosion experiments wall thickness loss rates between 35 nm and 350 nm per hour were investigated. Temperature conditions during unforced measurements were not kept stable and it was pointed out that ambient temperature changes introduced small temporary drifts in ultrasonic measurements. It was concluded that even with such drifts, wall thickness loss can be detected and accurately monitored once it exceeds 1 µm total wall thickness loss. As an example, 0.1 mm/year wall thickness can be detected in 3.65 days. This is exciting because 0.1 mm/year wall thickness loss rate in industry is the approximate threshold above which active control of corrosion is considered. Achieving response times of the order of a few days for ultrasonic measurements potentially opens the door to use the wall thickness loss measurements for the purpose of optimising process conditions.

It was also demonstrated that ultrasonic wall thickness measurements interrogate the area of the sample that is directly below it, and so wall thickness measurements are not affected by corrosion in other areas of the material where the ultrasonic beam does not interact with the surface. In contrast to this, it was found that the

LPR measurements averaged data over the whole electrode area so that also crevice corrosion around the O-ring of the rig influenced the recorded corrosion rate.

Chapter 6

Material Degradation Mapping

6.1 Introduction

Techniques presented in this thesis concentrate on maximising the precision of time-of-flight based ultrasonic monitoring. Wall thickness loss monitoring is a common application of this and is the main focus of the thesis. However, it is also possible to estimate the propagation velocity of ultrasonic waves using the same time-of-flight measurements when the distance of propagation is known. It is expected that the progress of material degradation mechanisms that weaken the structure due to voiding, for example high temperature hydrogen attack (HTHA), can also be monitored by tracking ultrasonic travel time. This is because the small voids caused by HTHA change the properties of the bulk material, which in turn is expected to result in effective ultrasonic propagation velocity changes.

This chapter starts by reviewing literature on hydrogen attack. This review elaborates on how hydrogen attack can be modelled in experiments and also links propagation velocity changes to the volume fraction of voids in a material. A feasibility study is then described, with the goal to create a non-uniform ultrasonic velocity distribution within the material via another simpler method. This is achieved by applying heat and creating a non-uniform temperature distribution in the sample, which can be linked to propagation velocity changes. Ultrasonic measurements are carried out using a waveguide transducer array on a heated sample, in order to collect data

from as many angles of the non-uniform temperature distribution as possible. A review of imaging methods is then presented, with the aim to reconstruct the entire non-uniform temperature map. The implementation of two imaging methods are then described in more detail, which are used to reconstruct the temperature maps.

Following the feasibility study relying on heat to introduce a non-uniform propagation velocity map, an experimental rig that was conceived to physically induce hydrogen attack is presented. The presented method induces hydrogen attack electrochemically by forcing electrolysed hydrogen into the steel. The experiment needs to take place at high temperature and the steel sample is therefore immersed in molten salt as outlined by Tsubakino [83]. Measurements from the rig, acquired using permanently installed ultrasonic sensors while hydrogen attack is being induced are then presented. Following this, the results are discussed and conclusions are drawn.

Some of the material described in this chapter has been published in [P4].

6.2 Hydrogen Attack

The phenomenon of hydrogen attack has attracted substantial attention over the years. The mechanism of the degradation is well known: it occurs in carbon steels when hydrogen diffuses into the steel at high partial pressures and produces methane further reacting with the metal carbides [84]. Therefore cavities filled with high pressure methane are formed. This degradation poses a complex problem as it can reduce the structural strength of the material [85]. Design codes have been introduced based on the Nelson curves to avoid certain grades of steel in environments that are susceptible to hydrogen attack [1], but there have still been failures in equipment that has been in service for long periods [86] and the Nelson curves have been adjusted several times. Prescott [86] concludes that the equipment operating under conditions that cause hydrogen attack should be considered as if it was degrading even if the operation of the equipment was designed according to the Nelson curves. It is necessary therefore to monitor the condition of the vessel in use.

It is thought that ultrasonic detection of hydrogen attack is potentially achievable. The ultrasonic properties of the degraded material are expected to change due to the

methane voids. This has previously been exploited, however currently implemented detection techniques are very much operator dependent and therefore the reliability of testing is subjective [87]. In addition, the accuracy of standard coupled velocity measurements is not well reported when used for material degradation. Yi *i.e.* [88] carried out thickness measurements relying on times of flight using standard coupled probes and concluded that the uncertainty of time of flight measurements may be up to 1 mm/10 mm = 10%. This is not sufficient for accurate evaluation of hydrogen attack.

Based on a report by Eliezer [89] the diameter of the voids caused by hydrogen attack is in the order of 2 µm - the wavelength of the ultrasonic signal used (frequency in the range of 1-10 MHz) is of the order of 1 mm which is 3 orders of magnitude larger than the microstructural changes and suggests that these changes can be modelled as changes to the bulk ultrasonic parameters. Significantly higher frequencies however cannot be used for the measurement because of attenuation problems.

Chatterjee [90] proposes to estimate the changes by calculating the effective bulk modulus and density (using a simple 'law of mixtures' equation) of a voided material. This can be used to evaluate the altered ultrasonic propagation velocity in the following way:

$$\varrho_{effective} = (1 - v_f)\varrho_{material} + v_f\varrho_{void} \tag{6.1}$$

$$\mu_{effective} = \mu_{material}(1 - 45/23v_f + 2.1v_f^2) \tag{6.2}$$

$$c_{voided} = \sqrt{\frac{\mu_{effective}}{\varrho_{effective}}} \tag{6.3}$$

where $\varrho_{material}$ and ϱ_{void} are the densities of the bulk material and of the void, v_f is the void fraction, μ is the shear modulus and c is the propagation velocity of shear waves. The resulting relationship between propagation velocity and void fraction in the range of interest of this study ($v_f = 0\% - 3\%$) is close to linear:

$$c_{voided} = p_1 \cdot v_f + p_0 \tag{6.4}$$

where $p_1 = -16.25\frac{\mathrm{m}}{\mathrm{s}}$ and $p_0 = 3246.7\frac{\mathrm{m}}{\mathrm{s}}$ are the linear fit coefficients for $v_f = 0\% - 3.5\%$. The maximum error of the fit is $0.44\frac{\mathrm{m}}{\mathrm{s}} = 0.01\%$.

There are more advanced models than the Chatterjee model, see *e.g.* Hirsekorn *i.e.* [19] and Caleap *i.e.* [21]. At late stages of the material degradation approaches such as proposed by Bowler *i.e.* [91] should also be considered. The Chatterjee model however is a suitable approximation at low void fractions where the voids are uniformly distributed. These are all expected to be valid assumptions at the onset stage of hydrogen attack.

6.3 Non-uniform Propagation Velocity Distribution

Although the conditions at which hydrogen attack occurs are well established, it is still difficult to induce it in laboratory conditions. This is because hydrogen is highly flammable, and is therefore dangerous at high temperatures. In order to quickly evaluate whether it is feasible to monitor hydrogen attack using permanently installed ultrasonic sensors, an alternative approach is described here. It is proposed to create a non-uniform velocity distribution similar to what would be the observed in hydrogen attack within a sample by means of heating. The waveguide transducers that are used in this thesis are designed to withstand high-temperatures, therefore

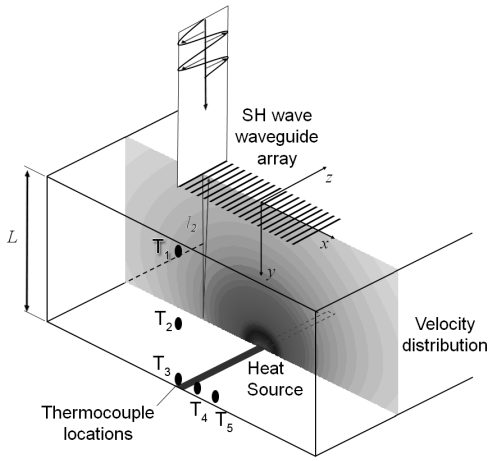

Figure 6.1: Sketch of setup with steel specimen and cylindrical heating element. The central temperature profile is assumed to be 2 dimensional and hence simulations of this region are shown in Figure 6.2. The location of the thermocouples relative to the test piece and the sensor assembly are shown as $T_1 - T_5$. (The location of T_3 is at $x = 0$ as shown on the image)

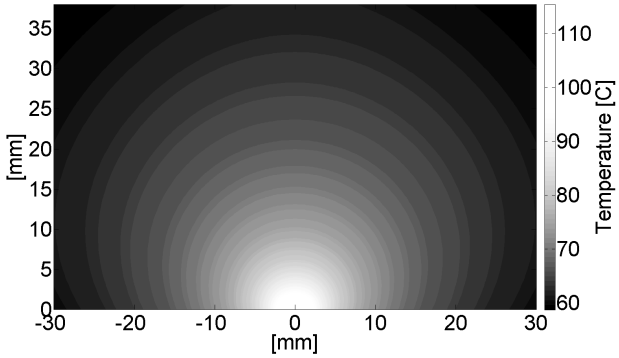

Figure 6.2: An example of a simulated 2D temperature distribution. The parameters of the simulation are described in Section 6.5

this approach seems like an ideal choice as the propagation velocity changes can be introduced in a short period of time.

The aim is therefore to create a 2D temperature distribution within the measurement plane of the test piece. In order to achieve this, a 100 mm long 500W cylindrical ($D = 10$ mm) heating element (sourced from: RS Components Ltd. Birchington Road, Corby, Northants, NN17 9RS, United Kingdom, stock number: 724-2103) was used to create a temperature distribution that could be modelled in 2D at the central plane of the test piece as shown in Figure 6.2. Since the relationship between the local temperature and ultrasonic propagation velocity is known, a one dimensional ultrasonic array attached to the surface of the plate can monitor the 2D spatial changes in the ultrasonic propagation velocity within the material. This configuration has also been investigated in simulations (illustrated by Figure 6.2) in order to be able to assess the proposed reconstruction techniques in a noise-free environment. The simulations were based on a two-dimensional steady state heat conduction model described in [60].

6.3.1 Calibration of the Ultrasonic Propagation Velocity's Dependence on Temperature

In order to accurately convert the propagation velocity values to temperature, a calibration measurement is needed on the sample that will be used for this feasibility study. Although the calibration curves established in a previous chapter of this thesis

could be used, the calibration is repeated here to maximise accuracy. The sensor assembly comprising of 20 waveguide sensors and a clamping assembly was slowly heated up to 120 °C with a Corning 6796-620D hotplate (Corning Incorporated, Tewksbury, USA) by placing the bottom of the sample on the hotplate and insulating it on all sides using rockwool. During this, the temperature distribution within the sample was measured using 5 K-type thermocouples at the locations shown in Figure 6.1. The heating gradient of the hotplate was chosen to be sufficiently low to ensure uniform temperature distribution, as verified by the thermocouples (all showing the same temperature to within less than 1 °C). Based on Equation 6.5 and assuming homogeneous temperature distribution the calibrated propagation velocity-temperature curve was calculated according to the following equations and is shown in Figure 6.3.

$$c_{ij}^{calib} = \frac{2\sqrt{\frac{d_{ij}^2}{4} + T^2} - d_{ij}}{T_{ij}^{SBW}} \tag{6.5}$$

$$\overline{c}^{calib} = \text{mean}(c_{ij}^{calib}) \tag{6.6}$$

$$\overline{c}^{calib} = k_1\Theta + k_0 \tag{6.7}$$

where d_{ij} is the nominal separation between waveguides number i and j, T is the thickness of the test piece, c_{ij}^{calib} is the calibrated propagation velocity at each temperature between waveguides number i and j, t_{ij}^{SBW} is the time of flight difference between surface wavepacket and backwall echo wavepacket (described in detail in Section 6.6.2), $\overline{c}^{calib}$ is the average calibrated velocity at each temperature level

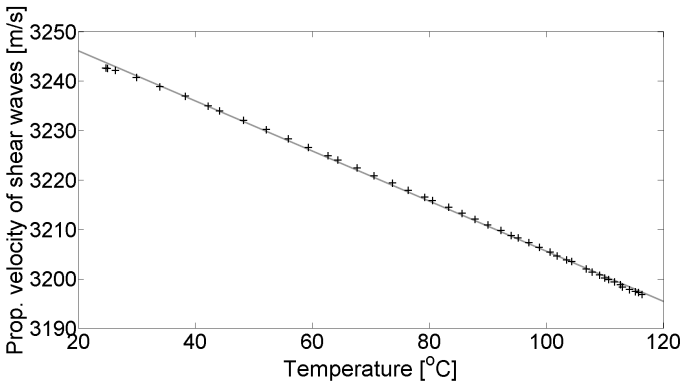

Figure 6.3: Measured ultrasonic shear velocity within the temperature range from 25 °C to 116 °C (crosses) and their linear fit (continuous line). Each measurement point is the average of 380 waveforms measured at each temperature level

(calculated as the arithmetic mean of all obtained c_{ij}^{calib} values), k_1 and k_0 are the parameters determined by the calibration, and Θ is the temperature. Altogether 380 waveforms were evaluated at each temperature level and so each calibration point is the average of 380 propagation velocity values. The relationship between the propagation velocity and temperature is assumed to be linear and is described by equation 6.7. The linear fit for the calibration points resulted in the following constants: $k_1 = 3254.9\frac{\mathrm{m}}{\mathrm{s}}$ and $k_0 = -0.4981\frac{\mathrm{m/s}}{^{\mathrm{o}}\mathrm{C}}$. This is comparable to the calibration curves obtained in Chapter 4. According to the results of the calibration measurement and the estimated effects of hydrogen attack, the ultrasonic velocity change over the temperature range investigated in this study $(20 - 110^oC)$ is equivalent to a void fraction of $0 - 3.5\%$ of hydrogen attack (using Equation 6.4 as an estimate).

6.3.2 Reconstruction Algorithms

The goal of the reconstruction is to quantitatively extract the ultrasonic propagation velocity map within the material based on the data from the waveguide sensor array. It is therefore important to choose a reconstruction algorithm suitable for the conditions of the measurements described in this chapter. In order to choose the appropriate imaging approach the main aspects of currently existing techniques are considered, namely the underlying physical assumptions and possible solution methods.

Several possible wave propagation modelling approaches may be considered from an imaging point of view. The most widely used modelling approaches are the straight and bent ray approximations [92], [93], both of which ignore diffraction and so the potential resolution of the reconstructed image is limited. The advantage of these approaches however is that they are relatively easy to implement and should result in a robust algorithm especially in the case of a low contrast image.

In order to account for diffraction the Born or the Rytov approximations are commonly considered [94]. Their advantage is a potential resolution gain, however these assumptions are highly restrictive as they require the observed object to be low contrast and small relative to the wavelength and potentially result in the reconstruction being more sensitive to noise.

Another option is the non-linear, full wave inversion method [95]. This approach uses a numerical approximation (*e.g.* finite difference method) of the underlying wave equation as its physical model. The selected solution method must then determine a suitable set of parameters (*e.g.*: material properties at all points on a grid) such that the signals from the model match the measurements from the array. In theory this approach avoids the problems associated with the approximations described above, however its implementation is complicated and experimental issues are difficult to account for using a forward model, so very high signal-to-noise ratio data, taken from a very controlled environment is required for such a method to be of practical use.

As mentioned above, another critical aspect of the imaging approach to consider is its solution method. Traditionally direct solution methods were used, often based on the Fourier transform (for example straight ray tomography based on the Fourier Slice theorem) [94]. Such an approach is particularly attractive if the reconstruction is carried out with data from a simple array configuration, such as a circle, which allows parallel projections through the object or if computing resources are limited. Fast modern processors, however, allow iterative algorithms to be employed; iterative methods are often easier to implement and are suitable for more general sensor configurations.

In this chapter the imaging is carried out based on the projection data measured by a waveguide sensor array, which means that the limited field of view of the setup combined with the high level of noise means that little additional information could be extracted through the more accurate physical modelling methods. A straight ray imaging approach using the Kaczmarz method as an iterative solver [96] was therefore selected for reconstructing the velocity map. Altogether this has the advantage of being relatively insensitive to noise and fairly simple to implement while still providing an accurate reconstructed image [94]. The details of the implementation are discussed in Section 6.4.1.

As an alternative approach to address the problem of limited field of view and the noise levels of the measurements an Assumed Distribution method is considered. It is expected that the most apparent issue of the reconstruction will be the lack of sufficient vertical resolution regardless of the reconstruction method, as the dataset simply does not include horizontal projections. It is proposed therefore

as an alternative reconstruction approach to assume a vertical distribution of the ultrasonic propagation velocity based on considerations related to the cause of propagation velocity change. This allows for the data from low angle, long wavepaths to be replaced, which are therefore the lowest signal-to-noise ratio waveforms of the dataset. Instead, assumptions of vertical propagation velocity distribution are used. In the case of this study the propagation velocity change is caused by temperature inhomogeneities around a point-like heatsource, which is approximated by an exponential distribution as further explained by Section 6.4.2. As hydrogen attack is linked to diffusion of hydrogen into the steel it may be possible to model it just like temperature diffusion.

6.4 Implementation of reconstruction

Based on the approach introduced in previous sections, the reconstruction of the spatial ultrasonic propagation velocity distribution from the time of flight data acquired by the waveguide sensor array is considered in this section. Two different algorithms are investigated: the Kaczmarz algorithm, which uses only geometrical assumptions about the positions of the transducers and the time of flight data extracted from the 380 acquired waveforms and the Assumed Distribution method, which uses only the data acquired by adjacent transducers and assumptions about the temperature distribution within the material. These methods are described in detail below.

6.4.1 The Kaczmarz Algorithm (Algebraic Reconstruction Technique)

The assumption of the Kaczmarz algorithm is that the image reconstruction based on the observed data is described by the following equation:

$$Ax = b \tag{6.8}$$

where $b = (b^1, ..., b^M) \in \mathbb{R}^M$ is the observed data (in this case the time of flight

data), $x = (x^1, ..., x^N) \in \mathbb{R}^N$ is the actual image (distribution of ultrasonic shear wave velocity in the sample), and $A = A_{ij}$ is a non-zero $N \times M$ matrix that describes the relationship between the observed data and the points of the image. Each row of matrix A contains therefore coefficients of each wavepath linked to all of the points of the image. The main problem of the reconstruction based on equation (6.8) is the large data dimension and noise in the observed data. The Kaczmarz method (also referred to as Algebraic Reconstruction Technique (ART) [96]) is one of the most popular solvers of overdetermined linear systems [97], [98].

Because of its iterative nature this approach addresses the problem of large data dimensions. It is also relatively simple to implement - every iteration step calculates:

$$x_{k+1} = x_k + \frac{b_i - \langle a_i, x_k \rangle}{||a_i||_2^2} a_i \tag{6.9}$$

where x_k is the k^{th} iteration of the reconstructed image, $i = (k \bmod m) + 1$ and $a_i, ..., a_N \in \mathbb{R}^N$ denote the rows of A. Therefore the algorithm cycles through the rows of A and adjusts a part of the reconstructed image based on the criteria described by the given row of A and the measured data (b). This essentially means that in each cycle the algorithm adjusts some of the pixels in the image (as described by the rows of A) based on the backwall echo arrival time of each wavepath. After cycling through the data enough times the image is expected to converge to the real distribution.

In order to increase the convergence rate of the original Kaczmarz algorithm a randomization is introduced so that the rows would not have to be reevaluated one after another, but in a random order [97] with the aim to speed up the iteration.

It is necessary therefore to set the probability of each row. Strohmer and Vershynin in [98] and [99] propose to set the probability to the Euclidean norm of the row, and therefore the revised algorithm is described by:

$$x_{k+1} = x_k + \frac{b_{p(i)} - \langle a_{p(i)}, x_k \rangle}{||a_{p(i)}||_2^2} a_{p(i)} \tag{6.10}$$

where $p(i)$ takes the values in $\{1, ..., N\}$ with probabilities $\frac{||a_{p(i)}||_2^2}{||A||_F^2}$. Here $||A||_F$ denotes the Frobenius norm of A. The implementation of this algorithm and the calculation

of constants are described in the next section.

The calculated average velocities for each wavepath are used as input data (see Section 6.6.2). In order to be able to discretise the spatial distribution of the propagation velocity a grid was created to serve as the image of the reconstructed velocity map. The resolution of the image can be chosen arbitrarily - the resolution in this chapter was chosen to be 1.5 pixels per millimetre, resulting in a resolution of 85 by 57 pixels. The reconstruction also requires matrix A (in equation 6.8) to be determined. This matrix quantifies the relationship between the velocity at each pixel and the measured data. The pixels are assumed to have an effect on the average velocities of the wavepaths in a certain distribution - in this calculation a polynomial distribution function has been used weighted by the y coordinate of the pixel described by equation 6.11,6.12, which are therefore necessary to produce a smooth image.

$$P_{mn} = \frac{M_T - M_0}{T} y_n + M_0 \tag{6.11}$$

$$A_{mn} = d^r - (\frac{l}{P_{mn}})^r \tag{6.12}$$

where P_{mn} is the weighting coefficient based on the y_n coordinate of pixel n, r is the exponent of the polynomial distribution, d is the nominal separation between neighbour waveguides, l is the distance between the given wavepath and point and A_{mn} are the elements of the matrix A defined by equation 6.8. The distribution described by Equation 6.12 (effectively the shape of an upside-down parabola curve) has negative values - these have to be replaced by zeros in order to achieve the intended functionality. The approximation therefore weighs in pixels close to the wavepath more than the ones further away from it, as shown in Figure 6.4. The following values have been used for the coefficients mentioned above: $r = 0.1$, $M_0 = 0.5$, $M_T = 4$. As an example one row of the A matrix is shown in Figure 6.4 reshaped as an image.

With all the constants defined, the reconstruction algorithm requires an estimated image with which to start the iteration. For this purpose the calculated propagation velocities for each wavepath are averaged for each pixel, weighted by the corresponding coefficients in matrix A. The resulting image is taken as step 0.

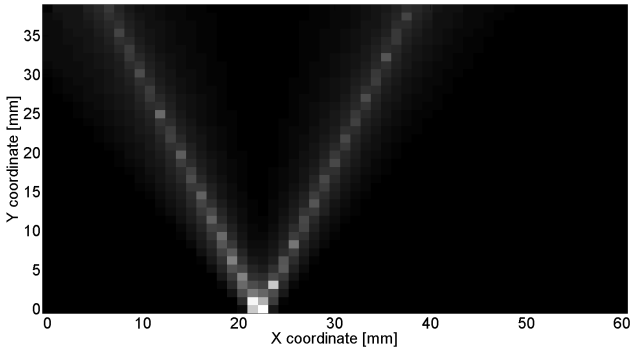

Figure 6.4: Coefficients for the wavepath between waveguide number 3 and 12 and each point of the velocity map

6.4.2 Assumed Distribution Method

An alternative reconstruction method is proposed based on the following considerations: the temperature distribution is assumed to be exponential around the heatsource, therefore its spatial distribution can be described by the following:

$$\Theta(r) = \exp\left(-q_1 \cdot r + q_0\right) + \Theta_0 \tag{6.13}$$

$$\Theta(x, y) = \exp\left(-q_1 \sqrt{(x - x_0)^2 + (y - y_0)^2} + q_0\right) + \Theta_0 \tag{6.14}$$

where r is the distance from the point-like heat source, x and y are the horizontal and vertical coordinates of points where the temperature is evaluated, x_0 and y_0 are the coordinates of the heat source, Θ_0 is a temperature constant describing the asymptote of the temperature distribution function and q_1 and q_0 are the parameters for which the equation will be solved. In practice x_0 is determined as the mean x coordinate of the waveguide pair registering the biggest temperature (which is equivalent simply to the waveform with the biggest time of flight change), whereas y_0 is assumed to coincide with the bottom surface of the flat backwall. The relationship between propagation velocity and the temperature is assumed to be linear which is defined by equation 6.7. Equations 6.7 and 6.14 yield the formulation of the spatial distribution of the propagation velocity (equation 6.15):

$$c(x, y) = k_1 \cdot \left(\exp\left(-q_1 \cdot \sqrt{(x - x_0)^2 + (y - y_0)^2} + q_0\right) + \Theta_0\right) + k_0 \tag{6.15}$$

In order to be able to evaluate the function described by Equation 6.15, the time of

flight data from the neighbouring waveguides are taken into consideration, because the closer the waveguides are, the higher the amplitude of the received signal is and this results in high signal to noise ratio and low variability in the measurements. Using $c_{ij}^{S,corr}$ (defined in Section 6.6.2) and the surface velocity as boundary conditions the equation can be solved for a and c in an iterative way.

$$q_0(x) = \ln(\frac{c_{surface} - k_0}{k_1} - \Theta_0) + q_1\sqrt{x_{ij}^2 + y_{ij}^2} \tag{6.16}$$

$$c_{ij}^{corr} \cong \frac{L}{\int_0^L \frac{1}{k_1(\exp(-q_1 \cdot \sqrt{(x_{ij}-x_0)^2+(y-y_0)^2}+q_0)+\Theta_0)+k_0} dy} \tag{6.17}$$

where x_{ij}, y_{ij} is the coordinate of the surface point halfway between waveguides i and $j = i + 1$ and y is the vertical coordinate of the pixel to be evaluated (vertical resolution can be arbitrary, as the assumed temperature distribution function can be evaluated at any number of points). The requirement of the iteration is to find q_1, where equation 6.17 is true. This can be achieved using the bisection method, using q_1 as the parameter and Equation 6.17 as the equation to solve.

The only constant not quantified so far is Θ_0, which is the the asymptote of the temperature distribution function. This constant has to be set very carefully as if its value is set too low then the estimated temperature of the hotspot will be lower than its actual temperature. However it is certain that the value of Θ_0 has to be lower than the coldest point within the test piece, because it denotes the asymptote of the temperature distribution curve - therefore the value of Θ_0 is set to be equal to the surface temperature, as it is the lowest known temperature within the material, and so it is certain that the temperature of the hotspot will be over-estimated. (In case of degradation monitoring over-estimation of the defect is more desirable than underestimation because of safety reasons.) Onceq_1 and q_0 are obtained the temperature distribution based on the Assumed Distribution method can be reconstructed.

6.5 Reconstruction of simulated data

In order to evaluate the implementations of the reconstruction methods described in Section 6.4 they are compared using simulated temperature distributions so that the effect of noise can be eliminated - for this purpose a simulated temperature distribution map has been created. The simulation was based on a two-dimensional steady state conduction model described in [60]. All boundaries were set to be convective. The temperature constant was chosen to be $\Theta_0 = 51$ °C and the heat convection constant (describing the heat transfer between the sample and air during cooling) to be $h = 1\frac{\mathrm{W}}{\mathrm{m}^2\mathrm{K}}$. The resulting temperature distribution is shown in Figure 6.5.a.

The constants determined by the calibration in Section 6.3.1 were used to convert the temperature map into velocities and therefore their relationship is linear. The

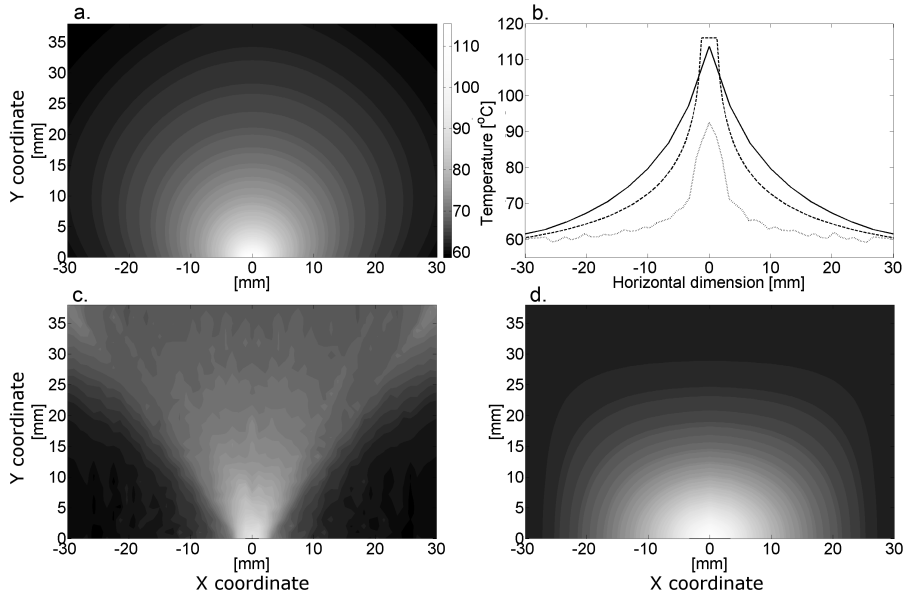

Figure 6.5: Reconstructed temperature distribution estimated from times of flights calculated from a simulated temperature distribution shown in Figure a. using the Randomized Kaczmarz algorithm shown in Figure c. and the Assumed Distribution method shown in Figure d. All of these images are displayed on identical color-scales as shown. (The array of sensors is located along the top edge of the image). For better numerical comparability Figure b. shows the horizontal temperature distribution at $y = 0$ mm - the continuous line shows the actual simulated temperature on the backwall, the dashed line shows the temperature distribution reconstructed by the Assumed Distribution method and the grey dotted line shows the distribution reconstructed by the Kaczmarz method

time of flight values and velocities were computed analytically without simulating ultrasonic waveforms. The locations of the wavepaths relative to this velocity map were determined in the following way: the endpoint coordinates of the wavepaths were calculated based on the known attachment point coordinates of each waveguide. In order to calculate the times of flight along each wavepath the value of the velocity map were evaluated along each wavepath using linear interpolation. For the linear interpolation, both the surface wavepath and backwall echo wavepath were sectioned with a spacing of dS = 0.001 mm resulting in n and m number of sections accordingly. Therefore the time of flight for each wavepath was:

$$t_{ij}^{surface} = \sum_{h=1}^{n} \frac{1}{c_h} dS \tag{6.18}$$

$$t_{ij}^{backwall} = \sum_{h=1}^{m} \frac{1}{c_h} dS \tag{6.19}$$

where c_h is the interpolated velocity at the differential line element number h. It is acknowledged that this straight-ray model ignores a) refraction and b) diffraction, but these were considered negligible due to a) the low contrast and b) the smoothly varying nature of the velocity field.

Once the time of flight values have been calculated, the two presented reconstruction algorithms can be applied. The simulated field is shown in Figure 6.5.a. and the reconstructed images are shown in Figure 6.5.b. and 6.5.c. For better comparability the distribution along the backwall of the sample ($y = 0$ mm) is shown in Figure 6.5.d.

The results show that the Assumed Distribution method estimates the temperature of the hotspot to within $2 - 3$ °C and estimating the backwall temperature to within 5 °C elsewhere, while the Kaczmarz algorithm has an offset error of 20 °C.

6.6 Reconstruction from experimental data

6.6.1 Signal Processing

The ultrasonic sensor array, the cylindrical heating element and test piece assembly shown in Figure 6.2 were used to capture waveforms to also experimentally evaluate the methods described in this chapter. The signal acquisition for these measurements has to be very fast as the transient temperature distribution is continuously changing. For signal generation and data acquisition purposes an M2M MultiX LF fully parallel array controller (M2M S.A., Les Ulis, France) was used, which is able to capture the 380 waveforms in a fraction of a second. As an approximation to the ideal toneburst, a 5 cycle square wave was used as a transmitted signal. The repetition rate of the measurements was 0.5 kHz and each saved waveform was calculated as the average of 16 measured waveforms.

Cegla *i.e.* [24] describe the behaviour of the waveguides assuming an ideal sent toneburst and conclude that the signal to noise ratio of the sensor is about 30 dB, as the excitation of undesirable modes in the waveguide cannot be completely avoided. Since the noise caused by the undesirable modes is coherent it cannot be removed by averaging. Another limitation of the setup is the signal generator of the array controller. As the sent toneburst is approximated by a 5 cycle square wave, its frequency spectrum is expected to be less ideal, which results in unwanted frequency components in the signal. These phenomena can be observed in Figure 6.6 showing a sample waveform measured with the setup.

Three different toneburst packets are clearly identifiable in Figure 6.6 nevertheless - the arrival of the surface skimming wavepacket, first backwall echo and second backwall echo wavepacket. A lower frequency tail wave close to the surface skimming wave caused by the imperfect sent toneburst is present as well followed by coherent noise between wave packets, which is explained by the dispersion in the waveguides as previously described. These phenomena cannot be avoided using the current array controller, their effect can only be reduced by band-pass filtering. Ultimately however the filters cannot eliminate all of the unwanted components and so they contribute to what is handled as coherent noise in the waveforms. The time of flight

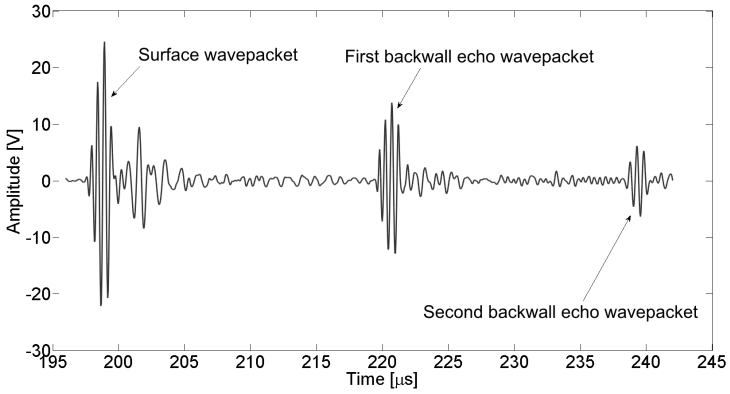

Figure 6.6: A sample waveform recorded at room temperature using the ultrasonic waveguiie transducer array. The arrival of the surface skimming wavepacket, first backwall echo and second backwall echo are clearly visible

data required for the reconstruction therefore is extracted from the necessarily noisy waveforms using signal processing tools described here.

6.6.2 Calculation of Times of Flight

The signal processing applied in this chapter is similar to the rest of the thesis, but is summarised here to clarify small differences. The fundamental frequency of the sent toneburst here is 2 MHz, therefore first a 5^{th} order band-pass Butterworth filter with cut-off frequencies at 1.2 MHz and 2.8 MHz is applied to the signal. Once the signal has been filtered, it is cross-correlated with an ideal noise-free toneburst. A toneburst is used here because its frequency spectrum is well defined and has been shown to work well with the waveguide transducers in previous sections. The peak times of the resulting cross-correlation function are then interpreted as the arrival times of each wave packet.

The goal of this chapter is to assess the spatial distribution of the propagation velocity within the material of the test piece; therefore the time of flight of the backwall echo wavepackets has to be obtained with as high accuracy as possible. For this purpose the first backwall echo wavepacket is considered. The measured peak times of this wavepacket however also include the time needed to propagate through the waveguides - this term needs to be subtracted in order to obtain the time of flights within the material of the test piece only.

For this purpose the arrival time of the surface skimming wavepacket is subtracted from the arrival time of the first backwall echo and this difference is used as an input for the reconstruction. This formulation of the problem eliminates the time of flights within the waveguides, but requires additional assumptions to be made about the sensor assembly.

$$t_{ij}^{SBW} = t_{ij}^{backwall} - t_{ij}^{surface} \tag{6.20}$$

where $t_{ij}^{surface}$ is the measured arrival time of the surface skimming wavepacket from waveguide i to j and t_{ij}^{SBW} is the time difference of the first backwall echo wavepacket and the surface wavepacket between waveguides i and j. In order to calculate the average propagating velocity over the backwall echo path based on t_{ij}^{SBW} it is necessary to obtain the propagation velocity of the surface skimming wavepackets.

In the case of isotropic and homogeneous propagation velocity distribution (and so homogeneous temperature distribution) the average velocities of the surface wavepacket and the backwall echo wavepacket are equal, therefore the calibration measurements can be carried out problem-free.

Common degradation mechanisms do not affect the surface wavepacket, therefore the velocity of the surface wavepacket is straightforward to track, as it is only influenced by the surface temperature, which can be measured externally (*e.g.*: using thermocouples). In the case of simulated heat distributions the temperature of the surface was within ± 1.5 °C, therefore all the surface velocities are assumed to have the same propagation velocity. The calculation of this velocity is carried out using the following equation:

$$\widehat{c}_{surface} = \mathrm{MED}\left(\frac{d_{jk}}{t_{ij}^{surface} - t_{ik}^{surface}}\right) \tag{6.21}$$

where MED means that the median of the indicated data set is extracted and d_{jk} is the separation of waveguides j and k. As the calculation involves 380 waveforms per measurement the median of the dataset is used as opposed to averaging in order to prevent the noisier outlier waveforms to impair the precision of the calculation.

The obtained median surface velocity can now be used to calculate the average

propagation velocity along each backwall echo wavepath

$$c_{ij}^{S} = \frac{2\sqrt{\frac{d_{ij}^2}{4} + T^2}}{t_{ij}^{SBW} + \frac{d_{ij}}{\widehat{c}_{surface}}} \tag{6.22}$$

where c_{ij}^{S} denotes the calculated average propagation velocity over the backwall echo path from waveguide i to j.

In order to further decrease variability caused by the differences in each waveguide, the calculated high temperature propagation velocities are corrected based on the ambient propagation velocities.

$$c_{ij}^{S,corr} = c_{ij}^{S} - c_{ij}^{S,ambient} + \overline{c}_{ij}^{S,ambient} \tag{6.23}$$

where $c_{ij}^{S,ambient}$ denotes the backwall velocities evaluated using t_{ij}^{SBW} at room temperature and $\overline{c}_{ij}^{S,ambient}$ is the arithmetic mean of all $c_{ij}^{S,ambient}$ values. This correction is based on the reasonable assumption that the average velocity measured at room temperature is precise and the variations come from the specific waveguide combinations (*e.g.*: coupling conditions, waveguide imperfections, differences in the piezoelectric elements, and so on).

The benefit of extracting the time of flights of the backwall echo wavepackets using the surface wavepacket is not immediately obvious, since a much more straightforward approach exists. The alternative would be to use pulse-echo waves (waveforms produced by sending and receiving with the same waveguide), which would allow to extract the time of flights within the waveguides directly, and subtract this value from $t_{ij}^{backwall}$ in order to calculate the time of flights of the backwall echo wavepackets. Indeed, pulse-echo waves are recorded as part of a full matrix capture, however it is practically impossible to carry out pulse-echo measurements on both the sending and receiving waveguide at the same time as the actual pitch-catch measurement takes place, which means that the temperature of the sample and the waveguides will have changed between measurements. In comparison the arrival of the surface wavepacket can be extracted from the very same waveform as the backwall echo wavepacket, it is certain therefore that all of the waveguide-related variabilities are cancelled out and so the surface wavepacket arrival times were chosen as reference for the signal

processing.

6.6.3 Experimental Measurements

The reconstruction of the experimental measurements described in this section are expected to differ from the simulated results due to noise, that experimental measurements introduce into the dataset. A measurement was carried out to evaluate the variability introduced by the experimental setup and the processing methods in use.

In order to evaluate the variability of the sensor assembly, measurements were carried out at room temperature. Altogether 60 datasets were acquired 12 seconds apart resulting in $60 \cdot 380 = 22800$ waveforms in 12 minutes. The results are shown in Figure 6.7. The maximum of the calculated standard deviation map is 0.23 m/s, which is 0.007% of the propagation velocity (while sending with waveguide number 19 and receiving with number 15 as shown in Figure 6.7). Based on the calibrated temperature-propagation velocity relation this yields a variability of 0.45 °C over the wavepath for this specific waveguide combination, which is the worst case scenario.

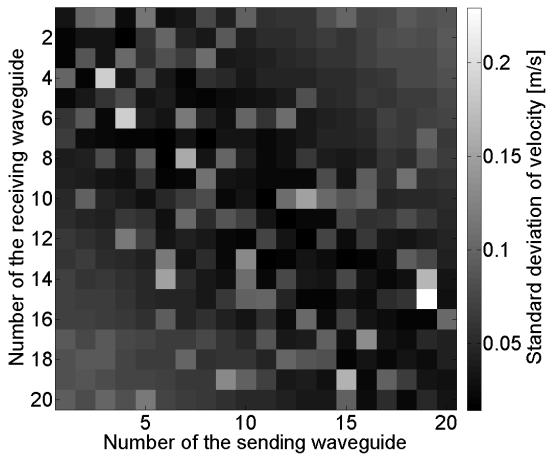

Figure 6.7: Standard deviation of the propagation velocities calculated for each waveguide pair measured at room temperature

6.6.4 Evaluation of Reconstruction Methods with Experimental Measurement Data

In the case of experimental measurements the exact temperature distribution within the test piece is unknown. The temperature of the test piece therefore was monitored using 5 thermocouples while heating the assembly. These were attached by welding in the locations shown in Figure 6.1.

The measurements carried out with the assembly were evaluated using the Randomized Kaczmarz algorithm and the Assumed Distribution method defined in Section 6.4.2 and were compared to the measurements carried out with the thermocouples.

Sixty datasets were acquired while the test piece was being heated. The reconstructed images at the highest temperatures are shown in Figures 6.8.a., 6.8.b. In order to demonstrate the importance of the position of the heat source a second measurement was carried out with the heating element repositioned by 10 mm. The reconstructed images from the measurements carried out with the repositioned heat source are shown in Figures 6.9.a., 6.9.b. (shown at the highest measured temperature).

The figures described above account for the static snapshots at a given time. The evolution of temperatures in time for the centred and repositioned case are shown in Figures 6.10.a., 6.10.b. These figures show the temperature of the hotspot measured by the thermocouples and reconstructed with the algorithms described in this chapter for all the 60 datasets that have been acquired.

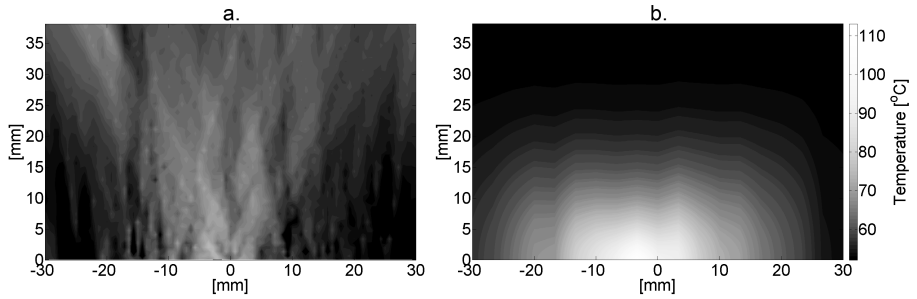

Figure 6.8: Reconstructed temperature distribution estimated from times of flights calculated from an experimental measurement with heating element at location $y = 0$, $x = 0$ mm using the Randomized Kaczmarz algorithm (a.) and using the Assumed Distribution method (b.) 591 seconds after start of heating

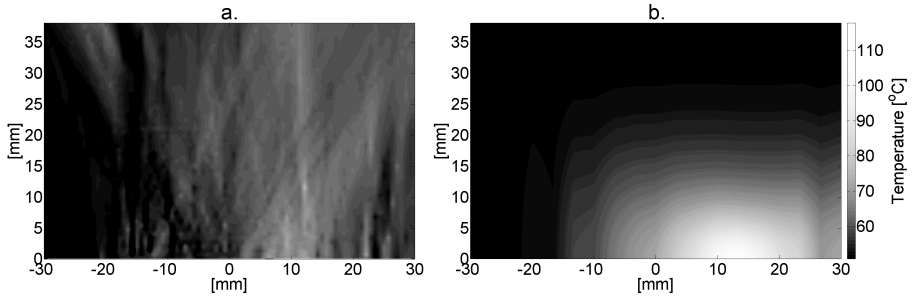

Figure 6.9: Reconstructed temperature distribution estimated from times of flights calculated from a measurement using the Randomized Kaczmarz algorithm (a.) and using the Assumed Distribution method (b.) after repositioning the cylindrical heating element to $y = 0$, $x = 10$ mm. The measurement was carried out 590 seconds after start of heating.

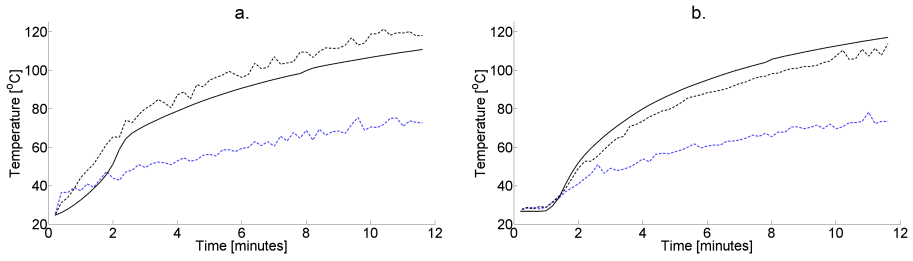

Figure 6.10: Evolution of the temperature at the hottest point of the material evaluated with different methods. The continuous line shows temperature measurements carried out using the thermocouples, the black dashed line shows the results of the Assumed Distribution method and the blue dashed line shows results of the Kaczmarz method. Image a. shows the measurement where the heating element is attached in the middle of the sample, while image b. shows the measurements where the heating element is attached at an offset of 10 [mm] from the middle of the array.

6.6.5 Discussion

It is clear that the Assumed Distribution method presented in Section 6.4.2 provides a more accurate reconstruction in the case of simulated data compared to the Kaczmarz algorithm. In simulations, the Assumed Distribution method estimates the temperature of the hotspot to within $2-3$ °C, while the Kaczmarz algorithm provides a less accurate estimation (the reconstructed hotspot had a 20 °C offset error).

The reconstructed images based on measured data are similar, however the inconsistent noisy data causes the Kaczmarz algorithm to perform even less accurately compared to the simulated case. It still provides a very rough estimate of the propagation velocity distribution within the material and so in this case the Kaczmarz algorithm is able to estimate the temperature of the hotspot with an accuracy of the order of ± 30 °C. The estimation accuracy of the Assumed Distribution method however is of the order of ± 5 °C, therefore outperforming the Kaczmarz algorithm. As shown in Figures 6.10 a. and b. the relative error of each method stays consistent while increasing the temperature of the hotspot.

The figures reconstructed by the Kaczmarz algorithm indicate that the primary source of variability is the lack of vertical resolution, which is caused by the limited field of view of the ultrasonic sensor array. This geometrical limitation however cannot be overcome by simply extending the array as the longer the waves propagate within the material the more attenuated they are, which in turn increases the variability of the extracted time of flight data (due to loss of signal to noise ratio).

In comparison to this shortcoming of the Kaczmarz algorithm the preliminary assumption of straight wavepaths introduces negligible errors, which was one of the initial concerns associated with this algorithm. This is because the biggest ultrasonic velocity change is of the order of 2% (which is equivalent to a void fraction of about 3.5% based on the Chatterjee model), therefore the error introduced by ignoring ray-bending is insignificant compared to the limitations of the geometry.

The Assumed Distribution method circumvents the problem of deducing vertical resolution from noisy data by assuming the vertical temperature distribution and

therefore ultrasonic velocity distribution. This approach has been shown to be more effective, however the assumptions made are specific to the phenomenon of diffusion, that can be described by an exponential decay from the source. This is a good model for heat transfer and diffusion of heat into the component. Hydrogen attack is dependent on diffusion of hydrogen into the steel and the Assumed Distribution Method therefore is also a likely candidate for describing the estimate of damage due to reaction of the diffused hydrogen with the carbon in the steel, provided it is linearly related to the amount of hydrogen. This distribution is not explicitly investigated in the literature, and the discussion of hydrogen attack in [87], [100], [101] only imply the effect of a step function in the damage. Based on governing rate equations and physical origins however there are strong analogies between heat transfer by conduction and mass transfer by diffusion [102], therefore the assumptions required for hydrogen attack are likely to be similar to the ones in this study.

In addition to these findings, it should be noted that a significant difference between temperature distribution and material degradation produced ultrasonic velocity change is the arrival time of the surface wavepacket. The measurements presented in this section involved creating a large temperature gradient within the specimen by applying heat, which is transferred quickly within the material to the surfaces, and so the extraction of the arrival time of the surface wavepacket required additional assumptions to be made. In the case of material degradation however the surface wavepacket should not be affected, therefore the arrival times can potentially be extracted more precisely.

6.7 Hydrogen Attack Experiments

6.7.1 Description of rig

Since the feasibility study using heat has shown that ultrasonic monitoring has the capability of monitoring changes that are expected from hydrogen attack, it is clear that implementing a hydrogen attack induction rig is worthwhile. As described in the previous section, hydrogen attack is caused by high partial pressure hydrogen diffusing into steel at high temperatures. The most straightforward approach to

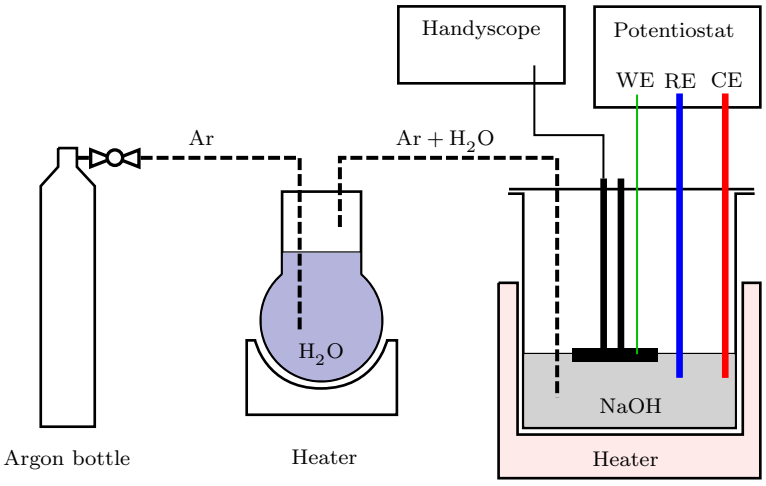

Figure 6.11: Figure shows the diagram of the molten salt hydrogen attack rig. This figure was produced based on [83].

induce hydrogen attack in the laboratory is by recreating a similar environment by means of a high temperature pressure vessel [103]. It is however very difficult to construct a rig which would allow only one side of the sample to be exposed, thus allowing ultrasonic measurements to be captured on the opposite side. Hence, an alternative electrolysis based approach is considered in this section based largely on the research of Tsubakino *i.e.* [83].

A diagram showing the principle of operation of the selected molten salt hydrogen attack rig is shown in Figure 6.11. Measurements on this rig can be carried out by heating NaOH in an inert container to 400 °C, which is significantly above its melting point of 318 °C [104]. Once the NaOH melts, a Pt-coated MgO stabilised zirconia reference electrode and a graphite counter electrode are inserted into the now liquid electrolyte all sourced from Sigma-Aldrich Company Ltd., Gillingham, UK. These electrodes are used as suggested by [83].

Meanwhile, water is heated up to 80 °C in a separate vessel. Once both solutions have reached the desired temperatures, argon gas is bubbled through the water in order to carry water vapour into the molten NaOH at a flow rate of $2 \cdot 10^{-6}$ m^3/s. Once a current is applied to the working electrode (the sample) that is immersed partially in the molten salt, the electrolysis of water results on hydrogen evolution on the surface of the sample.

Tsubakino evaluated the efficiency of this setup by current density as a function of

applied overpotential, which is a good indicator of the rate at which reactions occur at the interface of the working electrode. Tsubakino concluded that the applied current resulted in the evolution of hydrogen on the sample surface. The expected void fraction caused by hydrogen attack however was not quantified. Although SEM snapshots of the charged samples were presented, no control images were shown, and therefore it is not possible to estimate the volume fraction of the created voids. It further questions the quantitative relevance of the figures included in the report of Tsubakino that the surfaces shown are photographs of unpolished fractured surfaces. It is thought that such a fracture would preferentially occur in the material where the density of imperfections of any kind is highest. Hence, no good reference was found with regards to the expected void fraction caused by electrochemically induced hydrogen attack. Instead, the approach chosen in this thesis is to compare SEM figures of samples before and after inducing hydrogen attack in order to evaluate the whether hydrogen attack was induced on the sample.

6.7.2 Experimental Results

This molten salt based hydrogen attack induction rig was built. Figure 6.12 shows the results of a 5 hour measurement using the rig, during which an ultrasonic sensor was permanently installed on a sample immersed partly in the molten salt. The most interesting feature of the measured dataset is the relative ultrasonic propagation velocity shown in Figure 6.12.b., as it is expected to correlate with the induced hydrogen attack. In addition to the measured values, two horizontal lines are also shown to help visually interpret the variability of the measured values. These horizontal lines represent the propagation velocity change that would be expected from 1% void fraction hydrogen attack on 10% of the wall thickness.

As can be seen from the figure, the variability of ultrasonic measurements is too high to be able to measure changes of the order of 1% void fraction accurately. With such high variability it was not possible to measure changes once a forced current was applied to the sample represented by a vertical red line on the figure. The reason for the low precision is simply the continuous loss of signal amplitude as shown in Figure 6.12.c. Subsequent repetitions of the experiment confirmed that the ultrasonic signal amplitude rapidly degrades when the sample is inside the molten salt container. It

was found that the signal amplitude drop is caused by corrosion of the waveguide sensor contact patch. When the rig was disassembled, a small amount of NaOH was observed on the top surface of the sample even when the sample was not fully immersed in the molten salt.

Since the ultrasonic measurements were inconclusive, SEM photographs of the sample were evaluated before and after the hydrogen attack experiment. These images are shown in Figure 6.13. In both cases, the sample was polished using a grit size of 800. Although small voids can be observed on the hydrogen attack charged sample shown in Figure 6.13.b, the number of such voids is not conclusively higher than that of a control sample shown in Figure 6.13.a.

It was not possible therefore to confirm that inducing hydrogen attack was successful. In the future, it may be possible to improve the rig design to better protect the

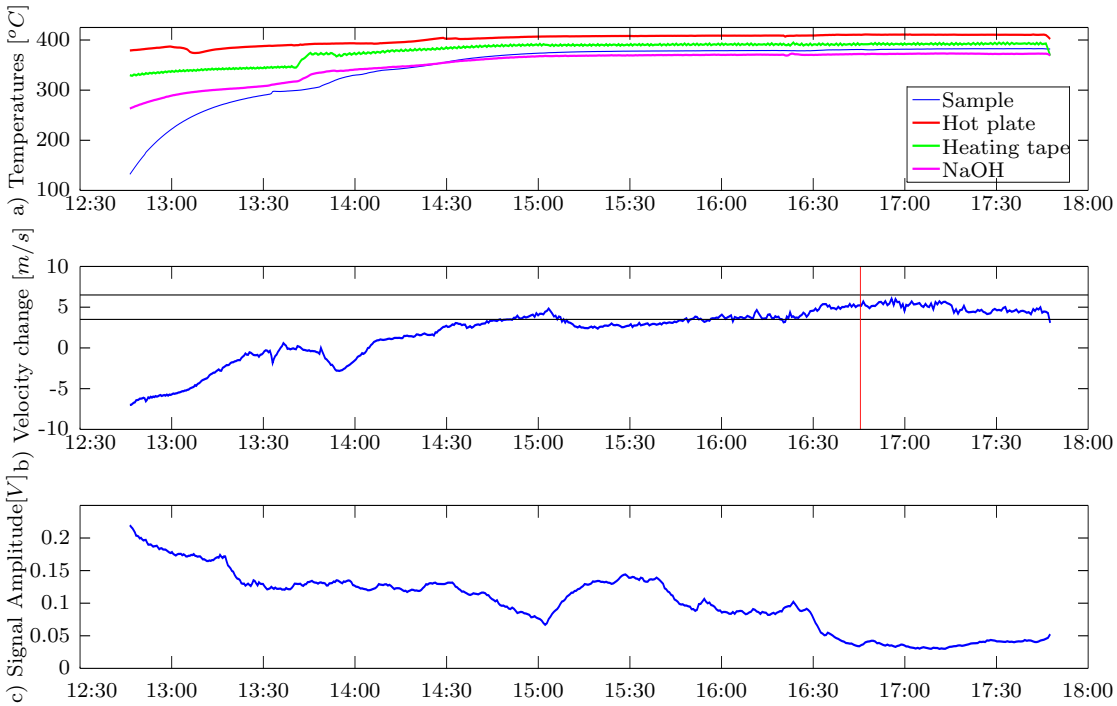

Figure 6.12: Figure a) shows the temperature of the sample (blue line), the hotplate used for heating (red line) and the measured temperature of the NaOH (magenta line). Figure b) shows the relative ultrasonic propagation velocity changes (blue line) and when current was applied to the sample (red vertical line). For reference, Figure b) also shows the amount of relative velocity change that would be introduced by 1% void fraction of hydrogen attack over 10% of the material thickness with horizontal black lines. Figure c) shows the maximum amplitude of the measured ultrasonic signal.

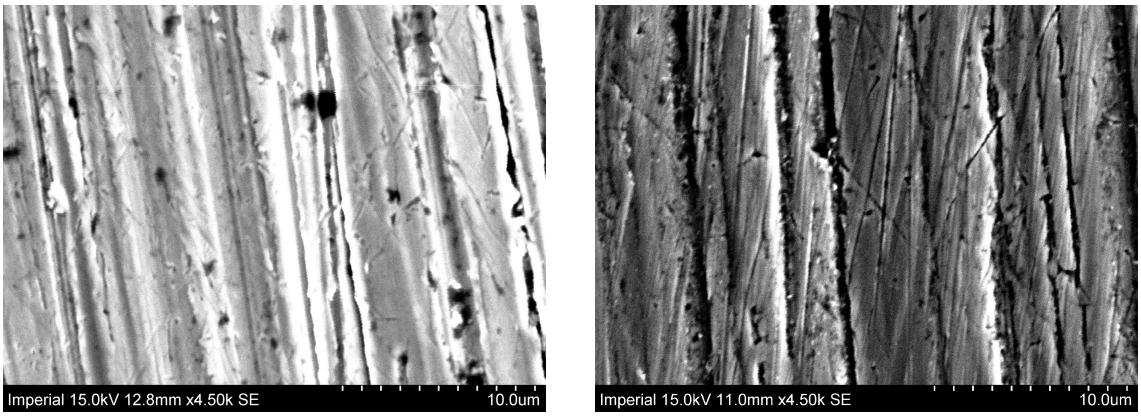

a) b)

Figure 6.13: Figure a) shows an SEM photograph of a mild steel sample before the experiment. Figure b) shows an SEM photograph of the same sample after the experiment. In both cases the sample was polished to 800 grit.

ultrasonic sensors from corrosion. This would improve the precision of ultrasonic measurements, as the signal amplitude would not be expected to decrease over time. It would also allow the experiment to be extended for longer periods of time, since the degradation of the signals would no longer be a limiting factor. Higher degrees of material degradation would therefore be possible to induce, which would be easier to verify using both ultrasonic methods and SEM images. Improving the molten salt rig was not attempted however due to time limitations, but may be interesting future work.

6.8 Summary

This chapter investigated the feasibility of using permanently installed ultrasonic sensors for monitoring high temperature hydrogen attack. A non-uniform ultrasonic velocity distribution, which is expected to be the effect of hydrogen attack and similar degradation mechanisms, was created by applying heat to the specimen. This temperature map was used to evaluate the feasibility of reconstructing the propagation velocity map within the material. The temperature range investigated in this study ($20 - 110$ °C) is equivalent to a void fraction of $0 - 3.5\%$ of hydrogen attack.

Based on the simulated and experimental results, the equipment and methods used

are precise enough to measure local temperature changes of the order of ±30 °C using the Kaczmarz (ART) algorithm and ±5 °C using the Assumed Distribution method presented here with a resolution of 1.5 pixels per millimetre equivalent to ∼ 0.7 mm per pixel (which is half the wavelength of the signal within the material). These values are equivalent to a local ultrasonic propagation velocity change of $\pm 15 \frac{\mathrm{m}}{\mathrm{s}}$ and $\pm 2.5 \frac{\mathrm{m}}{\mathrm{s}}$ respectively, which is equivalent to a local void fraction of 0.9% and 0.15%. These initial results thus showed that the techniques may be useful to monitor the progress of hydrogen attack.

A molten salt rig using NaOH was therefore built to induce hydrogen attack in a mild steel sample. The results of measurements using the hydrogen attack rig however were inconclusive, as environment inside the molten salt container induced rapid corrosion on the contact patch of the waveguide transducers. Because of this, ultrasonic measurement results degraded quickly, and the experiment had to be stopped prematurely. It was not possible to verify experimentally that hydrogen attack can be monitored using the proposed permanently installed ultrasonic sensor. It was proposed for future work instead to design a new rig that would protect the contact patch side of the sample and would prevent any contact-side corrosion.

Chapter 7

Thickness Loss Measurements on Evolving Rough Surfaces

7.1 Introduction

As discussed in previous chapters, the potential repeatability of permanently installed ultrasonic thickness monitoring is below the micrometre level in laboratory conditions. In practice however, measurement conditions are not as stable or predictable, which may significantly increase variability of the thickness measurements. Most of the possible sources of error, namely variable coupling conditions, temperature changes and gradients as well as random noise in the signal have been discussed in previous chapters of this thesis. The most complex issue to characterise however is caused by shape changes of the internal pipe surface, or backwall surface, and is discussed in this chapter.

Uneven backwall geometries, or rough backwalls, cause distortion in the ultrasonic wavepacket that is reflected from them. The distortion of the backwall echo wavepacket is expected to cause errors in the arrival time estimation, and thus in the thickness measurement. This phenomenon has been investigated in 2D simulations by Jarvis *et al.* [11]. In the paper by Jarvis *et al.* individual backwall samples were generated as random Gaussian distributed surfaces. Correlation lengths of 0.4 mm(0.25λ); 0.8 mm(0.5λ); 1.6 mm(λ); 2.4 mm(2λ) and R_{RMS} ranges of 0.02

mm(0.01λ) to 0.3 mm(0.19λ) with increments of 0.02 mm(0.01λ) were generated, where λ is the wavelength of the ultrasonic signal. Ultrasonic signals were then simulated for the generated geometries. Three standard signal processing methods (Cross-Correlation, Peak-to-Peak and First Arrival) were used to calculate thicknesses from the signals. The study evaluated the distribution of the calculated thicknesses and concluded that the error of mean wall thickness estimates may be as large as millimetres regardless of the applied signal processing methods. Although these simulations were carried out in 2D, in later studies Jarvis confirmed that 2D simulations capture the majority of physical interactions occurring during reflection compared to the 3D case [38, 105]. This is a valuable finding, since 3D simulations are computationally very expensive. This chapter is concerned with carrying out statistical simulations of the evolution of the backwall surface shape and therefore focuses on 2D simulations to keep simulation times feasible.

The results that were produced by Jarvis *et al.* are not directly applicable to extract the errors in thickness and wall loss where there is a continuously changing surface such as in corrosion/erosion. This is because the randomly generated successive backwall surface geometries were independent. When monitoring the process of corrosion with permanently installed sensors and when measurements are carried out frequently, the geometry is expected to change only gradually between measurements. The effect of gradual geometry change on the accuracy of mean wall thickness loss trend estimation has not yet been evaluated, and this is therefore discussed in this chapter.

It is important to note the complexity of the gradual wall thickness loss problem. In this thesis two types of wall thickness loss are distinguished: localised (tending towards pitting-type) thickness loss and statistically uniform thickness loss. Examples of these cases are shown in Figure 7.1. This figure shows the two alternative wall thickness loss mechanisms by superposing various stages of gradual shape change. In both of these mechanisms some amount of mean wall thickness is lost, and both may be affected by a degree of roughness or backwall surface shape change. The key difference between these cases is that with a localised (pitting-type) thickness loss phenomenon, not all of the backwall surface is affected and there are local areas, pits, at which metal is preferentially lost. The limiting scenario of this is an

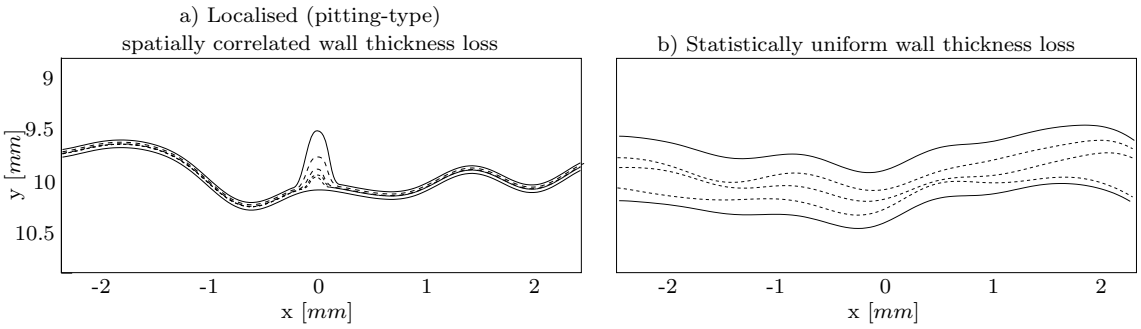

Figure 7.1: Two alternative wall thickness loss mechanisms. On both graphs the initial and final backwall shape is shown with solid black lines whereas steps of wall loss between these stages are shown with dashed black lines. a) shows a pitting-type localised thickness loss mechanism. b) shows a statistically uniform thickness loss mechanism. Both processes start with a moderately rough backwall.

isolated pit drilling through the whole wall thickness. The changes in the backwall are spatially correlated and therefore this phenomenon will also be referred to as spatially correlated thickness loss. In order to assess the integrity of such a structure one would then be interested in finding the location of the pit and monitoring its deepest point, *i.e.* monitoring the extent of the defect. In contrast, for a statistically uniform thickness loss phenomenon all areas of the backwall surface have the same probability of getting thinner and thickness loss is spatially uncorrelated. Here, it is the mean wall thickness loss that is of importance, as it is the most suitable parameter to describe the pipe wall thickness and pipe strength. Nonetheless, backwall surface geometry changes affect the estimated mean wall thickness loss.

This chapter aims to estimate the accuracy of ultrasonically monitored wall thickness loss rates under varying backwall morphology conditions. First, a backwall geometry model to generate sequences of backwalls with various amounts of gradual shape change is introduced. Following this, the approach of simulating ultrasonic signals for the generated backwall geometries is explained. Standard arrival time estimation methods (Peak-to-Peak, First Arrival and Cross-Correlation) are then introduced. Since previous studies by Jarvis *et al.* [11, 38, 105] have shown that standard arrival time estimation methods are sensitive to the effects of backwall roughness, a new improved arrival time estimation method - Adaptive Cross-Correlation (AXC) - is introduced. Both the standard and the newly proposed AXC methods are then used to process the simulated signals. The accuracy and precision of the wall loss rates as estimated by the different algorithms is then compared. This is followed by

concluding remarks.

7.2 Background of Study

7.2.1 Backwall geometry evolution simulation

It is well established that a number of corrosion and erosion processes may cause non-uniform wall thickness loss in pipes [1, 2, 5, 106, 107]. Since the impedance mismatch is very large between a typical steel pipewall and the contained medium (regardless if it is gas or fluid), it is a very good approximation to consider that the interaction of the ultrasonic wave and the backwall surface is a function of the backwall geometry only. A backwall generator model is therefore proposed based on the geometrical parameters of the surface only. This uncouples the ultrasonic simulations from the underlying corrosion/erosion process shaping the backwall, and instead allows to focus on the investigation of backwall parameters that affect the ultrasonic signal the most. It is beyond the scope of this thesis to develop a comprehensive model that links the corrosion parameters (temperature, pressure, chemical composition, flow rates, etc.) to a particular backwall shape. However, the statistical parameters of the modelled surfaces were based on profilometer scans from retired pipework to make sure that they were close to real life examples of corrosion [108]. For example a measurement of a retired sample that had been exposed to high temperature sulfidation corrosion yielded a surface RMS value in the range of 0.1-0.4 mm and correlation length in the range of 1-10 mm.

The model of backwall evolution that was created, initially describes a random Gaussian distributed backwall surface with a correlation length of CL_i and a profile height of $R_{RMS} = r_i$ similarly to [11]. This initial backwall sample is expressed as an array of points $BW_1(x)$. The mean value of $BW_1(x)$ is equivalent to the initial mean wall thickness and is chosen to be $T_1 = 10$ mm. Subsequent backwall samples $BW_{2..50}(x)$ are generated by adding a perturbation term to the previous backwall geometry. This perturbation term $P_n(x)$ is also generated as a random Gaussian distributed backwall surface. $P_n(x)$ is characterised by the following parameters: $CL_p = CL_i$ and $R_{RMS} = r_p < r_i$. The mean value of $P_n(x)$ is zero, meaning that

the perturbation term does not cause mean wall thickness loss.

The initially generated $BW_1(x)$ backwall surface is perturbed 49 times $P_{1-49}(x)$ resulting in altogether 50 backwall surfaces $BW_{1..50}(x)$. These 50 related backwall surface geometries $BW_{1..50}(x)$ are referred to as a backwall sequence. Each perturbation step of this backwall generator model therefore is calculated the following way:

$$BW_{n+1}(x) = (BW_n(x) - T_n + P_n(x)) \cdot s + T_{n+1} \tag{7.1}$$

$$T_{n+1} = T_n - \Delta T \tag{7.2}$$

where $BW_{n+1}(x)$ is the $(n+1)^{th}$ backwall geometry, $BW_n(x)$ is the n^{th} backwall geometry, T_n is the mean wall thickness of the n^{th} backwall, ΔT is the mean wall thickness lost at each perturbation step and s is the R_{RMS} scaling factor. The R_{RMS} scaling factor s was introduced in order to control the R_{RMS} profile height of the generated surfaces. In the initial simulations it is used to ensure that the sequence of 50 backwalls are of the same R_{RMS}, as without the scaling, perturbing the geometry multiple times would result in unintended R_{RMS} increase. In order to keep R_{RMS} constant, the following value is used for s:

$$s = \frac{r_i}{\sqrt{r_i^2 + r_p^2}} = \frac{1}{\sqrt{1 + \left(\frac{r_p}{r_i}\right)^2}} \tag{7.3}$$

This equation was derived based on normalising the sum of two independent variances. In addition to keeping the R_{RMS} constant, the R_{RMS} scaling factor can also be used to gradually scale backwall geometries to either increase or decrease their profile height. As opposed to the behaviour of $P_{1..49}(x)$, where the perturbation term is randomly generated at each step, this allows us to introduce a form of spatially correlated perturbation into the model, since continuously scaling the backwall will be spatially correlated between steps. For the rest of this thesis the term "correlated backwall change" refers to a perturbation of the backwall that is not spatially random and to some extent dependent on the existing backwall shape; *e.g.* thinner parts will preferentially thin and thicker parts will preferentially stay thick (this is essentially what happens in pitting).

In this backwall generation model ΔT represents the mean wall thickness loss per step, this is therefore the parameter the ultrasonic sensor is aiming to detect. ΔT however is not an independent variable. In a real scenario a backwall surface is unlikely to grow at any location, therefore when a backwall is perturbed, that perturbation must be linked to some amount of mean wall loss. In this model ΔT was chosen to be equal to r_p. Since r_p is the standard deviation of the random perturbation profile, this may still result in temporary thickness increase at a given step, but will result in average net thickness loss over all points for the full backwall sequence. This approach therefore maximises perturbation for a given amount of wall loss in order to investigate the maximum amount of uncertainty in ultrasonic thickness loss measurements as a function of mean wall thickness loss.

This model can then be used to generate backwall sequences, so that they can be used for ultrasonic signal simulations. The DPSM method introduced in Chapter 2 was used to simulate signals for the permanently installed ultrasonic waveguide sensor. 100 active point sources were used to model the transmitter transducer. These point sources were distributed with a separation of 10 µm and were offset from the transducer/sample interface by 5 µm. The backwall surface was represented by 1200 passive point sources with a separation of 50 µm offset from the surface by 25 µm altogether spanning the width of the 60 mm backwall surface. These parameters correspond to those proposed by Jarvis [105]. The receiver transducer was simulated by a single receiver point at the centre of the coupled transducer. A sketch of the complete setup is shown in Figure 7.2 along with the simulated signal for that setup.

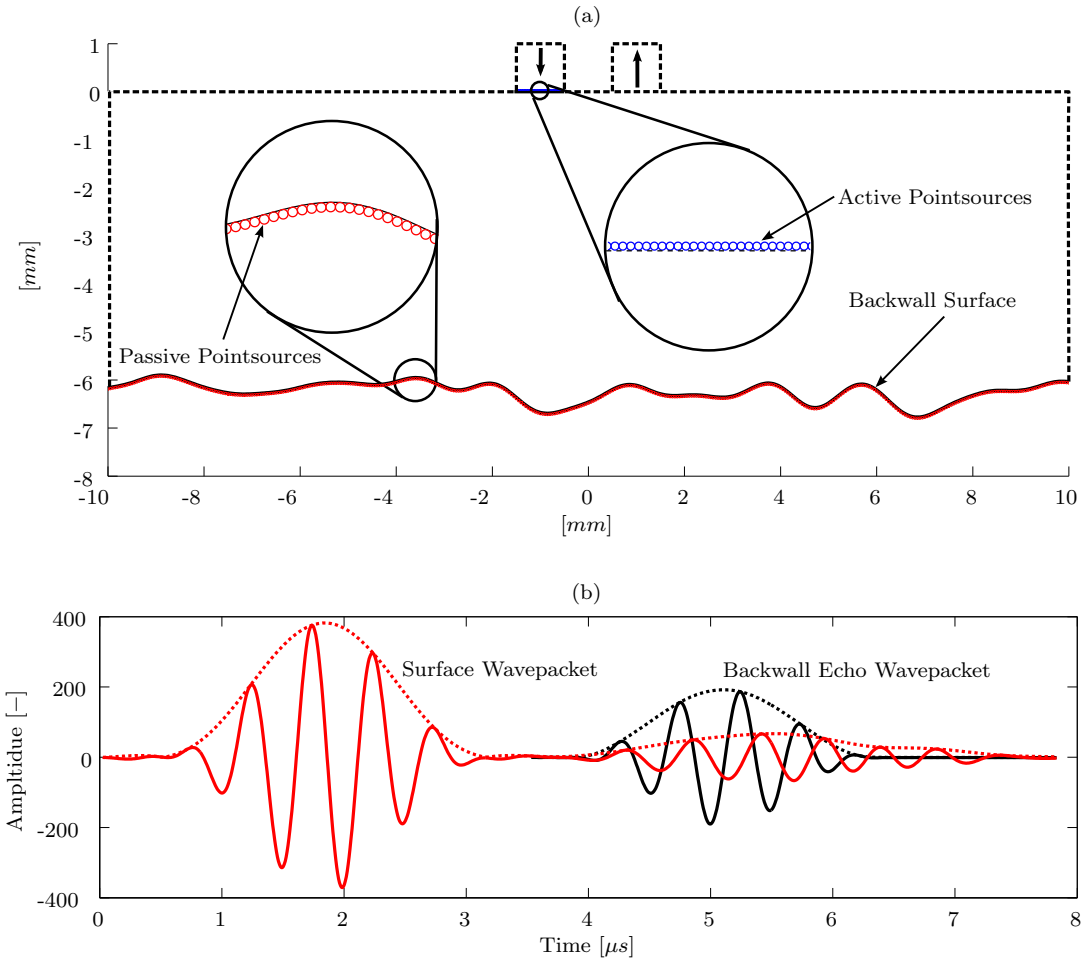

Figure 7.2: a) shows the geometry of the DPSM model of a generated backwall sample. Blue circles are the active point sources simulating the transmitter transducer. Red circles are passive point sources simulating the backwall geometry. In the DPSM simulations 60 mm wide patches are simulated, but a smaller section is shown on this figure for better visibility. Continuous black lines are drawn where a zero pressure boundary condition has been applied. Dashed lines are purely for visual purposes only and therefore no boundary condition was applied on them. b) shows the simulated signal based on the model in red. The signal for a flat backwall of equivalent mean wall thickness is shown in black. The Hilbert envelope for both signals are shown with respective colours using dashed lines. The first wavepackets in both signals (Surface Wavepacket) are undistorted and therefore overlap on the figure. The second wavepacket (Backwall Echo Wavepacket) of the rough backwall sample is distorted due to backwall roughness.

7.2.2 Arrival time extraction

Once the ultrasonic signal is simulated for a given backwall geometry, the arrival times of all wavepackets in that signal can be determined. As explained in Chapter 3 there are a number of signal processing methods commonly used for this purpose.

In this study the Peak-to-Peak (P2P), Cross-correlation (XC) and First Arrival (FA) have been implemented. These methods are commonly used because they are simple to implement and relatively robust. Their behaviour has been investigated under relevant conditions to this thesis by Jarvis *et al.* [11]. The study by Jarvis *et al.* proposed to compare the performance of the P2P, XC and FA algorithms on randomly generated independent rough backwall surfaces. Its conclusion was that even under moderately rough surface conditions ($R_{RMS} \sim 0.1\lambda \sim 0.15$ mm) the variability of the ultrasonically estimated mean wall thickness values was as large as a millimetre. Although this study did not investigate the effects of gradual surface geometry change, its results suggest that common methods are likely to be sensitive to the ultrasonic distortion effect of rough surfaces.

Since standard methods are expected to be sensitive to signal distortion, they are not expected to perform adequately for gradually changing rough backwall surfaces. A new method - Adaptive Cross-Correlation (AXC) - is therefore proposed here. AXC was developed specifically for the purpose of accurately estimating the mean wall thickness loss rate of gradually changing backwall surfaces. This method is based on the standard cross-correlation algorithm, however it uses an alternative reference signal with which to cross-correlate. This is because the synthesised toneburst used in standard cross-correlation is not a good model for distorted backwall echo signals. Instead, AXC uses the following protocol to determine the arrival times of all 50 waveforms ($w_{1..50}$) in a backwall sequence simulation:

$$t_1^{SW} \overset{1}{\leftarrow} xcorr(w_1, S^{tb}) \tag{7.4}$$

$$t_1^{BW} \overset{2}{\leftarrow} xcorr(w_1, S^{tb}) \tag{7.5}$$

$$S_{n-1}^{BW} = w_{n-1}(t_{n-1}^{BW} : t_{n-1}^{BW} + t_{length}^{BW}) \qquad \text{with } n = 2..50 \tag{7.6}$$

$$t_n^{SW} \overset{1}{\leftarrow} xcorr(w_n, S^{tb}) \qquad \text{with } n = 2..50 \tag{7.7}$$

$$t_n^{BW} \overset{2}{\leftarrow} xcorr(w_n, S_{n-1}^{BW}) \qquad \text{with } n = 2..50 \tag{7.8}$$

where $xcorr(a, b)$ is the cross-correlation of functions a and b, $\overset{1}{\leftarrow}$ denotes the extraction of the time of the highest peak in the first wavepacket of a signal, $\overset{2}{\leftarrow}$ denotes the extraction of the time of the highest peak in the second wavepacket of a signal, w_n is the n^{th} waveform, $w(t_a : t_b)$ denotes windowing a waveform between times t_a and t_b, and S_n^{BW} is the windowed backwall wavepacket for the n$^{\text{th}}$ measurement. In summary

therefore AXC relies on the cross-correlation function to determine arrival times. The surface wavepacket and backwall echo wavepacket arrival times of the first waveform are determined similarly to standard cross-correlation. Standard cross-correlation is used also for all subsequent surface wavepackets. For all subsequent backwall echo wavepackets the backwall sample from the preceding waveform is used for cross-correlation. This allows AXC to adjust the reference signal for the backwall echo wavepacket as the geometry of the backwall changes, and the backwall echo wavepacket gets continuously distorted. Consequently, AXC is expected to provide more accurate mean wall thickness loss rate measurements.

Once the arrival times have been extracted using any of the signal processing methods, the thickness can be calculated. Since the geometry of the sensor setup is constant, the thickness can be calculated using the same equation as introduced in Chapter 2:

$$T = \frac{1}{2}\sqrt{c \cdot (t^{SW} - t^{BW}) \cdot (c \cdot (t^{SW} - t^{BW}) - 2 \cdot d)} \tag{7.9}$$

In order to evaluate this equation, the remaining two variables - propagation velocity (c) and separation between transducers (d) - also have to be defined. In the DPSM simulation the propagation velocity of the ultrasonic wave is constant at $3250\frac{\mathrm{m}}{\mathrm{s}}$. For the separation of transducers (d), the assumed value of .7 mm is used.

7.2.3 Simulation procedure

The aim of this chapter is to simulate a large number of gradually changing backwall sequences, and simulate ultrasonic signals that are reflected from these backwalls, so that they can then be evaluated using the presented signal processing methods. Comparing the mean wall thickness loss trends that are returned by the different signal processing methods allows us to compare their performance at tracking the mean wall loss for the simulated backwall morphology conditions. This section describes how the backwall generator model is set up to achieve this and how the results of the four signal processing methods are graphically summarised and compared.

The parameters of the backwall generator model that need to be set are CL, r_i, r_p

and s. First CL is considered. For Gaussian distributed surface profiles CL behaves essentially as a low-pass spatial frequency filter [105]. However as the correlation length is lowered and higher spatial frequency components are introduced, the density of point sources in the DPSM model has to be increased as well, in order to be able to accurately represent the behaviour of that surface. Lowering the correlation length therefore increases computational time, which is significant because of the high number of backwall simulations to be carried out. As Jarvis *et al.* [11] reported however, correlation length has a much lower impact on the signal than the R_{RMS} profile height. Also, once the correlation length becomes much smaller than the interrogating wavelength, the wave reflection becomes similar to that of a flat surface again but of the extremities of the the rough surfaces (thinnest parts). In our model CL was chosen to be 1 mm $\sim 0.6\lambda$ for all simulations, as the biggest changes in the signal are expected in the signal for this correlation length, therefore leading to conservative conclusions.

All of the remaining parameters for these simulations are shown in Table 7.1. As table 7.1 shows, the remaining parameters are broken down into two separate simulation sets. The first set of simulations is intended to create backwall surfaces with no R_{RMS} scaling (no change in RMS throughout the sequence of 50 backwall surfaces) for a range of initial R_{RMS} surfaces. 3 R_{RMS} values were chosen as $r_i = 100; 200; 300$ µm to be used, these are believed to be representative of values that can be experienced in real life plants. Perturbation values were chosen to be $r_p = 0; 5; 15; 30$ µm. In these simulations s was calculated according to Equation 7.3, so that the R_{RMS} does not change throughout a backwall sequence. This dataset therefore simulates spatially random wall thickness loss phenomena.

The second set of simulations is set up to create backwall surfaces with continuous R_{RMS} scaling (changing RMS value throughout the sequence of 50 backwall surfaces). In this set of simulations $r_p = 5, 15, 30$ µm cases are simulated. Selected r_i values are: 100 and 300 µm. Here the scaling coefficient was chosen so that it results in an R_{RMS} increase from 100 µm to 300 µm (where $r_i = 100$ µm) and an R_{RMS} decrease from 300 µm to 100 µm (where $r_i = 300$ µm). The numerical values for s to achieve the intended amount of R_{RMS} change are a function of both r_i and r_p as well, they are therefore summarised in Table 7.1. This dataset therefore simulates spatially

	No R_{RMS} scaling			**With R_{RMS} scaling**	
	$r_i = 100$ µm	$r_i = 200$ µm	$r_i = 300$ µm	$r_i = 100$ µm	$r_i = 300$ µm
$r_p = 0$ µm	$s = 1$	$s = 1$	$s = 1$	N/A	N/A
$r_p = 5$ µm	$s = 0.998$	$s = 1$	$s = 1$	$s = -16.81$	$s = 165.5$
$r_p = 15$ µm	$s = 0.99$	$s = 0.999$	$s = 1$	$s = -1.543$	$s = 21.99$
$r_p = 30$ µm	$s = 0.958$	$s = 0.99$	$s = 0.995$	$s = -0.164$	$s = 9.757$

Table 7.1: Simulated parameter sets for the backwall generator model. Parameter sets denoted as N/A have not been simulated.

correlated perturbation in addition to the same amount of random perturbation as in the previous dataset.

For each parameter set 200 backwall sequences were simulated, with 50 backwall samples each. Ultrasonic signals were simulated for all of the backwalls, which were then evaluated with each of the discussed signal processing methods. This resulted in 50 thicknesses per backwall sequence. Backwall sequences are therefore linked to a sequence of thickness estimates as produced by the signal processing techniques. For each backwall sequence and its corresponding thicknesses a thickness trend could be extracted using a linear least squares line fit. These trend lines were denoted $m_{1..200}$, *i.e.* one for each backwall sequence. The linear fits were then normalised with respect to the real underlying mean wall thickness loss by: $e_{1..200} = \frac{m_r - m_{1..200}}{m_r}$ where $e_{1..200}$ were the normalised trend errors, while m_r was the real underlying mean wall thickness loss.

The performance of signal processing methods were then compared based on the width of their thickness trend error distributions. In order to represent this visually for a large number of parameter sets, trend error distributions are shown as boxplots, where the boxes represent the data between the 25^{th} and 75^{th} percentile, whereas the whiskers represent data between the 5^{th} and 95^{th} percentiles. A visual representation of this is shown in Figure 7.3.

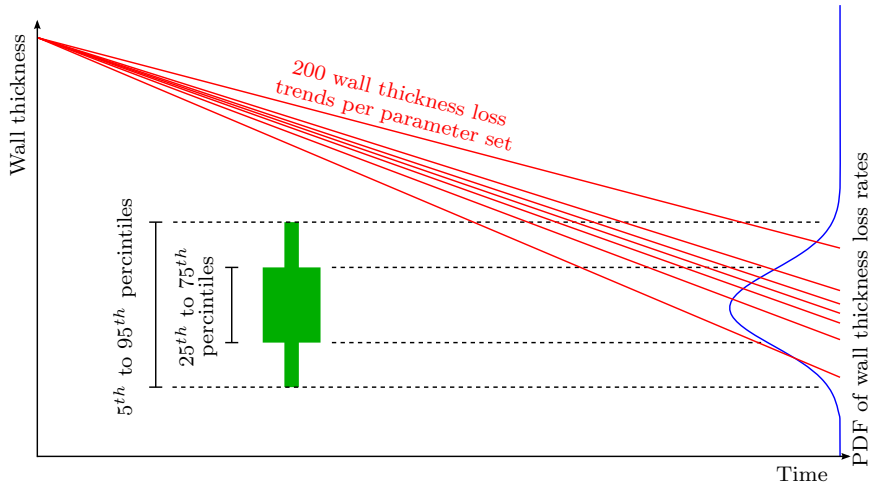

Figure 7.3: Boxplot representation of probability-density-function (PDF) of wall thickness loss trends.

7.3 Results

7.3.1 Backwall evolution without RMS change (only spatially random perturbation)

The results of the mean wall thickness loss trend error distribution plots for AXC, XC, P2P and FA methods under constant R_{RMS} conditions are shown in Figure 7.4. It should be noted that the axes on all graphs span between $\pm 100\%$, where 100% error means no wall thickness loss detected, 0% means that the wall thickness loss was measured accurately, and -100% means the wall thickness detected is twice as large compared to the underlying mean wall thickness loss.

It is particularly interesting to note the graph in the second column of the first row of Figure 7.4. Here, the box representing AXC is narrow and is close to 0%, revealing that wall thickness loss measured using AXC is accurate. The thick section of the box representing XC is also relatively narrow and also centred around 0%, however the thinner section of the same box spans significantly wider. This reveals that in most cases the wall thickness loss measurements using XC are accurate, while some of them are inaccurate. Overall the effects of both r_i and r_p are as expected across the various graphs, increasing R_{RMS} and perturbation widens the error bars of any signal processing method. This aligns with the conclusions of previous reports

suggesting that in general ultrasonic thickness measurements are sensitive to changes of backwall morphology [11, 38].

In addition, it is apparent from Figure 7.4 that on each and every plot the width of trend error distributions for AXC is narrowest. This is as expected, since the AXC algorithm was designed to perform better when monitoring gradually changing rough backwall surfaces. This is most noticeable on the right column of results in Figure 7.4, where $r_i = 300$ µm. Here the trend error distribution width of all standard methods (XC, P2P and FA) span between ±100%, while the trend error distribution

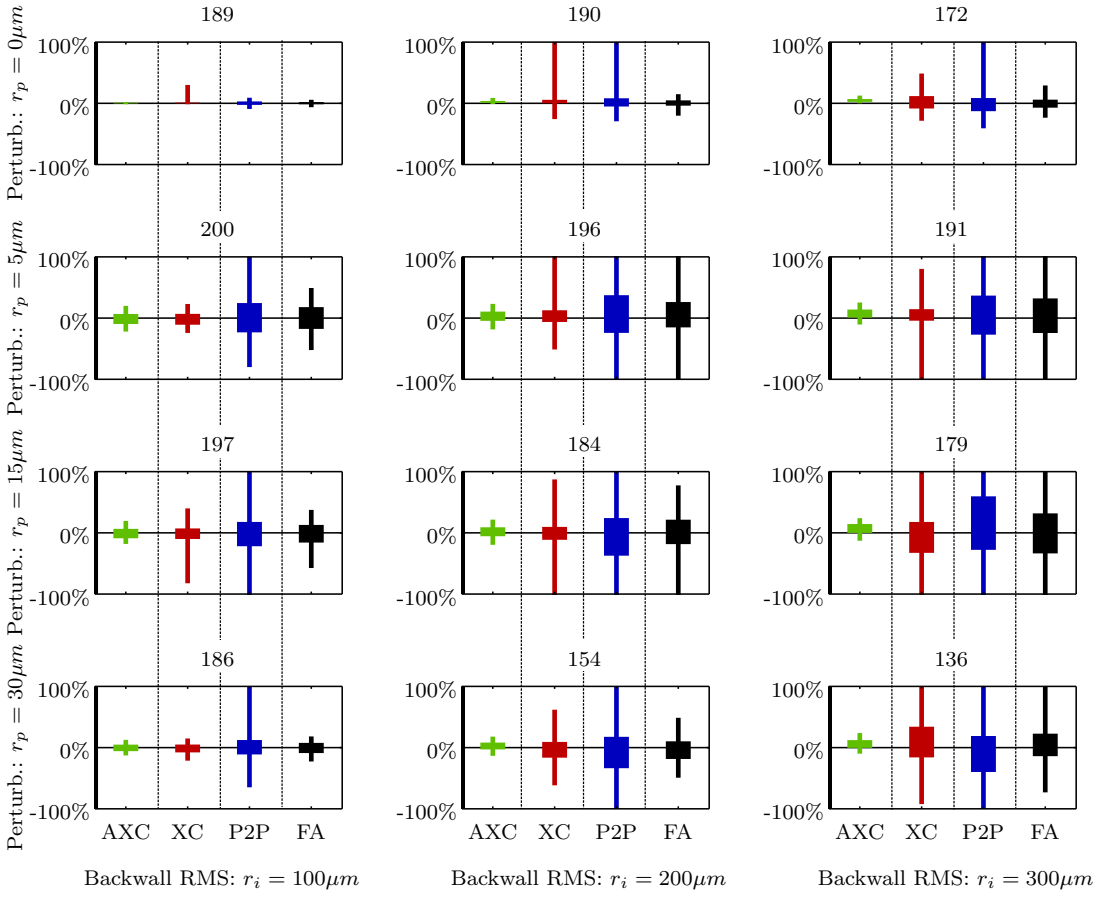

Figure 7.4: Distribution of normalised trend error $e_{1..200}$ for each backwall generator parameter set shown for each signal processing method. The green boxes represent the results for Adaptive Cross-Correlation (AXC), the red boxes are for Cross-Correlation (XC), the blue boxes are for Peak-to-Peak (P2P) and the black boxes are for First Arrival (FA) methods. Axes on all plots are identical for comparability. The numbers shown above each plot are the numbers of trends that have been evaluted.

width of AXC is close to an order of magnitude narrower spanning between +25% and −10%. This means that AXC has a slight bias to overestimate the thickness (or underestimate thickness loss rate), but this is negligible compared to the error of other methods.

In addition to benchmarking the accuracy of AXC, it is also essential to investigate its limitations. AXC is based on cross-correlation, and so the behaviour of XC is considered first. XC is sensitive to backwall roughness as shown by Figure 7.4. This breakdown in accuracy is caused by the distortion of the backwall echo wavepackets when the backwall surface is rough. When the backwall surface is rough and the signal is distorted, the synthesised toneburst used by XC does not correlate well with the received signal. Since XC relies on determining the biggest peak in the signal, in these cases a peak that is not representative of the mean wall thickness may be the biggest. Consequently, the wrong peak is often found for the purposes of the thickness measurement. This failure mode of XC was called peak jumping and will be referred to as such for the rest of the thesis.

AXC avoids this problem by using the backwall echo wavepacket from the previous measurement with which to cross-correlate, as it is much more likely to correlate well with the received signal. However, when the backwall surface changes significantly between measurements (which could occur in practice if ultrasonic signals are not acquired frequently), excessive signal distortion may occur. In this case the current signal will not correlate well with the previous backwall echo sample and AXC will be affected by peak jumping. For this reason AXC is expected to perform similarly to XC when applied to uncorrelated realisations of backwall surface geometries as evaluated by Jarvis *et al.* [11].

Although peak jumping may introduce large errors, it is simple to detect, since the error it causes is an integer multiple of $\sim \lambda/2$. It is also easily avoided by frequent measurements, as in a short time the backwall geometry is unlikely to change excessively. In addition, when measurements are carried out frequently, the thickness is not likely to change significantly and therefore the large error caused by peak jumping is even more straightforward to detect. Permanently installed monitoring is therefore well suited for AXC as it allows for frequent data acquisition.

The results shown in Figure 7.4 only show trends where AXC peak jumping does not occur. The number of trends out of the 200 simulated sequences that match this criterion is shown above each of the plots on the figure. It is apparent from the figure that although the distribution of trend errors is not affected significantly by increasing perturbation, the number of peak jumps is affected. This observation is in agreement with the concept that excessive change in backwall geometry causes peak jumps. This finding therefore confirms that frequent measurements are recommended when using AXC in order to ensure reliable and accurate thickness loss trends.

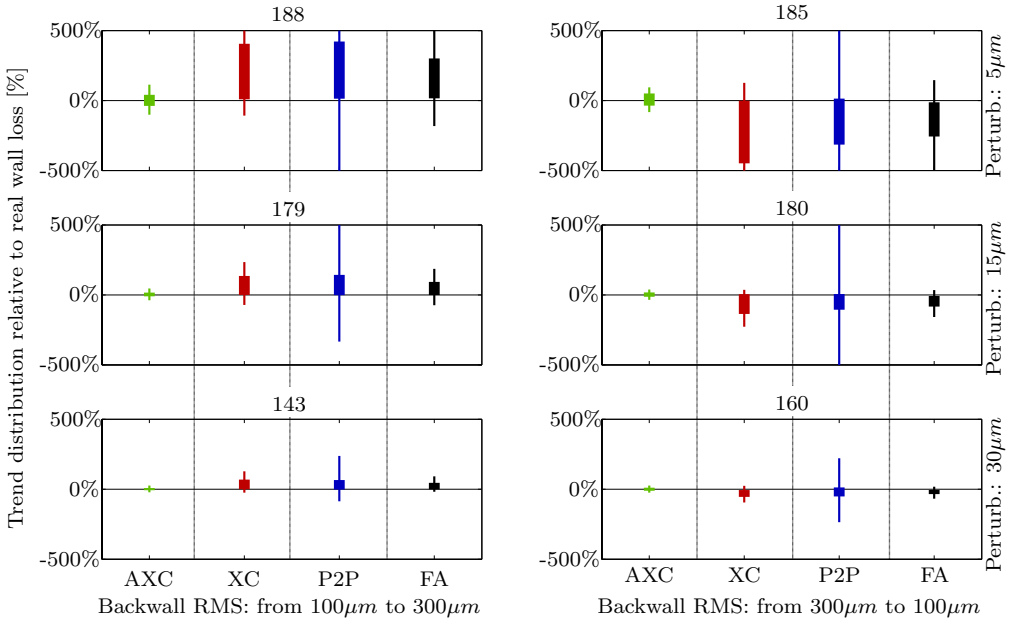

Figure 7.5: Distribution of normalised trend error $e_{1..200}$ for each backwall generator parameter set shown for each signal processing method with R_{RMS} scaling. The green boxes represent the results for Adaptive Cross-Correlation (AXC), the red boxes are for Cross-Correlation (XC), the blue boxes are for Peak-to-Peak (P2P) and the black boxes are for First Arrival (FA) methods. Axes on all plots are identical for comparability within the Figure, however they are 5 times larger compared to Figure 7.4. The numbers shown above each plot are the numbers of trends that have been evaluted.

7.3.2 Backwall evolution with RMS change (and spatially correlated perturbation)

The mean wall thickness trend error distribution plots with R_{RMS} scaling applied are shown in Figure 7.5. It should be noted that the axes of the plots in Figure 7.5 are 5 times larger than those of Figure 7.4. This larger range was chosen as the trend error distributions are substantially larger when R_{RMS} scaling is applied to the geometry. In order to better understand the reason for this, the behaviour of R_{RMS} scaling in the backwall sequence generator model is considered.

The R_{RMS} scaling was defined in the model as a factor that scaled the backwall geometry at every step. It therefore acts as a correlated perturbation term, since the change introduced by R_{RMS} scaling will be correlated between steps of the backwall sequence model and thinner parts of the component will become thinner and thicker parts will stay thicker relative to the mean thickness of the component. It is important to point out that this correlated perturbation caused by R_{RMS} scaling also introduces distortion in the ultrasonic signal in addition to that introduced by random perturbation. In the backwall sequence generator model, mean wall thickness loss however is linked to random perturbation alone, and it is not linked in any way to R_{RMS} scaling and hence correlated perturbation. Because of this, when random perturbation is small, the mean wall loss will still be small even if correlated perturbation is large. The error introduced by large correlated perturbation will however be large relative to the small mean wall loss. This can be observed on the top row of Figure 7.5, where the random perturbation r_p term is small but trend error distributions are large.

A real life example of a similar phenomenon is pitting. With pitting-type degradation mechanisms the backwall of the sample loses wall thickness in a non-uniform fashion as individual pits grow. The continuous growth of a pit is a type of spatially correlated perturbation, which may occur without significant mean wall thickness loss. Over time substantial changes in backwall geometry may occur, without much mean wall thickness loss, but still introducing large amounts of distortion in the ultrasonic signal.

Considering the results in Figure 7.5 quantitatively reveals that the trend error

distributions for all standard methods (XC, P2P, FA) extend well beyond the ±100% mark for all simulated scenarios. The worst case scenario is the top row of the figure, where correlated perturbation is most significant. AXC still performs better than any other signal processing method in all scenarios, however its performance is not as accurate as when uncorrelated backwall changes occur. The widths of normalized trend error distribution of AXC are as high as 200%, where error is quantified as the width of trend error distributions between the 5^{th} and 95^{th} percentiles. In comparison, the width of trend error distributions for all other methods (XC, P2P and FA) are of the order of 1000%. It is worth noting however, that when random perturbation is applied in higher proportion compared to correlated perturbation (bottom two rows of Figure 7.5, the error of all four methods (AXC, XC, P2P and FA) decrease significantly.

Another interesting feature of the displayed plots is that under increasing R_{RMS} conditions (left column of plots in Figure 7.5) XC, P2P and FA methods tend to overestimate the thickness. Under decreasing R_{RMS} conditions however (right column of plots in Figure 7.5) the same methods consistently underestimate thickness. This is thought to be the consequence of the interaction of the scattered wavefield from the backwall and the coherent backwall echo wavepacket: with increasing R_{RMS} the relative amplitude of the scattered wavefield increases - effectively delaying energy within the received wavepacket. An example of this distortion effect is shown in Figure 7.2.b. With decreasing R_{RMS} the opposite effect is observed, as expected.

For a more complete picture, the difference between the applicability of results with and without R_{RMS} scaling is pointed out here. It should be noted that the applicability of results presented in Section 7.3.1, where no R_{RMS} scaling was applied, is clearly defined as random perturbation itself is well defined. One should be more careful however when considering quantitative results with correlated perturbation present. This study is not intended to be representative of all real backwall perturbation processes, as the backwall morphology evolution of various corrosion/erosion processes may be highly specific. As an extreme example, very narrow, but deep pits evolving on the backwall surface may be considered. These are a form of correlated perturbation with close to zero mean wall loss. However, because of the changing backwall shape, the ultrasonic signal will be affected. This by the definition of the

error (or definition of the error reported in this study) would result in very large trend errors, since some thickness change will be detected with very little underlying mean wall loss. This is because the concept of mean wall thickness loss alone is not a good model for defect characterisation. It is expected however that adequate defect detection may be possible using the ultrasonic monitoring principle used in this thesis with a more appropriate approach, such as permanently installed arrays, and therefore may be interesting future work.

In addition to the problem of identifying the limits of correlated perturbation, the model used in this chapter has another limitation. Correlated perturbation in the model is simulated as scaling the backwall shape vertically. Consequently, no horizontal changes are introduced. A real pit would however be expected to grow both in the vertical and horizontal dimensions. Because of this, it is expected the vertical scaling only may not be realistic to simulate pits. However, at this point it is important to recall that it is the purpose of this chapter to provide an insight into the effect that different backwall change scenarios have on the ultrasonic measurement. Whereas more in depth analysis of correlated perturbation may be valuable, but would likely have to be specific to a degradation mechanism, and is therefore outside the scope of this thesis. It should also be noted that this study was carried out for a particular transducer geometry that is used in practice for thickness monitoring. Results would be slightly different for other transducer geometries, but most likely they will show the same trends as the scattering phenomenon and interaction with the rough backwall remains similar (*e.g.*: the study by Benstock and Cegla [108] has shown that variation of thickness measurements with round transducers is of similar order to that described by Jarvis [38]). Simply the size of the surface over which the wave field interacts with the surfaces will be different. Furthermore, it is expected that the relative performance differences between various signal processing methods are similar.

7.4 Summary

In this chapter the effect of continuously changing rough backwall surfaces on the accuracy and precision of ultrasonically monitored thicknesses was investigated.

This was achieved by means of a backwall sequence generator model that simulates gradual perturbation of backwall geometries. This model was then used to generate backwall sequences with a range of parameters, including various R_{RMS} heights and perturbation quantities. Instances of both spatially random and spatially correlated perturbation were generated. Ultrasonic signals were then simulated for all generated backwall geometries, which was evaluated using 3 standard signal processing methods: Cross-Correlation (XC), Peak-to-Peak (P2P) and First Arrival (FA). In addition, a new signal processing method, Adaptive Cross-Correlation (AXC) was proposed, which was developed specifically to provide accurate trend predictions for gradually perturbed backwall geometries. These 4 methods were used to calculate the thicknesses corresponding to the backwall sequences based on the simulated ultrasonic signals. Following this, the accuracy of estimated mean wall thickness loss trends were compared under the simulated conditions, allowing to compare the evaluated methods.

It was found that the accuracy of trend predictions varies significantly with signal processing methods. When the backwall geometry was perturbed randomly, the error of XC, P2P and FA methods were as high as $0\% \pm 100\%$, where error is quantified as the width of trend error distributions between the 5^{th} and 95^{th} percentiles. For the same ultrasonic signals the worst error of AXC was $7.5\% \pm 18\%$, close to an order of magnitude less than other methods. A slight underestimation of the AXC estimated wall thickness loss rate was also observed, but this was small compared to the error of other methods and the width of the distribution. Based on the presented data one can therefore conclude that when monitoring uniform corrosion mechanisms that result in 1 mm/year of loss then with AXC one would expect the actual result to be of the order of $0.75 - 1.1$ mm/year whereas the estimates of other algorithms would record rates between 0 and 2 mm/year.

With R_{RMS} scaling applied, which acts as a form of correlated perturbation, the error of all signal processing methods increased compared to the random perturbation case. AXC still performed best under these conditions - its 5^{th} to 95^{th} percentile trend error width was 200% compared to about 1000% of other methods. Therefore for corrosion mechanisms that result in correlated backwall changes (pitting-type) for a wall loss rate of 1 mm/year in the worst case $0 - 2$ mm/year would be measured

with AXC while other methods would result in −4 to +6 mm/year.

It was noted that correlated perturbation in extreme cases (*e.g.*: narrow, but deep pits) may result in very little mean wall thickness loss, while still causing distortion of the ultrasonic signal. In such cases mean wall thickness loss is not expected to be the key parameter of the pipe wall to be estimated, and instead other parameters, such as the minimum wall thickness (*i.e.*: deepest pit) would be of interest. Therefore further investigations of correlated perturbation with the specific aim to develop signal processing to detection and monitor more isolated defects are required.

Chapter 8

Thickness Loss Measurements on Evolving Rough Surfaces Using Multiple Transducers

8.1 Introduction

The previous chapter of this thesis has concluded that standard signal processing techniques for ultrasonic wall thickness loss measurements (XC, P2P, FA) are affected by significant errors when the internal wall surface is rough. It has also been shown that the errors have a strong dependence on backwall surface morphology conditions. A new signal processing method - Adaptive Cross-Correlation (AXC) - was presented as a method of decreasing errors by as much as an order of magnitude under all investigated conditions. However, the proposed AXC method was also shown to be susceptible to the effects of roughness, although to a lesser extent than standard methods (XC, P2P, FA). It was shown that under certain conditions (*i.e.*: with large amounts of correlated perturbation) errors may rise to relatively high levels. So far all the errors associated with the different signal processing algorithms were quantified based on comparison to the mean loss of the known and simulated geometry. It was not yet attempted to determine an estimate of the measurement error/range based on the measured data itself.

In this chapter methods to gain more information about the continuously progressing thickness loss phenomenon are discussed with the aim to both further improve the accuracy of the wall thickness loss measurements, and also to determine an indication of the accuracy of the wall loss estimate based on the measured data itself. Given that the accuracy of trend estimates varies considerably as a function of backwall geometry conditions, this would greatly increase confidence in the determined mean wall loss measurements in the field.

Here methods to gain accuracy are explored by collecting more data related to one particular thickness estimate. This is in contrast to the previous section, which relied on a single waveform for a given thickness estimate. A number of approaches to capture more data about a single backwall are considered. Methods to collect new information with as little change to readily available hardware as possible are described first, followed by alternatives requiring some degree of modifications. This order was chosen as fewer changes to hardware are easier to implement.

By default, a 5-cycle 2 MHz toneburst is used as excitation for the permanently installed waveguide sensor. The most straightforward approach to capture new information using the sensor assembly is to assess the viability of transmitting signals at different frequencies. Such a technique could be implemented by sending the two signals sequentially, and evaluating the two measurements in pairs. Introducing new frequency components compared to the originally proposed 5-cycle 2 MHz toneburst is difficult however, regardless of how that is achieved (*e.g.*: adjusting the centre frequency of the toneburst or adjusting the number of cycles). This is because low frequency components (approximately 1 MHz and lower) get distorted by the dispersive waveguides [25], whereas high frequency components are very susceptible to roughness (strongly attenuated) [109]. Initial processing did not reveal any gains so the concept of adjusting the sent toneburst was abandoned early on. Another approach to gather more data about a thickness loss mechanism is to use multiple transducer arrangements in order to take advantage of the spatial differences in the backwall morphology. In this chapter two possible approaches are investigated.

The first transducer arrangement that is explored in this chapter uses multiple angle illumination. Here, a sensor unit consists of 8 transducers in 4 pairs, that are used in pitch-catch mode. These 4 pairs of transducers nominally illuminate the same patch

of the backwall, but at different angles of illumination. The waves from the different angles of illumination reflect differently from the backwall surface, which should change the susceptibility to roughness of the measurement. (Obliquely incident waves are less affected by rough surfaces, consider *e.g.* sunlight reflection from the surface of the sea at low angles of incidence). Overall, the average of measured wall loss rates should be a more accurate prediction of the real mean wall thickness loss rate. In addition, the distribution of wall thickness loss rate estimates could be used to estimate the accuracy of the measured rate.

The second approach that was evaluated is grouping (or clustering) multiple independent backwall sequences that are generated with the same statistical parameters. A real life implementation of this sensor configuration would be multiple sensors coupled onto a pipe at close proximity, where the mean wall thickness loss can be assumed to be similar. In this application the sensors are expected to measure the same mean wall thickness rate, while the actual surface changes under each sensor are somewhat different. The mean of the measured wall loss rates and the spread can then be used to estimate the errors associated with the measurement, similarly to the multi-angle sensor configuration.

In this chapter both the multi-angle and sensor-cluster approach are investigated in detail. After the introduction of both sensor configurations, their performance is evaluated, compared and discussed. Finally, the conclusions of the two investigations are summarised and future work is outlined.

8.2 Geometry and measurement principles of proposed sensor configurations

8.2.1 Monitoring of rough surfaces using multiple angles

The advantage of an array of sensors installed at a particular location is that multiple measurements at the same spot on the wall can be made but at different incident angles. The sensor configuration that was considered is shown in Figure 8.1. This sensor configuration is based on 4 transducer pairs, each of them centred

at $x = 0$ mm with separations of $d = 2; 5; 10$ and 20 mm. For these pairs therefore the angle of illumination compared to the normal of the mean of the backwall is $\theta = 5.7°; 14°; 26.6°$ and $45°$. All waveguide pairs are used in pitch-catch mode and therefore they nominally illuminate the same patch of the backwall, with only the angle of illumination being different for each pair. The advantage of this approach is that the actual mean wall thickness loss rates for all measurements are identical.

Increasing the angle of incidence is the only control mechanism to decrease the dependence (in a statistical sense) of measurements, but adjusting it is only possible within finite bounds. This is because increasing the angle of incidence is only possible by increasing separation of the transmitter and receiver, which therefore also implies increasing the distance of wave propagation both for the surface wavepacket and backwall echo wavepacket. Once the separation reaches a threshold, the two wavepackets overlap and thickness estimation becomes significantly less accurate. This limit for the separation can be calculated as follows:

$$d = (4 \cdot f^2 \cdot T^2 - \Omega^2 \cdot c^2)/(2 \cdot \Omega \cdot f \cdot c) \tag{8.1}$$

where f is the centre frequency of the toneburst, Ω is the number of cycles in the

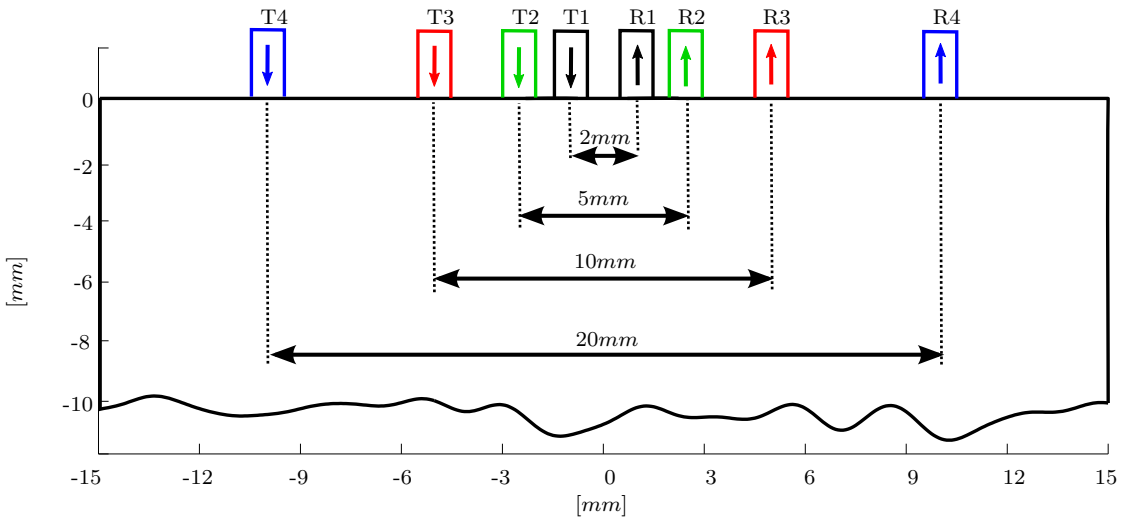

Figure 8.1: 4 different transducer pairs that have been investigated, with each pair denoted with the same colour. Those denoted with a T act as transmitters, whereas those denoted with an R are used as receivers. Since all 4 transducer pairs are centered around $x = 0$ mm, their specular reflection is nominally in the same location.

toneburst, T is thickness of the sample and c is the propagation velocity of the ultrasonic wave. For the parameters of this study at $T = 10$ mm according to Equation 8.1 the maximum separation is $d_{max} = 20.5$ mm. Therefore the widest separation of 20 mm shown in Figure 8.1 is the maximum realistic value for the thickness that was investigated.

8.2.2 Monitoring of rough surfaces with sensor clusters

For a wall thickness loss rate measurement on rough and evolving surfaces using a single sensor, the error distribution of wall thickness loss rate estimates has already been determined in the previous chapter. When a second sensor is added to measure the same wall thickness loss rate with a roughness evolution of identical statistical parameters, it is favourable to average the two estimates provided that the measurements of the two sensors are independent. This simple principle is applied in this section to multiple measurements of statistically uniform wall thickness loss scenarios.

The concept of independent measurements is implemented in this section by grouping (or clustering) multiple backwall sequence simulations that were generated in the same way (*i.e.*: randomly generated using identical r_i, r_p, CL, s parameters, but different instances thereof). Since the backwall sequence simulations are initiated in all cases by randomly generating the initial surface and then randomly perturbing it, they are inherently independent. The only link between backwall sequence simulations are the statistical parameters that were used to generate them (r_i, r_p, CL, s). These were then used as the basis for grouping them.

Although the primary purpose of the investigation is to gain an insight into whether grouping measurements would result in the average or median trend being more accurate, it is also important to consider practical implications. In practice, multiple sensors can be clustered at close proximity, where the mean wall thickness loss rate of the pipe can be assumed to be the same. The waveguide sensor assembly can be used without any need for modifications.

When using sensor clusters, the decision of how close the sensors should be coupled

onto the pipe should be considered. If the sensors are coupled too far apart from one-another, the assumption of identical mean wall thickness loss rate might break down. If the sensors are coupled too closely, the illuminated backwall surface area of the sensors may overlap, compromising the assumption of independent measurements. Therefore the question of how far apart sensors have to be spaced to ensure independent ultrasonic measurements is important.

The correlation length of the surface is the most important property that governs how far measurements will need to be spaced apart to result in independent measurements. Correlation length is defined as the spatial offset at which the autocorrelation of the backwall geometry falls below $e^{-1} \approx 0.37$ [11]. As a consequence of this definition, higher spatial offsets result in lower values of autocorrelation. A spatial offset of 3 correlation lengths results in an autocorrelation value of $e^{-3} \approx 0.05$. It is assumed here that backwall shapes 3 or more correlation lengths apart are therefore independent as their correlation is sufficiently low. In addition, it has been shown by Cegla *et al.* [109] that the waveguide sensor is not sensitive to correlation lengths higher than $4 - 5\lambda \approx 6 - 8$ mm. Hence, it is expected that ultrasonic measurement errors behave independently with a sensor separation of three times the maximum correlation length: $3 \cdot (6 - 8 \text{ mm}) \approx 20$ mm.

8.3 Data processing protocol

The previous section has introduced two approaches (multi-angle and clustered sensor configuration) for monitoring rough surfaces. In both sensor configurations, transducer pairs are used for pitch-catch measurements with signal processing identical to that in Chapter 7. Although the signal processing approach itself has not changed, it is summarised here for clarity. First, a waveform is simulated for a given backwall geometry. This waveform is filtered and a time-of-flight algorithm is applied. In this section all previously presented algorithms (AXC, XC, P2P and FA) are evaluated. The extracted arrival times are then used to calculate the thickness of the sample.

The resulting thickness measurements for multi-angle and clustered sensor configurations are then evaluated in the same way. The thickness measurements of m

transducer pairs are referred to as $T_{1..50}^{1..m}$, where m is the number of sensors for sensor-clusters, or $m = 4$ for multi-angle sensor configurations. Figure 8.2.a. shows an example of the thickness plots for 5 transducer pairs for a backwall sequence calculated using AXC. The mean wall thickness change per segment is then calculated for each of those backwall sequences referred to as $TC_{1..49}^{1..m}$, and is shown in Figure 8.2.b. As introduced in the previous chapter, AXC is occasionally affected by peak-jumping, a failure mechanism that results in large errors between two successive thickness measurements. Since in this section multiple mean wall thickness loss rate measurements are available, these errors can be identified and removed. This is implemented in an algorithm that is named trend-segment-averaging (TSA). Trend-segment-averaging ignores any thickness changes from one sample to the next with an absolute value of more than 0.4 mm. This is half of the error introduced by a single peak-jump, which is expected to be an integer multiple of half of the wavelength $\lambda/2 \sim 0.8$ mm. Following this, the algorithm calculates the median value of the remaining trend segments. In case all trends show a thickness rate with an absolute value of more than 0.4 mm for a given segment, then the mean of all rates are calculated. This means that if all measurements are affected by peak jumping for a given segment then the jump cannot be avoided but this is highly unlikely.

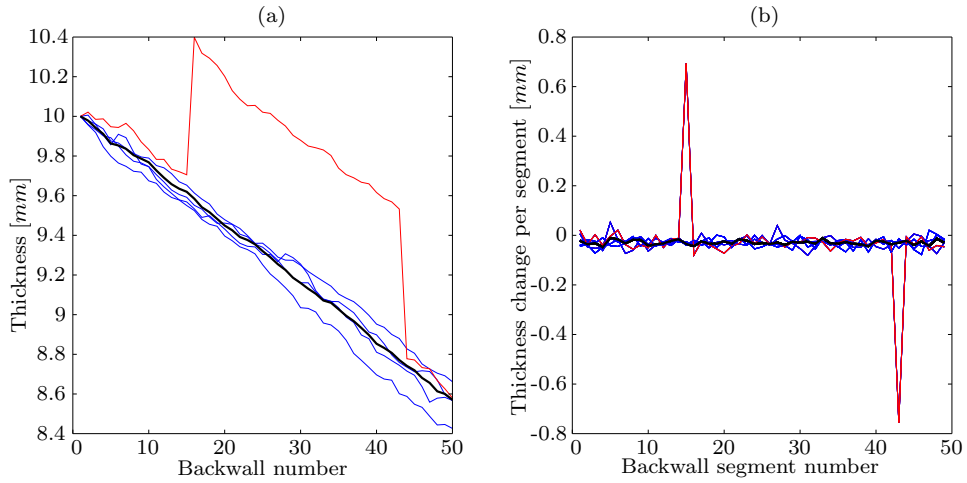

Figure 8.2: Calculated thicknesses using AXC for 5 sensors simulated as independent backwall sequences with $r_i = 300$ µm, $r_p = 30$ µm and no R_{RMS} scaling. 4 thickness trends are not affected by peak-jumping and are shown in blue. One of the thickness trends is affected by peak-jumping and is shown in red. The calculated thickness trend using trend-segment-averaging for these sensors is shown in black. Figure b shows the thickness change per step for the same sensors. Here the same colours represent the same thickness trends.

The calculated mean wall thickness trend is then referred to as $TC_{1..49}^{TSA}$. In order to calculate the thicknesses based on the calculated rates, the first thickness is defined as the median of thicknesses measured by all sensors: $T_1^{TSA} = median\,(T_1^{1..m})$. The remaining thicknesses are then defined as $T_{n+1}^{TSA} = T_n^{TSA} + TC_n^{TSA}$ where $n = 1..49$.

The process of trend-segment-averaging is therefore expected to significantly decrease the incidence of peak-jumping and is also expected to provide more accurate mean wall thickness loss rate estimates than a single transducer pair would. These more accurate trends for a multi-transducer sensor configurations are then treated and evaluated in the same way as in the previous chapter. This process is summarised here briefly. A linear fit is calculated for the measured thickness loss trends using the method of least squares. For a given parameter set, altogether 200 multi-transducer sensor configurations are evaluated, which results in 200 linear fits. The width of the linear fit distributions are then normalised based on the real underlying mean wall thickness loss, and this is visualised using boxplots. Plots produced in this fashion can be directly compared to those in the previous section, since the method of evaluation is identical.

If measurements from multiple transducers are available, it is possible to evaluate the distribution of the individual trends, and use this as an estimate of the accuracy of the mean wall thickness loss measurement. The ability to estimate that accuracy based on the measurement itself would greatly increase confidence in the measurement and will tell the user when to trust a measurement and when to have less confidence in it. The accuracy estimation method proposed here is initiated by calculating the best trend estimate using the trend-segment-averaging method described above. Peak-jumps are ignored here as well as any wall loss trend segment with an absolute value of more than 0.4 mm. Following this, the standard deviation is estimated the following way:

$$TC_{error}^{i} = median\left(TC_{1..49}^{i} - TC_{1..49}^{TSA}\right) \qquad \text{with } i = 1..m \tag{8.2}$$

$$GSTD = std\left(TC_{error}^{1..m}\right) \tag{8.3}$$

where TC_{error}^{i} is the error of thickness change per segment for each sensor and $GSTD$ is the estimated standard deviation for the sensor cluster. GSTD can therefore be used as an estimate of the standard deviation for the mean wall thickness loss rate.

8.4 Results

The primary aim of this section is to evaluate the extent to which accuracy can be improved using multi-angle or clustered sensor configurations under gradually changing backwall morphology conditions. The secondary objective is to investigate if accuracy can be estimated based on the measurements. The process to achieve this is similar to that of the previous section and is summarised here.

8.4.1 Method of comparison

For the clustered sensor configuration, the previous backwall sequences and the previous signals are grouped randomly. 200 clusters are created per parameter set. Here a cluster size of 12 sensors is investigated. All parameter sets with perturbation (summarised in Table 7.1) are included in this section. The cases where the backwall surface was not perturbed are omitted as their error was very low even when using only one sensor and therefore are not relevant for this study.

For both sensor configurations, all 4 signal processing methods (AXC, XC, P2P, FA) are then applied in combination with trend-segment-averaging to create a mean wall thickness loss trend per cluster of sensors. The distribution of the created trends are then shown on boxplots, similarly to the previous chapter.

8.4.2 Accuracy of multi-angle sensor configuration

Figure 8.3 shows the normalised mean wall thickness loss trend error results computed with the multi-angle sensor configuration by trend-segment-averaging measurements from all 4 angles. Comparing results from Figure 8.3 to the results with single sensors (Figures 7.4 and 7.5 in the previous chapter) reveals that the most significant difference between the figures is the number of peak-jumps. Using the multi-angle sensor configuration resulted in only 8 peak-jumps for AXC out of the 3000 simulated backwall sequences, an incidence of just 0.3%.

An interesting aspect of these results is that the performance of XC appears to be

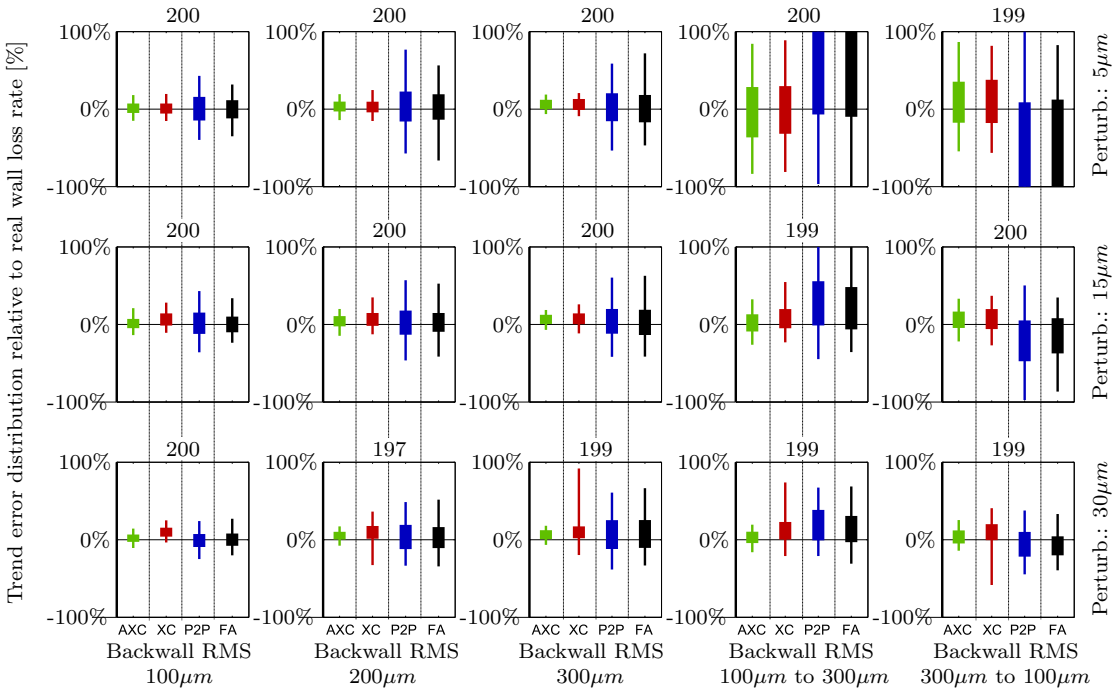

Figure 8.3: Mean wall thickness loss trend error distribution results for all 4 investigated angles with trend-segment-averaging. The green boxes show results for Adaptive Cross-Correlation (AXC), the red boxes represent Cross-Correlation (XC), the blue boxes are for Peak-to-Peak (P2P) and the black boxes are for First Arrival (FA) methods. All plots are shown with the ±100% axes for comparability with other results. Correlated perturbation results (first two columns from the right) are also shown with ±100% axes, which are directly comparable to the results using 12 independent sensors shown in Figure 8.4.

almost the same as AXC. This is because the trend-segment-averaging approach works very efficiently in identifying peak-jumps, which greatly improves the performance of XC. The P2P and FA algorithms however do not exhibit a similar peak-jumping behaviour, and their performance is not affected by peak-jump filtering.

8.4.3 Accuracy of clustered sensor configuration

Figure 8.4 shows the results computed with sensor-clusters of 12 sensors. Comparing these results with those of Figure 7.4 and Figure 7.5 in the previous chapter it is apparent that the peak-jumps have been eliminated completely in all simulated parameter sets. The width of trend error distributions have decreased as well. In theory, the standard deviation of the results when averaging independent measurements is expected to decrease by the square-root of the number of averages [51]. This rate of

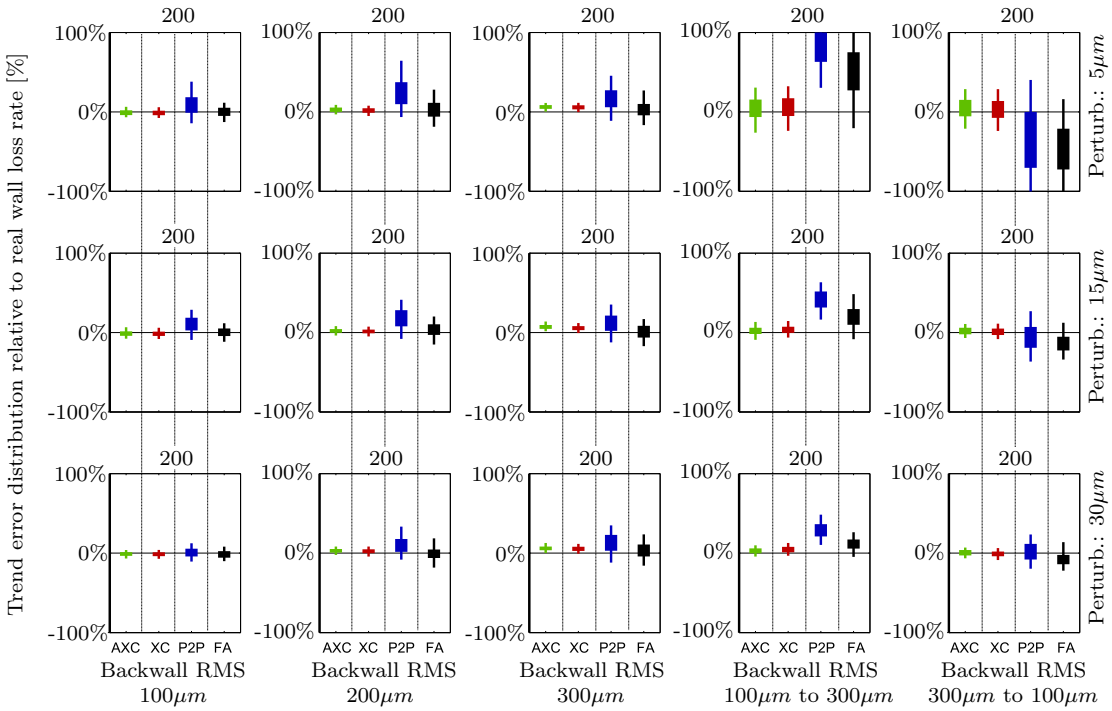

Figure 8.4: Mean wall thickness loss trend error distribution results for 12 sensor clusters. The green boxes show results for Adaptive Cross-Correlation (AXC), the red boxes represent Cross-Correlation (XC), the blue boxes are for Peak-to-Peak (P2P) and the black boxes are for First Arrival (FA) methods. All plots are shown with ±100% axes for comparability with other results. Correlated perturbation results (first two columns from the right) are also shown with ±100% axes, which are not directly comparable to those in the previous chapter.

accuracy improvement is confirmed when comparing Figure 8.4 with Figures 7.4 and 7.5 in the previous chapter. For example, with 5 µm perturbation and a backwall RMS of 100 µm the normalised trend error width decreased from ±20% (when using a single sensor) to ±6% when using a cluster of 12 sensors. The error therefore decreased by $1 - \frac{6}{20} = 70\%$, which is similar to what is expected from averaging 12 measurements: $1 - \frac{1}{\sqrt{12}} \approx 71\%$. In addition, the accuracy of XC has improved here as well and nearly matches that of AXC, similarly to the results of the multi-angle sensor configuration.

8.4.4 Error estimation using multi-angle sensor configuration

The results for the estimated standard deviations (GSTD) using the data from all 4 angles of the multi-angle sensor configuration are shown in Figure 8.5. From the figure it can be seen that estimation of standard deviation for wall thickness loss rates is very limited for any signal processing method using the multi-angle sensor configuration. The explanation for this is the same as for the lack of improvement in accuracy: the measurements using the various angles are simply too dependent, and therefore any benefit is limited.

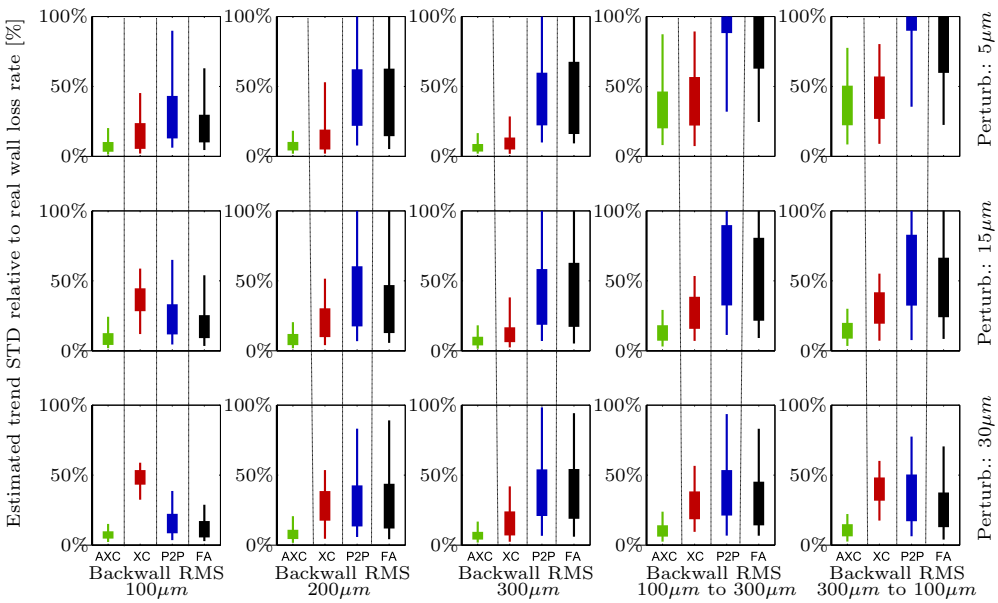

Figure 8.5: Estimated standard deviation of calculated mean wall thickness trend distribution results for results from all 4 angles of the multi-angle sensor configuration. The green boxes show results for Adaptive Cross-Correlation (AXC), the red boxes represent Cross-Correlation (XC), the blue boxes are for Peak-to-Peak (P2P) and the black boxes are for First Arrival (FA) methods. All plots are shown with identical axes for comparabilty with other results.

8.4.5 Error estimation using the clustered sensor configuration

Figure 8.6 shows the results of estimated trend standard deviation (GSTD) using sensor-clusters for a cluster size of 12 sensors. It is clear that the AXC and XC methods are the most accurate in this investigation as well, as a consequence of filtering out peak-jumps. It is apparent that using data from multiple sensors clearly allows for qualitative differentiation of the worst cases of backwall shape change (top right plot) compared to those with less significant change (left 3 columns of subplots) using either AXC or XC. When using 12 sensors in a cluster, qualitative estimation of the accuracy is also feasible. Based on Figure 8.6 the estimated standard deviation (GSTD) of trends based on AXC are below 18% in all of the plots from the left 3 columns. Comparing this to the results in Figure 7.4 (measurements using a single transducer pair in the previous chapter), the estimated GSTD values are accurate. All other parameter sets behave similarly, estimated standard deviations (GSTD)

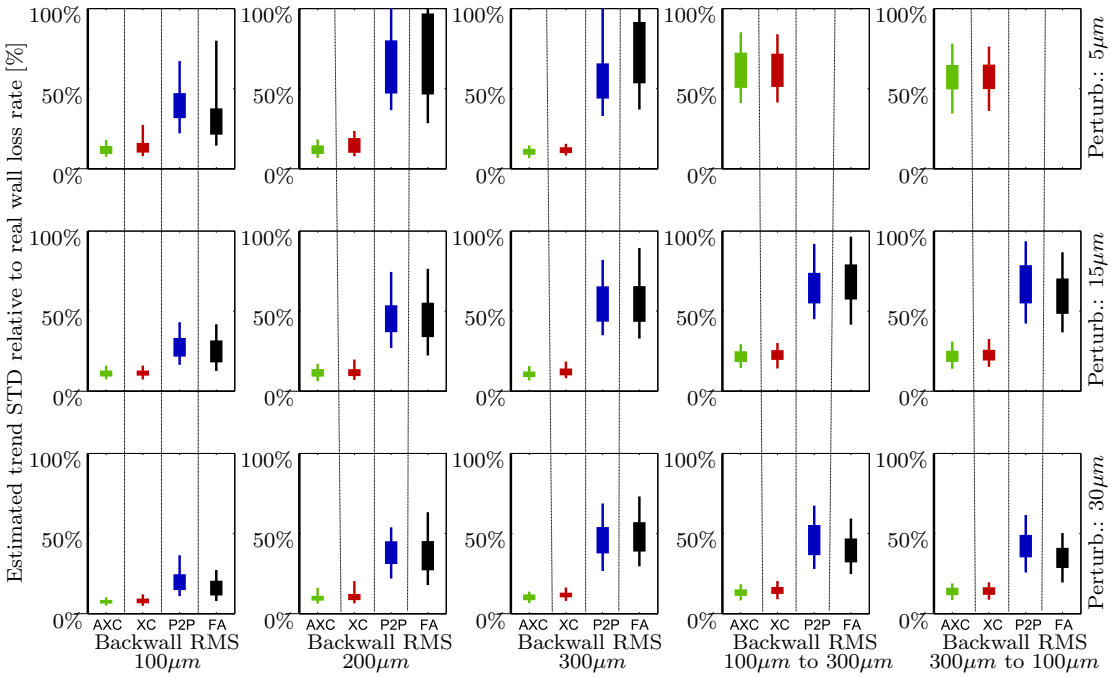

Figure 8.6: Estimated standard deviation (GSTD) of calculated mean wall thickness trend distribution results for 12 sensor clusters. The green boxes show results for Adaptive Cross-Correlation (AXC), the red boxes represent Cross-Correlation (XC), the blue boxes are for Peak-to-Peak (P2P) and the black boxes are for First Arrival (FA) methods. All plots are shown with identical axes for comparabiltiy with other results.

shown in Figure 8.6 are reasonably accurate compared to those expected from Figure 7.5.

8.5 Discussion

The results clearly show that in some scenarios using a multiple transducer sensor configuration can be beneficial. The degree to which improvements can be achieved depends on the sensor configuration. It was shown that the benefit of using a multi-angle sensor configuration is limited. One of the main difficulties in implementation is that the largest illumination angle and therefore the maximum transducer separation is a function of the pipe thickness. Results showed that the benefits of using a multi-angle sensor configuration are limited to the mitigation of the peak-jumping phenomenon, which may only be of practical use when very severe backwall geometry changes are expected. However, frequent sampling is also expected to result in a decrease of peak-jumps and therefore the multi-angle sensor configuration may be of limited use in a real application.

Simulations of grouping independent backwall sequences, representing an ideal clustered sensor configuration, show more promise. It is feasible to eliminate peak-jumping completely and improvements in estimated mean wall thickness loss rate accuracy can also be achieved when using multiple transducers. Trend accuracy estimation has also been shown to be possible in simulations. Therefore it is concluded that the approach of using multiple independent measurements is effective.

It should be noted that in practice this sensor configuration may have limitations compared to what was shown in the simulations: a possible problem in a real application is that the mean wall thickness loss rate under each of the sensors in a cluster will be different. This has not been investigated in simulations, as all clusters were formed by backwall sequences with the same underlying mean wall thickness loss rate. In case the wall thickness is lost at a different rate under various sensors, it is expected that the estimated standard deviation (GSTD) of the cluster would be relatively large, depending on the severity of differences in wall loss rate. It would be interesting future work to quantitatively estimate the deviations that

can be introduced in such scenarios. It may be possible to use amplitude changes and waveform distortion as an indicator to help evaluate whether backwall shape changes are taking place or if the underlying mean corrosion rate is genuinely different corresponding to various sensors. Sensor sub-clustering may be another plausible approach, which could help identify outliers within the cluster. These concepts have not been investigated in this thesis, but they are thought to be potentially interesting future work.

Although the ability to estimate the standard deviation of the measurements is practical, it is still desirable to maximise accuracy. Therefore it is essential to ensure that the mean wall thickness loss rates below sensors are the same. It is expected that in a real application mean wall loss rates are more likely to be similar when sensors are coupled close to one-another, regardless of corrosion phenomena. As explained earlier however, coupling sensors too close to each other could violate the assumption of independent measurements. It has been discussed that ultrasonic measurements using waveguide sensors coupled with a separation of 20 mm or more result in independent measurements. In practice sensors cannot physically be coupled closer to one another than 20 mm because of the width of their coupling clamp, hence in practice their measurements are expected to be independent and so the positioning of sensors can be arbitrarily chosen.

Other methods may be potentially useful for transducers other than the waveguides, such as changing the centre frequency of the sent toneburst between measurements. No other alternatives were investigated here however, since the transducer used in the study is not suitable for such approaches. In addition, independent measurements from a multi-sensor cluster constitute the maximum achievable accuracy for a given number of measurements.

8.6 Summary

In this chapter the potential gain in accuracy for estimating a single mean wall thickness loss rate using multiple transducers has been investigated in simulations. In addition, the feasibility of estimating the standard deviation of the mean wall

thickness loss rate based on the measurements from multiple transducers was also investigated. Both of these expected improvements have been evaluated for two proposed sensor configurations.

The first sensor configuration used 4 pairs of transducers in pitch-catch mode illuminating the same patch of the backwall at different angles. One of the biggest improvements this method demonstrated was a significant reduction in number of peak-jumps compared to the use of data from a single transmitter receiver pair only. With the multi-angle sensor configuration only small accuracy improvement was shown to be achievable using AXC compared to the standard sensor configuration.

The second proposed sensor configuration relied on a cluster of multiple sensors coupled to a sample at close proximity, where the mean wall thickness loss rate is identical. In simulations, the sensors in the cluster were represented by independent backwall sequence simulations generated using statistically identical parameters $(r_i; r_p; CL,\ s)$. It was found that using a cluster size of 12 sensors, the accuracy of all signal processing methods increased compared to single sensors in the previous chapter, most notably Adaptive Cross-Correlation (AXC) and Cross-Correlation. The accuracy of AXC increased by 69%, which is proportional to the square root of number of sensors in the cluster ($1-\frac{1}{\sqrt{12}} \sim 71\%$). In addition, the peak-jumps of AXC have been eliminated entirely. Standard deviation estimation (GSTD) using results from 12 sensors has been shown to be accurate enough for qualitative estimates (*i.e.*: small or large error). Clustering fewer than 12 sensors has been shown to promise similar benefits, however the accuracy of standard deviation estimation (GSTD) decreases if fewer sensors are used. In addition, practical difficulties with a real implementation of sensor clustering were discussed: when sensors are clustered on a real pipe, the underlying mean wall thickness loss for each of those sensors may be different. It was preliminarily concluded that such an scenario would likely increase the standard deviation estimate (GSTD), and hence would be detectable. It was also concluded that sensors should be coupled onto the pipe as closely as possible. As a guideline, it was concluded that coupling sensors as close as 20 mm would result in independent measurement error and therefore results would be expected to behave as reported in this study.

As future work it may also be interesting to investigate combining the multi-sensor

approach and the multi-angle approach in a waveguide array. The array sensor configuration could provide reasonably independent measurements with reasonably similar corrosion rates, although both assumptions may be compromised to some extent. However, the consideration of how localised certain corrosion/erosion phenomena are is expected to be specific to the particular corrosion mechanisms, which may be a good starting point for further analysis.

Chapter 9

Conclusions

9.1 Thesis Review

In this thesis maximising the precision of permanently installed ultrasonic time of flight sensors was investigated. Various sources of variability affecting the measurement precision were evaluated and a measurement protocol was suggested to minimise variability. The repeatability that can be achieved with the described measurement protocol was verified in simulations and in laboratory corrosion experiments as well as various other experiments. One of the most significant and complex problems affecting the precision, inner wall surface roughness, was also investigated and a signal processing method was proposed to improve the accuracy of estimated wall thickness loss rates by an order of magnitude compared to standard methods.

The background and theory on ultrasonic wave propagation that supports this research was introduced in Chapter 2. It was explained that permanently installed ultrasonic sensors in particular have the potential to carry out time of flight measurements such as thickness measurements with very high repeatability. In addition, they are also well suited to carry out such measurements at short regular intervals. Increased measurement precision and decreased measurement intervals allow for greatly increased accuracy in measured component wall thickness loss rates. Because of the substantial gain in rate estimation accuracy, permanently installed monitoring was established as a central concept in the thesis. It was also explained that most

investigations in this thesis are aimed to be generic, however in order to be able to compare techniques that are presented in the thesis quantitatively, an example permanently installed sensor was needed. A waveguide-based permanently installed sensor was introduced, that was then used throughout the thesis to benchmark presented methods that aim to maximise the precision of time of flight measurements.

With the generic concept of permanently installed time of flight measurements established, potential sources of uncertainty were evaluated in Chapters 3 and 4. First, parameters of the signal acquisition hardware were looked at (*e.g.*: sampling frequency, quantisation resolution and amplitude range). Signal processing, including filtering, averaging, arrival time estimation methods were then investigated. In addition, experimental error sources that affect most measurements were also discussed. This included evaluating coherent noise, coupling stability and temperature effects.

With all aspects of the signal acquisition and processing evaluated, a signal processing protocol was established. The precision that can be achieved with this protocol was experimentally verified using a corrosion rig in Chapter 5. Both corrosion forced by applied current and unforced corrosion were monitored by online ultrasonic measurements using the waveguide sensor. Here, the accuracy of ultrasonically measured wall thickness loss rates were compared to electrochemically predicted corrosion rates. Electrolytes that were tested were distilled water, NaCl, Na_2SO_3, citric acid and HCl.

Beyond corrosion experiments, the feasibility of material degradation monitoring was assessed in Chapter 6 via measurements of ultrasonic propagation velocity. First, propagation velocity changes caused by a non-uniform temperature distribution were created. Ultrasonic measurements were carried out during the heating of the monitored component and the measured data was used to reconstruct the propagation velocity map, which was then converted into the temperature map. In addition, the feasibility of monitoring hydrogen attack, a degradation mechanism expected to cause a shift in ultrasonic propagation velocity similar to the effect of temperature, was also evaluated. For this, a hydrogen attack rig was built that was capable of inducing the degradation mechanism while being monitored using the waveguide sensor.

Although the precision that can be achieved in experiments using a permanently installed ultrasonic sensor was demonstrated, it was noted in Chapter 7 that surface geometry changes of the inner wall surface (*i.e.* backwall roughness) may introduce large errors in measurements. Chapter 7 therefore investigated the effects of gradual changes in inner surface geometry of the monitored component on ultrasonic measurements. Gradual changes in surface geometry were investigated as it is expected that permanently installed sensors carry out measurements at a single location at high frequency, and therefore it is expected that the surface geometry changes gradually between measurements. Here the performance of common arrival time estimation methods were compared for a range of gradually changing simulated backwall surface geometries. A new arrival time estimation method, Adaptive Cross-Correlation (AXC) was also introduced with the aim to improve the accuracy of estimated wall thickness loss rates compared to traditional methods.

The feasibility of monitoring a single wall thickness loss rate for a gradually changing rough backwall using multiple transducers was then looked at in Chapter 8 with the hope of improving the accuracy of the measured wall thickness loss rates. Two setups were evaluated. The first setup used multiple transducers illuminating the same patch of the backwall from multiple angles, whereas the second setup relied on independent transducer pairs below which the underlying wall thickness loss can be assumed to be identical.

9.2 Main Findings

The main findings of this thesis are as follows:

- A signal acquisition and processing protocol that was experimentally demonstrated to be capable of measuring wall thickness with a precision of 20 nm was established
- A new arrival time estimation method (AXC) was developed and shown to improve the precision of wall thickness loss rate estimation by an order of magnitude compared to standard methods on rough and evolving backwall surfaces

- Further improvement in wall thickness loss rate estimation of rough backwall surfaces was demonstrated using a multi-sensor setup

Evaluating signal generation, acquisition and processing revealed that it is possible to measure wall thicknesses of components at nanometre precision using permanently installed ultrasonic sensors with temperature compensation and raw signal to noise ratios of the order of 52 dB by applying the signal processing protocol that is described in this thesis. It was also shown that the precision of wall thickness estimates in experiments is typically limited by the temperature compensation that is applied. When temperature changes are small (< 0.1 °C) a standard deviation of 14 nm was measured in wall thickness estimates using the established signal processing protocol. Further experimental results showed that realistic temperature changes of the order of 5 °C limit precision of wall thickness estimates to 1 µm. In addition, larger changes in temperature (of the order of 400 °C) are expected to cause errors of up to 20 µm during heating transients.

Inner wall surface roughness was shown to potentially introduce even larger errors than temperature, but is not expected to affect all monitored specimens. It was demonstrated that standard processing methods estimate mean wall thickness loss rates with an accuracy of the order of $\pm 100\%$ even with moderate amount of spatially random surface shape changes. When spatially correlated inner wall surface shape changes occur, error bars have been shown to be even higher and may reach $\pm 500\%$. This showed not only that standard methods may be inaccurate when monitoring rough inner surfaces, but also that an increase in mean wall thickness may be measured in some cases, while the real underlying wall thickness decreases. A new arrival time estimation method, Adaptive Cross-Correlation (AXC) was then introduced and was shown to improve mean wall thickness loss rate estimation accuracy by almost an order of magnitude. The accuracy of AXC was shown to be $7.5 \pm 18\%$ when inner surface shape changes are spatially random and $\pm 100\%$ when surface changes are spatially correlated. Attention was drawn to the fact that the mean wall thickness describes the wall thickness loss of spatially random loss mechanisms well, whereas mean wall thickness loss is not a good representation of spatially correlated phenomena such as pitting.

Even further increase in achievable wall thickness loss rate accuracy was shown using a multi-sensor setup, where accuracy was shown to increase to ±30% (worst case scenario) with AXC using a 12 sensors cluster when monitoring spatially correlated surface changes. This constitutes an improvement of 70% compared to the performance of a single sensor setup. Furthermore, it was shown that the accuracy of the calculated wall loss rate can be estimated based on the measurement itself using the multi-sensor cluster. This is thought to be a key improvement, as the accuracy of wall loss estimates vary significantly depending on the type of the inner wall surface shape change (*i.e.* spatially random or spatially correlated). The accuracy estimation using the multi-sensor setup therefore helps increase confidence in the ultrasonic wall thickness loss measurements, as the accuracy of the measurements can be estimated and it is not necessary to make assumptions about how spatially correlated the underlying surface changes are for a measurement.

In summary, it was demonstrated that very high precision can be achieved in experiments and that such precision is expected to be achievable using sensors with signal to noise ratio of the order of 40 dB and above. It was also shown that even with severe changes to inner wall surface roughness a wall loss estimate accuracy of ±30% can be achieved using a multi-sensor setup with AXC. Furthermore, it was demonstrated that the accuracy can be estimated based on the measurement itself, which is expected to greatly increase confidence in ultrasonic wall loss estimate measurements. Techniques presented in this thesis therefore allow for the accurate monitoring of components in a wider range of conditions and for more forms of degradations compared to what had been possible before. In addition, the techniques presented are expected to be readily applicable for implementation in field.

9.3 Proposed Future Work

Although it was shown that techniques presented in this thesis are capable of accurately monitoring components with gradually changing inner wall surface roughness even if those shape changes are spatially correlated, it was also explained that the estimation of mean wall thickness loss is not expected to be a good model for monitoring very localised defects, such as narrow pits or cracks. In the future, defect

monitoring techniques should therefore be developed that can be used in parallel with techniques for monitoring general mean wall thickness loss described here. Such techniques would need to identify when a defect (*e.g.* a pit or a crack) is more dominant than the underlying mean wall thickness loss hence allowing for a more complete assessment of component health status.

Another area of potential improvement is the accuracy of temperature compensation. Excluding inner wall surface roughness, temperature was found to be the largest contributor of error for typical measurements, hence improving the accuracy of temperature compensation is expected to translate directly into more accurate wall thickness loss measurements. By better modelling the distribution of temperatures within the component wall may allow for decreasing the errors that were measured in this thesis. In addition, it is thought that investigating the possibility of insulating the temperature measurement device (*i.e* thermocouple) from ambient air-flow may lead to improved temperature measurements and hence more effective temperature compensation.

Lastly, it would be interesting to improve the hydrogen attack rig that was described in this thesis. Measurements described here were stopped prematurely as the ultrasonic sensor signal quality degraded as a result of contact patch corrosion. This is because the ultrasonic sensor was not adequately protected from the corrosive environment that was necessary for laboratory induced hydrogen attack. By better protecting the sensor, it may be possible to continue the experiment for longer periods of time, hence increasing the amount of induced degradation while preserving the quality of ultrasonic measurements.

Appendix A

Appendix

A.1 Derivation of slope error in Equation 2.16

Equation 2.15 has established that the variability of a thickness slope can be estimated assuming that the variability of individual thickness measurements are identical. The equation is repeated here:

$$\sigma_{slope} = \frac{\sigma}{\sqrt{\sum (t_i - \bar{t})^2}} \tag{A.1}$$

This can be simplified by assuming that N number of measurements are carried out at equal Δt intervals in a period of $\widehat{t} = N \cdot \Delta t$ time. Given that:

$$t_i = (i-1) \cdot \Delta t \tag{A.2}$$

and

$$\bar{t} = \frac{(N-1) \cdot \Delta t}{2} \tag{A.3}$$

it is possible to expand $\sum (t_i - \bar{t})^2$ from Equation A.1:

$$\sum (t_i - \bar{t})^2 = \Delta t^2 \sum \left((i-1) - \frac{N-1}{2} \right)^2 = \Delta t^2 \sum \left(i^2 - (N+1) \cdot i + \frac{(N+1)^2}{4} \right) \tag{A.4}$$

Using standard expressions for sums, this simplifies to:

$$\sum (t_i - \bar{t})^2 = \Delta t^2 \left(\frac{2N^3 + 3N^2 + N}{6} - \frac{N(N+1)^2}{2} + \frac{N(N+1)^2}{4} \right) \tag{A.5}$$

Which then reduces to:

$$\sum (t_i - \bar{t})^2 = \frac{\Delta t^2}{12}(N^3 - N) \tag{A.6}$$

This can then be substituted back to Equation A.1 to produce what is Equation 2.16:

$$\sigma_{slope} = \frac{\sigma\sqrt{12}}{\Delta t\sqrt{N^3 - N}} \tag{A.7}$$

A.2 Polynomial fits for ultrasonic propagation velocity - temperature calibration curves

Material	**Velocity at 20 °C** [m/s]	**Slope = P(1)** [m/s/°C]	**Offset = P(0)** [m/s]	**Temperature at which max error** [°C]	**Max Error** [m/s]
S275	3265.28	-0.62778	3277.84	38.30	10.35
304 SS	3173.69	-0.78157	3189.32	39.91	2.04
316 SS	3157.47	-0.80513	3173.57	26.58	5.05
CR12	3274.24	-0.61008	3286.44	430.58	9.09
CR5	3309.09	-0.59486	3320.99	430.37	9.26
CR9	3360.95	-0.63146	3373.58	428.02	12.64

Table A.1: Temperature compensation constants for 6 different alloys using a linear fit, where $c = P(1) \cdot T + P(0)$ where c is the ultrasonic propagation velocity, T is the temperature and $P(1) and P(0)$ are the parameters of the fit.

Material	Velocity at 20 °C [m/s]	P(2)	P(1)	P(0)	Temperature at which max error [°C]	Max Error [m/s]
S275	3251.17	-0.00049	-0.413460266	3259.64	402.34	3.75
304 SS	3173.23	-0.00001	-0.775028987	3188.73	39.91	1.70
316 SS	3154.04	-0.00012	-0.75249286	3169.14	429.58	2.54
CR12	3257.43	-0.00042	-0.402123254	3265.64	431.25	0.61
CR5	3292.84	-0.00042	-0.390783686	3300.82	433.24	0.95
CR9	3347.35	-0.00046	-0.422219199	3355.98	26.54	1.75

Table A.2: Temperature compensation constants for 6 different alloys using a quadratic fit, where $c = P(2) \cdot T^2 + P(1) \cdot T + P(0)$ where c is the ultrasonic propagation velocity, T is the temperature and $P(2), P(1) and P(0)$ are the parameters of the fit.

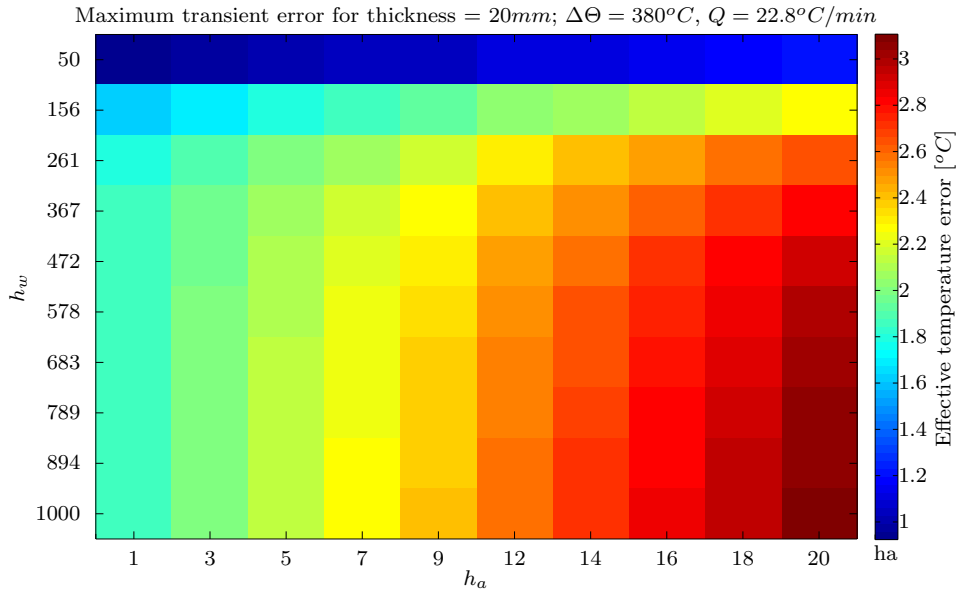

Figure A.1: Estimated maximum transient error (METEST) values for a 20 mm thick pipe. The maximum temperature difference in the simulation is $\Delta\Theta = 380$ °C and heating rate is 22.8 °C/min

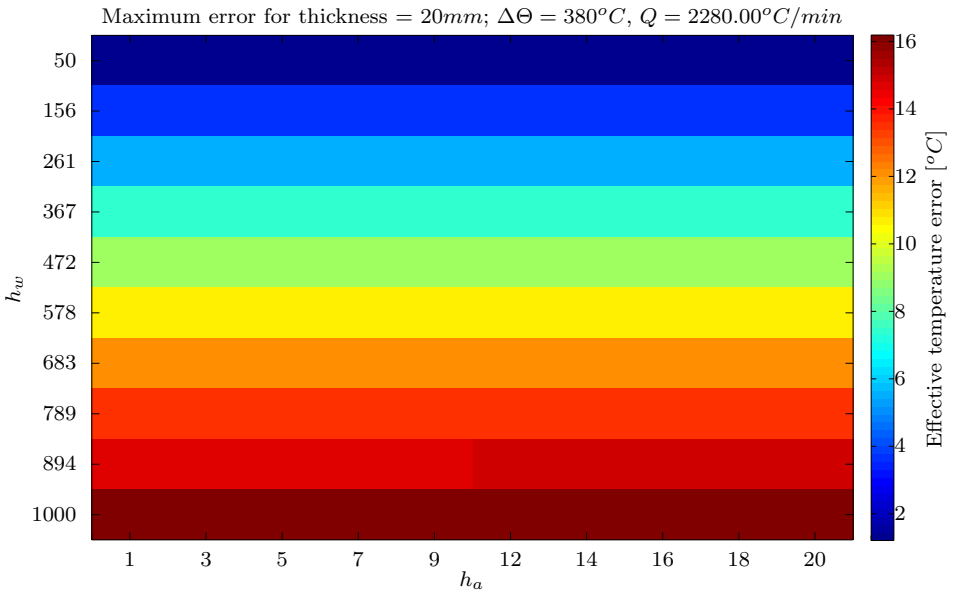

Figure A.2: Estimated maximum transient error (METEST) values for a 20 mm thick pipe. The maximum temperature difference in the simulation is $\Delta\Theta = 380$ °C and heating rate is 2280 °C/min

References

[1] L. Garverick. *Corrosion in the petrochemical industry.* ASM International, 1994.

[2] E. Slavcheva, B. Shone, and A. Turnbull. Review of naphthenic acid corrosion in oilrefining. *Br. Corros. J.*, 34(2):125–131, 1999.

[3] M. Matsumura. *Erosion-Corrosion: An Introduction to Flow Induced Macro-Cell Corrosion.* Bentham Science Publishers, 2012.

[4] P. Riccardella, A. Deardorff, and T. Griesbach. *Advances in Fatigue Lifetime Predictive Techniques*, volume 1122. ASTM International, 100 Barr Harbor Drive, PO Box C700, West Conshohocken, PA 19428-2959, January 1992.

[5] H. C. Furtado and I. L. May. High temperature degradation in power plants and refineries. *Mater. Res.*, 7(1):103–110, 2004.

[6] F. B. Cegla, A. J. C. Jarvis, and J. O. Davies. High Temperature Ultrasonic Crack Monitoring Using SH Waves. *Mech. Eng.*, pages 1–31, 2011.

[7] N. G. Thompson, M. Yunovich, and D. Dunmire. Cost of corrosion and corrosion mainenance strategies. *Corros. Rev.*, 25(3-4), January 2007.

[8] M. V. Biezma and J. R. San Cristóbal. Methodology to study cost of corrosion. *Corros. Eng. Sci. Technol.*, 40(4):344–352, December 2005.

[9] P. T. Wilson, D. P. Krousse, and C. J. Moss. Statistical Analysis of UT Wall Thickness Data from Corroded Plant. *Non-destructive Testing, Aust.*, 41(3), 2004.

[10] W. G. Yi, M. R. Lee, J. H. Lee, and S. H. Lee. A study on the ultrasonic thickness measurement of wall thinned pipe in nuclear power plants. In *12th Asia-Pacific Conf. NDT*, 2006.

[11] A. J. C. Jarvis and F. B. Cegla. Application of the distributed point source method to rough surface scattering and ultrasonic wall thickness measurement. *J. Acoust. Soc. Am.*, 132(3):1325–35, September 2012.

[12] K. F. Graff. *Wave motion in elastic solids*. Dover Publications, 1991.

[13] J. L. Rose. *Ultrasonic waves in solid media*, volume 107. Cambridge University Press, 2004.

[14] J. A. Hudson. *The excitation and propagation of elastic waves*. Cambridge University Press, 1980.

[15] C. F. Ying and R. Truell. Scattering of a Plane Longitudinal Wave by a Spherical Obstacle in an Isotropically Elastic Solid. *J. Appl. Phys.*, 27(9):1086, 1956.

[16] N. G. Einspruch, E. J. Witterholt, and R. Truell. Scattering of a Plane Transverse Wave by a Spherical Obstacle in an Elastic Medium. *J. Appl. Phys.*, 31(5):806, 1960.

[17] M. A. Biot. Mechanics of Deformation and Acoustic Propagation in Porous Media. *J. Appl. Phys.*, 33(4):1482, 1962.

[18] R. L. Weaver. Ultrasonics in an aluminum foam. *Ultrasonics*, 36(1-5):435–442, 1998.

[19] S. Hirsekorn and P. V. Andel. Ultrasonic methods to detect and evaluate damage in steel. *Nondestruct. Test. Eval.*, 15(6):373–393, 1998.

[20] F. B. Cegla, P. Cawley, and M. J. S. Lowe. Material property measurement using the quasi-Scholte mode - A waveguide sensor. *J. Acoust. Soc. Am.*, 117(3):1098, 2005.

[21] M. Caleap, B. W. Drinkwater, and P. D. Wilcox. Modelling wave propagation through creep damaged material. *NDT E Int.*, 44(5):456–462, September 2011.

[22] P. E. Huthwaite. *Quantitative imaging with mechanical waves*. PhD thesis, 2012.

[23] P. G. Campbell. An auxiliary scale for ultrasonic thickness measuring means, US3022661A, February 1962.

[24] F. B. Cegla. Energy concentration at the center of large aspect ratio rectangular waveguides at high frequencies. *J. Acoust. Soc. Am.*, 123(6):4218–26, June 2008.

[25] F. B. Cegla, P. Cawley, J. Allin, and J. Davies. High-temperature (500C) wall thickness monitoring using dry-coupled ultrasonic waveguide transducers. *IEEE Trans. Ultrason. Ferroelectr. Freq. Control*, 58(1):156–67, January 2011.

[26] J. Frankel and W. Scholz. Ultrasonic Studies of Stresses and Plastic Deformation in Steel During Tension and Compression. In *Rev. Prog. Quant. Nondestruct. Eval.*, pages 1577–1584, 1987.

[27] K. Lillie, C. Reed, and M. Rodgers. *Workshop on Condition Assessment Inspection Devices for Water Transmission Mains*. American Water Works Association, 2005.

[28] A. Davies, editor. *Handbook of Condition Monitoring: Techniques and Methodology*. Springer Science & Business Media, 1997.

[29] T. Rommetveit, T. F. Johansen, and R. Johnsen. Using a multi-layered transducer model to estimate the properties of paraffin wax deposited on steel. *Ultrasonics*, 51(1):85–93, 2011.

[30] M. G. Bulmer. *Principles of statistics*. Dover Publications, 1979.

[31] O. Buyukozturk, M. A. Tasdemir, O. Gunes, and Y. Akkaya, editors. *Nondestructive Testing of Materials and Structures: Proceedings of NDTMS-2011, Istanbul, Turkey, May 15-18, 2011*. Springer Science & Business Media, 2012.

[32] T. Kundu, editor. *Ultrasonic and Electromagnetic NDE for Structure and Material Characterization: Engineering and Biomedical Applications*. CRC Press, 2012.

[33] P. Rajagopal, E. Skelton, M. Lowe, R. Craster, D. O. Thompson, and D. E. Chimenti. Finite element based hybrid models for ultrasonic NDE using commercial packages. In *Rev. Prog. Quant. Nondestruct. Eval. Vols 29A 29B*, volume 1211, pages 662–669. AMER Inst. Physics, Melville, NY, USA, 2010.

[34] P. Rajagopal, E. Skelton, M. Lowe, R. Craster, J. Russell, D. O. Thompson, and D. E. Chimenti. Generic time-domain hybrid models for ultrasonic NDE. In *Rev. Prog. Quant. Nondestruct. Eval. Vols. 30A 30B*, volume 1335, pages 67–74. AMER Inst. Physics, Melville, NY, USA, 2011.

[35] W. Choi, E. Skelton, M. J. S. Lowe, R. Craster, and P. Rajagopal. Generic hybrid models for three-dimensional ultrasonic NDE. In *Rev. Prog. Quant. Nondestruct. Eval. Vols 31A 31B*, volume 1430, pages 126–133. AMER Inst. Physics, Melville, NY, USA, 2012.

[36] P. Rajagopal, E. A. Skelton, W. Choi, M. J. S. Lowe, and R. V. Craster. A generic hybrid model for bulk elastodynamics, with application to ultrasonic nondestructive evaluation. *IEEE Trans. Ultrason. Ferroelectr. Freq. Control*, 59(6):1239–52, June 2012.

[37] D. Placko and T. Kundu. *DPSM for Modeling Engineering Problems*. Wiley-Interscience, 2007.

[38] A. J. C. Jarvis and F. B. Cegla. Scattering of near normal incidence SH waves by sinusoidal and rough surfaces in 3-D: comparison to the scalar wave approximation. *Ultrason. Ferroelectr. Freq. Control*, pages 1–13, 2014.

[39] L. L. Yu. *In-situ Structural Health Monitoring with Piezoelectric Wafer Active Sensor Guided-wave Phased Arrays*. PhD thesis, 2006.

[40] A. A. Kumar. *Signals and Systems*. PHI Learning Pvt. Ltd., 2013.

[41] A. D. Poularikas, editor. *Transforms and Applications Handbook, Third Edition*. CRC Press, 2010.

[42] S. L. Hahn. *Hilbert Transforms in Signal Processing*. Artech House, 1996.

[43] A. Abbate, J. Koay, J. Frankel, S. C. Schroeder, and P. Das. Signal detection and noise suppression using a wavelet transform signal processor: application

to ultrasonic flaw detection. *IEEE Trans. Ultrason. Ferroelectr. Freq. Control*, 44(1):14–26, January 1997.

[44] F. Honarvar, F. Salehi, V. Safavi, A. Mokhtari, and A. N. Sinclair. Ultrasonic monitoring of erosion/corrosion thinning rates in industrial piping systems. *Ultrasonics*, 53(7):1251–1258, March 2013.

[45] C. D. Stoik. *Nondestructive Evaluation of Aircraft Composites Using Terahertz Time Domain Spectroscopy*. ProQuest, 2008.

[46] B. C. Wang. *Digital Signal Processing Techniques and Applications in Radar Image Processing*. John Wiley & Sons, 2008.

[47] J. Kim and B. Grisso. Electrical modeling of piezoelectric ceramics for analysis and evaluation of sensory systems. *Symp. 2008. SAS*, pages 122–127, 2008.

[48] B. K. Seung. *Development of Instantaneous Reference-free Damage Diagnosis Schemes for Plate-like Structures*. ProQuest, 2008.

[49] R. E. Challis and V. G. Ivchenko. Sub-threshold sampling in a correlation-based ultrasonic spectrometer. *Meas. Sci. Technol.*, 22(2):25902, 2011.

[50] L. D. Paarmann. *Design and Analysis of Analog Filters: A Signal Processing Perspective*. Springer Science & Business Media, 2001.

[51] S. W. Smith. *Digital signal processing: a practical guide for engineers and scientists*. 2003.

[52] R. L. Smith, W. N. Reynolds, and H. N. G. Wadley. Ultrasonic attenuation and microstructure in low-carbon steels. *Met. Sci.*, 15(11-12):554–558, November 1981.

[53] V. A. Attarian, F. B. Cegla, and P. Cawley. Long-term stability of guided wave structural health monitoring using distributed adhesively bonded piezoelectric transducers. *Struct. Heal. Monit.*, 13(3):265–280, February 2014.

[54] F. Margetan, R. Thompson, and I. Yalda-Mooshabad. Backscattered microstructural noise in ultrasonic toneburst inspections. *J. Nondestruct. Eval.*, 13(3):111–136, September 1994.

[55] A. Saxena, J. D. Landes, and J. L. Bassani. *Nonlinear Fracture Mechanics: Elastic-plastic fracture*. ASTM International, 1988.

[56] C. Scruby and B. Moss. Non-contact ultrasonic measurements on steel at elevated temperatures. *NDT E Int.*, 26(4):177–188, August 1993.

[57] M. M. Rathore and R. Kapuno. *Engineering Heat Transfer*. Jones & Bartlett Publishers, 2011.

[58] R. Rudramoorthy. *Heat and Mass Transfer*. Pearson Education India, 2010.

[59] Y. Ueda, H. Murakawa, and N. Ma. *Welding Deformation and Residual Stress Prevention*. Elsevier, 2012.

[60] J. R. Simonson. *Engineering Heat Transfer*. Palgrave Macmillan, second edition, 1988.

[61] N. Perez. *Electrochemistry and Corrosion Science*. Springer Science & Business Media, 2004.

[62] P. A. Schweitzer and P.E. *Corrosion Engineering Handbook, Second Edition - 3 Volume Set*. CRC Press, 1996.

[63] R. G. Kelly, J. R. Scully, D. W. Shoesmith, and R. G. Buchheit. Electrochemical Techniques in Corrosion Science and Engineering. *World Wide Web Internet Web Inf. Syst.*, 18:426, 2003.

[64] P. Marcus. *Corrosion Mechanisms in Theory and Practice*. CRC Press, 2002.

[65] E. E. Stansbury and R. A. Buchanan. *Fundamentals of Electrochemical Corrosion*. ASM International, 2000.

[66] P. F. Lye. *Metalwork Theory, Book 1*, volume 1. Nelson Thornes, 2014.

[67] P. Scallan. *Process Planning: The design/manufacture interface*. Butterworth-Heinemann, 2003.

[68] J. N. Friend. *The Corrosion of Iron and Steel*. Longmans, Green and Company, 1911.

[69] E. McCafferty. *Introduction to Corrosion Science*. Springer Science & Business Media, 2010.

[70] L. Yang, editor. *Techniques for Corrosion Monitoring*. Elsevier, 2008.

[71] C. G. Zoski, editor. *Handbook of Electrochemistry*. Elsevier, 2007.

[72] E. Ghali, V. S. Sastri, and M. Elboujdaini. *Corrosion Prevention and Protection: Practical Solutions*. John Wiley & Sons, 2007.

[73] Workshop Toward an Oxygen Transfer Standard. page 271, Pacific Grove, 1979. Environmental Protection Agency, Office of Research and Development, Municipal Environmental Research Laboratory.

[74] L. M. Callow, J. A. Richardson, and J. L. Dawson. Corrosion Monitoring using Polarisation Resistance Measurements: II. Sources of error. *Br. Corros. J.*, 11(3):132–139, January 1976.

[75] L. L. Scribner and S. R. Taylor. *The Measurement and Correction of Electrolyte Resistance in Electrochemical Tests, Issue 1056*. ASTM International, 1990.

[76] W. L. F. Armarego and C. L. L. Chai. *Purification of Laboratory Chemicals*. Butterworth-Heinemann, 2013.

[77] E. Machnikova, K. H. Whitmire, and N. Hackerman. Corrosion inhibition of carbon steel in hydrochloric acid by furan derivatives. *Electrochim. Acta*, 53(20):6024–6032, August 2008.

[78] I. Ahamad, R. Prasad, E. E. Ebenso, and M. A. Quraishi. Electrochemical and Quantum Chemical Study of Albendazole as Corrosion Inhibitor for Mild Steel in Hydrochloric Acid Solution. *Int. J. Electrochem. Sci*, 7:3436–3452, 2012.

[79] S. K. Shukla, A. K. Singh, L. C. Murulana, M. M. Kabanda, and E. E. Ebenso. Inhibitive effect of azorubine dye on the corrosion of mild steel in hydrochloric acid medium and synergistic iodide additive. *Int. J. Electrochem. Sci.*, 7:5057–5068, 2012.

[80] D. A. Fadare, T. G. Fadara, and Others. Corrosion Resistance of Heat-Treated NST 37-2 Steel in Hydrochloric Acid Solution. *J. Miner. Mater. Charact. Eng.*, 1(01):1, 2013.

[81] S. John, B. Joseph, K. Aravindakshan, and A. Joseph. Inhibition of mild steel corrosion in 1M hydrochloric acid by 4-(N,N-dimethylaminobenzilidine)-3-mercapto-6-methyl-1,2,4-triazin(4H)-5-one (DAMMT). *Mater. Chem. Phys.*, 122(2-3):374–379, August 2010.

[82] B. D. Craig and D. S. Anderson, editors. *Handbook of Corrosion Data*. ASM International, 1994.

[83] H. Tsubakino, A. Ando, and T. Masuda. Hydrogen attack produced by an electrochemical method using molten salts. *Trans. Iron Steel Inst. Jpn.*, (999):999–1001, 1985.

[84] J. Hucinska. Advanced vanadium modified steels for high pressure hydrogen reactors. *Adv. Mater. Sci.*, 4(2):21–27, 2003.

[85] Y. Houbaert and J. Dilewijns. Identification and quantification of hydrogen attack. *Int. J. Press. Vessel. Pip.*, 46(1):113–124, 1991.

[86] G. R. Prescott and B. Shannon. Process equipment problems caused by interaction with hydrogen - an overview. *Process Saf. Prog.*, 20(1):63–72, March 2001.

[87] A. Birring, M. Riethmuller, and K. Kawano. Ultrasonic techniques for detection of high temperature hydrogen attack. *Mater. Eval.*, 63(2):110–114, 2005.

[88] W. G. Yi, M. R. Lee, J. H. Lee, and S. H. Lee. A study on the ultrasonic thickness measurement of wall thinned pipe in nuclear power plants. pages 4–10, 2006.

[89] D. Eliezer. High-temperature hydrogen attack of carbon steel. *J. Mater. Sci.*, 16(11):2962–2966, November 1981.

[90] A. Chatterjee and A. Mal. Elastic moduli of two-component systems. *J. Geophys. Res.*, 83(7):1785–1792, 1978.

[91] A. I. Bowler, B. W. Drinkwater, and P. D. Wilcox. An investigation into the feasibility of internal strain measurement in solids by correlation of ultrasonic images. *Proc. R. Soc. A Math. Phys. Eng. Sci.*, 467(2132):2247–2270, March 2011.

[92] P. R. Williamson. A guide to the limits of resolution imposed by scattering in ray tomography. *Geophysics*, 56(2):202, February 1991.

[93] S. Li, M. Jackowski, D. P. Dione, T. Varslot, L. H. Staib, and K. Mueller. Refraction corrected transmission ultrasound computed tomography for application in breast imaging. *Med. Phys.*, 37(5):2233–2246, 2010.

[94] A. C. Kak and M. Slaney. *Principles of Computerized Tomographic Imaging*, volume 33 of *Classics in applied Mathematics*. IEEE Press, 1988.

[95] J. Wiskin, D. T. Borup, S. A. Johnson, M. Berggren, T. Abbott, and R. Hanover. Full-Wave, Non-Linear, Inverse Scattering. volume 28 of *Acoustical Imaging*, pages 183–193. Springer Netherlands, 2007.

[96] M. Jiang and G. Wang. Development of iterative algorithms for image reconstruction. *J. Xray. Sci. Technol.*, 10(2):77–86, 2002.

[97] D. Needell. Randomized Kaczmarz solver for noisy linear systems. *BIT Numer. Math.*, 50(2):395–403, 2010.

[98] T. Strohmer and R. Vershynin. A randomized solver for linear systems with exponential convergence. *Approx. Randomization Comb. Optim. Algorithms Tech.*, (2):499–507, 2006.

[99] T. Strohmer and R. Vershynin. Comments on the Randomized Kaczmarz Method. *J. Fourier Anal. Appl.*, 15(4):437–440, 2009.

[100] A. Birring and D. Alcazar. Method and means for detection of hydrogen attack by ultrasonic wave velocity measurements, 1990.

[101] G. Moran and P. Labine. *Corrosion Monitoring in Industrial Plants Using Nondestructive Testing and Electrochemical Methods*. 1986.

[102] T. L. Bergman, A. S. Lavine, F. P. Incropera, and D. P. DeWitt. *Fundamentals of Heat and Mass Transfer*. John Wiley & Sons, 2011.

[103] G. Sundararajan and P. G. Shewmon. The hydrogen attack of HSLA steels. *Metall. Trans. A*, 11(3):509–516, March 1980.

[104] T. Kamiyama, S. Enomoto, and M. Inoue. Syntheses of mercaptobenzoic acids and mercaptopyridines using elemental sulfur in the presence of NaOH-KOH. *Chem. Pharm. Bull. (Tokyo).*, 33(12):5184–5189, March 1985.

[105] A. J. C. Jarvis. *Simulation of ultrasonic monitoring data to improve corrosion characterisation within high temperature environments*. PhD thesis, Imperial College London, 2013.

[106] J. Melville, G. G. Foster, H. Street, and G. Britain. A pictorial review of failures conventional boiler plant. *Int. J. Press. Vessel. Pip.*, (3), 1974.

[107] P. P. Alvisi and V. de Freitas Cunha Lins. Acid salt corrosion in a hydrotreatment plant of a petroleum refinery. *Eng. Fail. Anal.*, 15(8):1035–1041, December 2008.

[108] D. Benstock and F. Cegla. The influence of surface roughness on ultrasonic C-scans. *J. Acoust. Soc. Am.*, 136(6):3028–3039, 2014.

[109] F. B. Cegla. Manual UT vs PIMS. In *Int. Symp. SHM NDT*, 2013.

List of Publications

[P1] A. Gajdacsi, A. J. C. Jarvis, F. Cegla, "Reconstruction of Temperature Distribution in a Steel Block Using an Ultrasonic Sensor Array", in *Review of Progress in Quantitative Nondestructive Evaluation*, Vol. 1511, pp.1166–1173, 2013.

[P2] F. Cegla, A. J. C. Jarvis, A. Gajdacsi, "Continuous Thickness Monitoring - Experience from the Field and Lessons Learned", in *Structural Health Monitoring*, Stanford, California, Vol. 1-2. pp.2194–2201, 2013

[P3] A. Gajdacsi, F. Cegla, "High Accuracy Wall Thickness Loss Monitoring", in *Review of Progress in Quantitative Nondestructive Evaluation*, Baltimore, Maryland, Vol. 1581, pp 1687-1694, 2014.

[P4] A. Gajdacsi, A. J. C. Jarvis, P. Huthwaite, F. Cegla, "Reconstruction of Temperature Distribution in a Steel Block Using an Ultrasonic Sensor Array", in *Journal of Nondestructive Evaluation*, Vol. 33, Issue 3, pp.458-470, 2014.

[P5] A. Gajdacsi, F. Cegla, "Ultrasonic wall loss monitoring of rough surfaces", in *Review of Progress in Quantitative Nondestructive Evaluation*, Boise, Idaho, 2015. In press.

[P6] A. Gajdacsi, F. Cegla, "Nanometre Precision Ultrasonic Corrosion Monitoring", in *NACE Corrosion 2015*, Dallas, Texas, 2015. In press.

[P7] A. Gajdacsi, F. Cegla, "The effect of corrosion induced surface morphology changes on ultrasonically monitored corrosion rates", in preparation for submission to *Proceedings of the Royal Society A*